CZECH TECHNICAL UNIVERSITY IN PRAGUE

Faculty of Nuclear Sciences and Physical Engineering

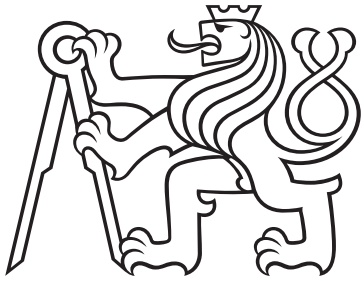

DISSERTATION

Properties of ultrashort pulse laser amplifiers

Prague 2022 Ing. Zbyněk Hubka

Declaration

I hereby declare that except where specific reference is made to the work of others, the contents of this dissertation are original and have not been submitted in whole or in part for consideration for any other degree or qualification in this, or any other university. This dissertation is my own work and contains nothing that is the outcome of work done in collaboration with others, except as specified in the text and Acknowledgements.

Zbyněk Hubka

February 2022

It is a commonplace observation that work expands so as to fill the time available for its completion.
Cyril Northcote Parkinson, The Economist, 1955

The dissertation thesis must be submitted within 7 years after the enrolment in studies at the latest.
Study and Examination Rules for Students at CTU, Part IV, Article 19

Bibliographic Entry

Author:	**Ing. Zbyněk Hubka** Czech Technical University in Prague Faculty of Nuclear Sciences and Physical Engineering Department of Physical Electronics
Title of Dissertation:	Properties of ultrashort pulse laser amplifiers
Degree Program:	Applications of Natural Sciences
Field of Study:	Physical Engineering
Supervisor:	Prof. Ing. Helena Jelínková, DrSc. Department of Physical Electronics, CTU FNSPE
Supervisor Specialist:	Ing. Pavel Bakule, DPhil. Institute of Physics, Czech Academy of Sciences ELI Beamlines
Academic Year:	2021 / 2022
Number of Pages:	96
Keywords:	Thin-disk laser, Regenerative amplifier, Pump laser, Second Harmonic Generation, OPCPA

Bibliografický záznam

Autor:	**Ing. Zbyněk Hubka** České vysoké učení technické v Praze Fakulta jaderná a fyzikálně inženýrská Katedra fyzikální elektroniky
Název práce:	Vlastnosti laserových zesilovačů ultrakrátkých pulzů
Studijní program:	Aplikace přírodních věd
Studijní obor:	Fyzikální inženýrství
Školitel:	Prof. Ing. Helena Jelínková, DrSc. Katedra fyzikální elektroniky, ČVUT v Praze, FJFI
Školitel specialista:	Ing. Pavel Bakule, DPhil. Fyzikální Ústav Akademie věd ČR ELI Beamlines
Akademický rok:	2021 / 2022
Počet stran:	96
Klíčová slova:	Tenko-diskový laser, Regenerativní zesilovač, Čerpací laser, Generace druhé harmonické, OPCPA

Acknowledgements

Working with the pump lasers described in this thesis turned out to be quite time-consuming. Sometimes it felt like building a house of cards on top of a trampoline while kids were jumping around. This metaphor manifested itself in the laser lab in several different ways. Sometimes the output energy of the seed oscillator was changing during long term SHG stability measurements and the SHG efficiency was affected. Other times, the control system software or hardware crashed in the middle of the day, requiring long debugging. And sometimes there was just not enough time to probe and tweak all the parameters before the pump laser had to be prepared for a week or two of experiments with external users. On top of all this, having a large portion of the system in vacuum made adjustments and testing more complicated than with similar pump lasers build in air.

I was able to reach all the necessary results thanks to the help of all my colleagues in Department of Laser systems and many other people present in the project before me. My gratitude goes to Control system team, as none of the hundreds of L1 laser system's motors, cameras, and software user interfaces controlling them would not be working if not for their hard work. Hats off especially to my laser team colleagues, for making our workplace such an interesting, enjoyable and fun place. And for their support, ideas, comments and system improvements we were able to realize during the whole duration of my PhD. Thank you Emily, Lukáš, František, Alex, Annika, Václav, Boguslaw, Murat, Michael, Jack, Petr, Karel, Martin, Wojciech, Gavin, Petr, Irena, Honza, Daniel, and Sam. Special thanks goes to my closest pump lasers colleagues – Robert Boge, Tyler Green, and Jakub Novák. Robert was the one who experimented with compression and frequency conversion of pulses from DIRA 1 before I joined him. On top of that, frequent discussions and fun moments with all of these 3 guys were the highlights of every week spent working in the lab.

I would like to emphasize how extremely thankful I am for the help from my dear colleague, mentor and friend Roman Antipenkov, with whom I shared an office. His intellect, knowledge, and skills will never cease to impress me. He was always willing to discuss any problem we faced, both in lab with technical devices, as well as in the office with organizational challenges, and he always played the best devil's advocate in all situations.

I would like to thank both of my supervisors – prof. Helena Jelínková for her patience and trust in me and for letting me realize my PhD work at ELI Beamlines premises; and Pavel Bakule, the L1 teamleader, for his organizational skills and friendly attitude during the whole course of my studies and work.

Large part of my thankfulness goes to my dear friends Michal Rychlík, Josef Cupal, Jitka Černohorská, Mikuláš Toman, Apolena Šustková, Martina Žáková-Greplová, Robert Krajcar and volleyball colleagues Roman Lavička, and Jan Kaufman. For all the entertaining and delightful time we got to spend together, for their interesting questions and fruitful discussions inspiring me further in my work or for improving my work-life balance even in times when I did not know I needed it. Thank you.

Finally, I would like to thank my closest family, Petra, Zbyněk, Radek, Markéta, and Stella, who always supported me, especially in my last year of PhD.

I would also like to acknowledge the following funding and grants:

Funding agency	Grant number
Ministry of Education, Youth and Sports	LM2018141
FNSPE CTU in Prague	RVO 68407700
FNSPE CTU in Prague	SGS 19/191/OHK4/3T/14
European Regional Development Fund	ADONIS, CZ.02.1.01/0.0/0.0/16–019/0000789

Abstract

This thesis describes the development of pump lasers for the last three optical parametric chirped pulse amplification (OPCPA) stages of the L1 Allegra system at ELI Beamlines. These broadband OPCPA stages amplify signal pulses centered around 830 nm at 1 kHz and the final system drives different X-ray sources used for probing ultra-fast dynamics of processes in various types of samples. The three OPCPA stages require pump pulses with energy above 100 mJ with a picosecond pulse duration and a central wavelength around 510 – 540 nm. Such lasers were not available commercially at the beginning of this work and had to be developed. The pump lasers described in this thesis are based on chirped pulse amplification (CPA) technology and Yb-doped thin-disk regenerative amplifiers (RA). Output pump pulses at 1030 nm are compressed by multilayer dielectric (MLD) grating compressors and frequency converted to 515 nm in LBO crystals. Compression and second harmonic generation (SHG) is realized in vacuum to avoid self-focusing of high intensity pulses in air.

The thesis briefly describes the differences between the OPCPA technology based on nonlinear crystals and CPA based on Ti:sapphire crystals, as Ti:sapphire oscillator is used for both the generation of broadband signal pulses as well as to generate RA seed pulses at 1030 nm. It also gives an overview of the available Yb-based technology capable of generating picosecond pulses at 515 nm. In order to provide a broader context for second harmonic generation (SHG), some sections cover nonlinear optics theory, such as phase-matching and self-focusing. These parts are followed by a short introduction to dispersion management, laser pulse temporal characterization, and effects related to gain narrowing and the variation of the RA central wavelength. The topic of vacuum cleanliness and laser induced contamination is also covered.

The main part of the thesis covers the commissioning of 3 commercial RAs, their vacuum compressors and SHG stages. With a RA delivering pulses with an energy of 230 mJ at a repetition rate of 1 kHz, the expected energy of pump pulses at 515 nm was 120 mJ, assuming a SHG efficiency of 60%. Initial results showed an SHG energy of only 85 mJ, corresponding to an efficiency of just 43% with poor long-term energy stability. The main focus of this thesis is the effort to improve this. This includes using longer LBO crystals, smaller beam diameters, and improving the initially non-Gaussian beam profiles of two linear cavity RAs by replacing the Faraday rotators. The required frequent phase-matching corrections of LBO crystals due to the rising temperature of the SHG mounts was successfully solved with temperature stabilization of those mounts by thermo-electric cooling elements. Laser induced contamination was found to be an issue on optical surfaces with incident compressed pulses, degrading the beam profile on mirrors and increasing parasitic absorption in gratings and LBO crystals. This problem is mitigated by regular radio-frequency generated plasma cleaning. These improvements enabled the generation of stable pump pulses with energies of nearly 110 mJ and SHG efficiency of 55%. One of the major issues preventing the pump lasers from reaching higher SHG efficiency is the amount of amplified spontaneous emission (ASE) present in the 1030 nm pulses. An experiment with different seed distribution and Yb:fiber oscillator proved that SHG efficiency as high as 63% can be reached when seed pulses with less ASE are used. The result of this experiment is the planned redesigned seed distribution system. This plan also addresses the problem with compression optimization of pump pulses by including a separate chirped fiber Bragg grating tunable stretcher for each of the pump lasers. These stretchers enable custom compression optimization, exploiting the best dispersion settings for each pump laser separately.

Despite the issues with sub-optimal contrast and low SHG efficiency, the 3 pump lasers developed here can regularly generate 75 – 100 mJ at 515 nm with a pulse duration between 2 – 3 ps. With pump lasers operating reliably on a daily basis, providing pump pulses for the last 3 OPCPA stages, L1 Allegra was able to provide 634 h of high energy (> 14 mJ) operation for experiments in 2019 – 2021.

Abstrakt

Tato práce popisuje vývoj čerpacích laserů pro poslední tři zesilovače založené na optickém parametrickém zesílení čerpovaných impulsů (OPCPA) systému L1 Allegra v ELI Beamlines. Tyto zesilovače umožňují zesílit impulsy s centrální vlnovou délkou 830 nm a opakovací frekvencí 1 kHz a celý systém L1 Allegra pak umožňuje provoz několika různých zdrojů rentgenového záření pro účely zkoumání dynamiky ultra rychlých procesů v mnoha odlišných chemických či biologických vzorcích. Všechny tři zesilovače potřebují čerpací impulsy s energií větší než 100 mJ s délkou impulsu několika pikosekund a centrální vlnovou délkou v rozmezí 510 – 540 nm. Takové lasery nebyly na počátku práce komerčně dostupné. Čerpací lasery popsané v této práci jsou založeny na technologii zesilování čerpovaných impulsů (CPA) a Ytterbiem dopovaných tenko-diskových regenerativních zesilovačích (RA). Jejich výstupní impulsy s vlnovou délkou 1030 nm jsou zkracovány pomocí kompresoru s dielektrickými mřížkami a jejich vlnová délka je přeměněna pomocí generace druhé harmonické (SHG) na 515 nm v LBO krystalech. Zkracování impulsů a SHG se děje ve vakuu, aby se zamezilo samo-fokusaci impulsů s vysokou intenzitou.

Práce nejdříve stručně popisuje rozdíly mezi OPCPA technologií, která využívá nelineární krystaly, a CPA technologí založenou na titan-safírových krystalech. Poskytuje také přehled dostupných technologií využívajících iontu ytterbia, pomocí kterých lze generovat impulsy s délkou několika ps na vlnové délce 515 nm. Některé části práce jsou kvůli poskytnutí souvislostí ke generaci druhé harmonické věnovány teorii nelineární optiky, zejména podmínce fázového synchronismu a samo-fokusaci. Na tyto části navazuje stručný úvod do teorie disperze, časové charakterizace laserového impulsu a do efektů souvisejících se zúžením zesilovaného spektra a posunu výstupní vlnové délky RA. Práce také popisuje téma čistoty ve vakuu a laserem způsobeného znečištění (LIC).

Hlavní část práce pojednává o zprovoznění 3 komerčních RA a kompresorů a SHG stupňů ve vakuu. Vzhledem k výstupní energii 230 mJ z RA a předpokládané SHG účinnosti 60% byla očekávaná energie na vlnové délce 515 nm 120 mJ. Počáteční měření ukázaly výstupní energii pouhých 85 mJ, odpovídající účinosti jen 43%, se špatnou dlouhodobou stabilitou. Jedním z hlavních cílů práce bylo tuto účinnost a stabilitu vylepšit. To zahrnovalo použití LBO krystalů s větší tloušťkou, menších průměrů výstupního svazku a zlepšení ne-Gaussovského profilu svazku na výstupu dvou RA s lineárním rezonátorem pomocí nahrazení Faradayových rotátorů. LBO krystaly vyžadovaly kvůli své rostoucí teplotě pravidelnou optimalizaci podmínky fázového synchronismu, což bylo vyřešeno teplotní stabilizací držáku krystalu pomocí termo-elektrických chladicích článků. Laserem způsobené znečištění představovalo problém pro optické povrchy na které dopadají impulsy s vysokou intenzitou a způsobovalo deformaci výstupního svazku z kompresoru a zvýšení absorpce laserového záření v mřížkách a LBO krystalech. Tento problém byl vyřešen pravidelným čištěním pomocí plazmatu buzeného radiovou frekvencí. Tato zlepšení umožnila generaci impulsů na vlnové délce 515 nm se stabilní energií 110 mJ a účinností 55%. Jedním z hlavních důvodů bránících čerpacím laserům v dosažení ještě vyšší účinnosti byla úroveň spontánně zesílené emise záření (ASE) přítomná v impulsech s vlnovou délkou 1030 nm. Experiment s jiným systémem zárodečných impulsů a Yb:vláknovým oscilátorem prokázal, že s menším množstvím ASE je možné dosáhnout SHG účinnosti až 63%. Výsledkem tohoto experimentu je nový návrh systému pro poskytování zárodečných impulsů. Tento návrh reflektuje také problém s optimalizací disperze každého z čerpacích laserů tím, že používá pro každý z laserů jeho vlastní laditelný vláknový prodlužovač pulzů. Tyto vláknové prodlužovače umožňují optimalizovat disperzi zárodečných impulsů pro každý čerpací laser zvlášť a tím umožní dosáhnout ideálního zkrácení impulsů v kompresoru.

I přes problémy s nedokonalým kontrastem a nízkou účinností generace druhé harmonické jsou popsané tři čerpací lasery schopny generovat impulsy s energií mezi 75 – 100 mJ na vlnové délce 515 nm s délkou impulsu 2 – 3 ps. Díky jejich spolehlivému provozu na denní bázi poskytují čerpací

impulsy posledním třem OPCPA zesilovačům laserového systému L1 Allegra. Ten byl díky tomu v letech 2019 – 2021 schopen pro experimenty poskytnout 634 h provozu s vysokou výstupní energií (> 14 mJ).

Table of Contents

List of Tables

List of Figures

List of Symbols and acronyms

Symbols

α	Thermal expansion coefficient	[K^{-1}]
$A(z)$	Amplitude of the electromagnetic wave	[$V\,m^{-1}$]
A_S	Surface area	[m^2]
β	Grating's angle of incidence	[deg]
b	Grating's groove density	[-]
c	Speed of light in vacuum	[$m\,s^{-1}$]
c_p	Specific heat capacity	[$kJ\,kg^{-1}\,K^{-1}$]
$\chi^{(n)}$	Optical susceptibility	[$(m\,V^{-1})^n$]
d	Perpendicular gratings separation distance	[m]
d_{eff}	Effective nonlinear coefficient	[$rad\,W^{-1}\,m^{-1}$]
D_m	Spectral phase coefficients in wavelength domain	[$ps^m\,nm^{-1}$]
E	Laser pulse energy	[J]
$\tilde{E}$	Electric field strength	[$V\,m^{-1}$]
E_G	Laser pulse energy distributed within the main Gaussian peak	[%]
E_i	Energy levels	[cm^{-1}]
ε_0	Vacuum permitivity	[$F\,m^{-1}$]
ε	Emissivity of a material	[-]
η	Efficiency	[%]
G	Total amplifier gain	[-]
$I(x,t)$	Laser beam intensity	[$W\,m^{-2}$]
k	Wavevector	[m^{-1}]
κ	Thermal conductivity	[$W\,m^{-1}\,K^{-1}$]
Δk	Wavevector mismatch	[m^{-1}]
$\tilde{k}$	Propagation vector	[m^{-1}]
L	Length of a material	[m]
λ	Wavelength	[m]
λ_c	Central wavelength	[m]
$\Delta\lambda$	Spectral bandwidth	[m]
M^2	Beam quality factor	[-]
n_0	Linear refractive index	[-]
n_2	Nonlinear refractive index	[$m^2\,W^{-1}$]
Δn	Refractive index change	[-]
$\mathrm{d}n/\mathrm{d}T$	Thermo-optic coefficient	[-]
$\Delta\nu$	Spectral bandwidth	[Hz]
ω	Frequency of the electromagnetic wave	[Hz]
$\delta\omega$	Instantaneous frequency	[Hz]
P	Power	[W]
P_{cr}	Threshold critical power for self-focusing	[W]
ϕ	Angle between propagation vector and the crystal's X axis	[deg]
$\phi(x,t)$	Phase	[-]
$\phi_{NL}(x,t)$	Nonlinear phase	[-]
$\varphi(\omega)$	Spectral phase	[-]

φ_m	Spectral phase coefficients in frequency domain	[s^m]
π	3.141592	[-]
$\tilde{P}$	Polarization	[C m^2]
R	Reflectivity	[%]
ρ	Density	[g m^{-3}]
$S(\omega)$	Spectral intensity	[W Hz^{-1}]
σ_B	Stefan-Boltzmann constant	[W m^{-2} K^4]
σ	Standard deviation	[a.u.]
T	Temperature	[$^\circ$ C]
τ	Laser pulse duration	[s]
ϑ	Walk-off angle	[deg]
θ	Angle between propagation vector and an optical axis	[deg]
v_g	Group velocity	[m s^{-1}]
v_p	Phase velocity	[m s^{-1}]
w_0	Laser beam waist radius	[m]
z_{sf}	Characteristic collapsed focal distance	[m]

Acronyms and abbreviations

AC	Autocorrelation, Autocorrelator
AMU	Atomic mass unit
AOM	Acousto-optic modulator
AOPDF	Acousto-optic programmable filter
AR	Anti-reflection
ASE	Amplified spontaneous emission
BBO	Beta-barium borate (β–BaB_2O_4)
BELLA	Berkeley lab laser accelerator
BiBO	Bismut borate (BiB_3O_6)
CFBG	Chirped fiber Bragg grating
CIRC	Circulator
CLBO	Cesium lithium borate crystal ($CsLiB_6O_{10}$)
CMC	Chirped mirror compressor
CMP	Compressor
CPA	Chirped pulse amplification
CW	Continuous-wave
DCPA	Double chirped pulse amplification
DFG	Difference frequency generation
DIRA	Thin-disk regenerative amplifier
DPSSL	Diode-pumped solid state lasers
ELI	Extreme Light Infrastructure
ELI ALPS	ELI Attosecond Light Pulse Source
ELI NP	ELI Nuclear Physics
FA	Fiber amplifier
FROG	Frequency resolved optical gating
FTIR	Fourier transform infrared spectroscopy
FWHM	Full width at half maximum
GD	Group delay

GDD	Group delay dispersion
ISO	Isolator
KDP	Potassium dihydrogen phosphate (KH_2PO_4)
KTA	Potassium titanyle arsenate ($KTiOAsO_4$)
KTF	Pottasium Terbium Fluoride (KTb_3F_{10})
KTP	Potassium titanyl phosphate ($KTiOPO_4$)
$\lambda/2$	Half-wave
$\lambda/4$	Quarter-wave
LBO	Lithium triborate (LiB_3O_5)
LIC	Laser induced contamination
LIDT	Laser induced damage threshold
LIGO	Laser interferometer gravitational-wave observatory
MgO:PPLN	Magnesium oxide-doped periodically poled lithium niobate ($MgO:LiNbO_3$)
MLD	Multilayer dielectric
MZM	Mach-Zehnder modulator
Nd:glass	Neodymium doped phosphate glass
Nd:YAG	Neodymium doped yttrium aluminium garnet ($Nd^{3+}:Y_3Al_2O_3$)
NIR	Near-infrared
OPA	Optical parametric amplification
OPCPA	Optical parametric chirped pulse amplification
PC	Pockels cell
PD	Photodiode
PID	Proportional, integral, and derivative control loop
PZT	Piezo-actuated fiber delay
RA	Regenerative amplifier
RF	Radio-frequency
RGA	Residual gas analysis (analyzer)
RMS	Root mean square
SHG	Second harmonic generation
SNLO	Selected non-linear optics software
TBP	Time bandwidth product
TC	Tap coupler
TEC	Thermo-electric cooler
TFP	Thin-film polarizer
TGG	Terbium gallium garnet ($Tb_3Ga_5O_{12}$)
Ti:sapphire	Titanium doped sapphire ($Ti^{3+}:Al_2O_3$)
TOD	Third order dispersion
XPW	Cross-polarized wave generation
XUV	Extreme ultraviolet
Yb	Ytterbium
Yb:fiber	Ytterbium doped fiber
Yb:KGW	Ytterbium doped potassium gadolinium tungstate ($Yb^{3+}:KGd(WO_4)_2$)
Yb:LuAG	Ytterbium doped lutecium aluminium garnet ($Y^{3+}:Lu_3Al_2O_3$)
Yb:YAG	Ytterbium doped yttrium aluminium garnet ($Y^{3+}:Y_3Al_2O_3$)
YCOB	Yttrium calcium oxoborate ($YCa_4O(BO_3)_3$)

1. Introduction

Ever since the first laser shot in 1960 [1], lasers are at the core of most modern technologies nowadays. Few people could imagine our life today without fast communications, data storage and retrieval devices, laser welding and cutting, medical treatments or bar code readers. On top of that, the laser is a key tool for scientific research, pushing the boundaries of the scientific knowledge due to advancements in laser-matter interaction sciences, including experiments in biology and chemistry.

Initially, the driving topic of laser development from the 60s through 80s was to achieve conditions for nuclear fusion with the help of generating nanosecond pulses. The chirped pulse amplification method (CPA) for optical frequencies developed by Mourou and Strickland in 1985 [2] (for which they received a Nobel price in 2018) enabled the development of lasers capable of generating ultra-short pulses with high energy. In CPA, the ultra-short pulses to be amplified are first stretched in time by more than a thousand times in order to decrease their peak power. Then amplified in either a laser active medium or nonlinear crystal and finally compressed again to short duration via a pulse compressor. The output peak power of such lasers enabled new types of experiments. The result was the increase in the number of PW-class (>0.1 PW) lasers in operation across the world from 1 in 1998 [3] to 58 (with 205 more in construction) in 2019 [4]. With them, the number of research facilities housing these and other high peak and high average power lasers grew as well. While high peak power enables experiments to cross a threshold of observing particular effects, high average power enables faster data acquisition and good statistics. These state-of-the-art laser facilities expand the potential applications of lasers to particle acceleration, radiation therapy and generation of secondary sources of short pulse radiation (electrons, protons, X-rays). That enables scientific progress in molecular and solid-state physics, real-time monitoring of chemical reactions, molecule charge transfer, or transport of electrons in solid materials.

One of the projects aimed at pushing the progress of fundamental research by using high average power and high peak power lasers is the Extreme Light Infrastructure (ELI). ELI was established due to coordination between the laser scientific community in Europe and support from the European commission. It comprises of three different facilities in Czech Republic (ELI Beamlines, aimed at creation of high-energy beams), Hungary (ELI ALPS, providing pulses with duration in the order of attoseconds) and Romania (ELI NP, with laser pulses having ultra-high intensity for research in nuclear physics). ELI Beamlines laser systems are aiming at providing pulses with high repetition rate (1kHz) at up 100 W, PW laser pulses at repetition rate up to 10 Hz and 10 PW pulses at 1 shot per minute.

This section provides a context for this work. After introduction to large laser systems based on CPA technologies (1.1), it shows an overview of diode pumped solid-state pump lasers for the systems based on Optical parametric chirped pulse amplification (OPCPA) (1.2). It also presents the ELI Beamlines project (1.3) and the laser system relevant for this thesis – the L1 Allegra system – with pump lasers based on Yb-doped thin-disk regenerative amplifiers (RA), multilayer dielectric (MLD) grating compressors and LBO crystals used for second harmonic generation (SHG).

1.1 Active media of laser amplifiers

To amplify the stretched signal pulses to high energies, and enable later recompression to pulse duration on a femtosecond timescale we need amplifiers based on active medium supporting large spectral bandwidth. Generally, high peak power lasers are trying to achieve large signal bandwidth, good signal-to-noise ratio and good conversion efficiency. The most commonly used amplification tech-

nologies capable of providing these properties in visible and near-infrared (NIR) wavelength region are Ti:sapphire crystals and OPCPA in nonlinear crystals. The laser systems being developed at ELI Beamlines facility are using both technologies and their overview is given in Fig. 1.

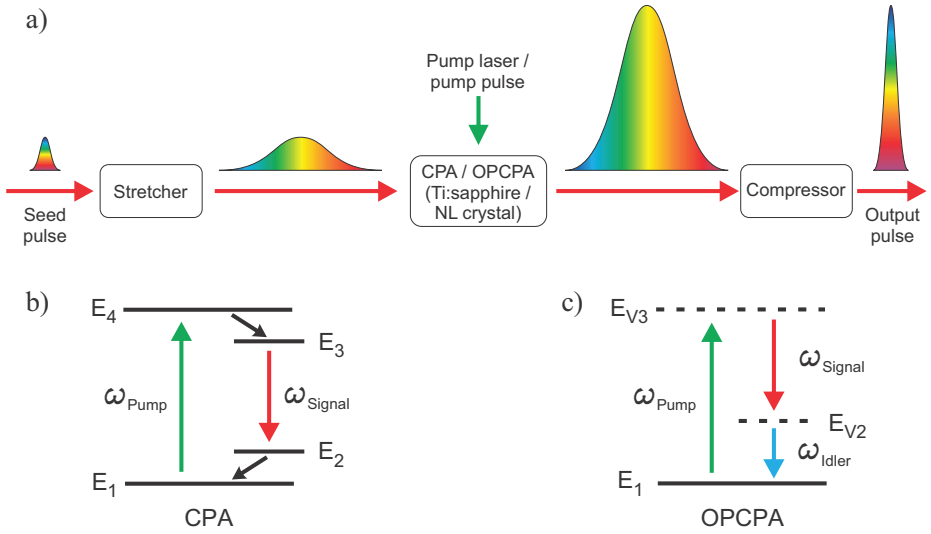

Fig. 1. Basic concept (a) and energy diagrams (b,c) behind two amplification methods – CPA and OPCPA. During CPA in active medium (b), the energy difference between the absorbed pump photon with frequency ω_{Pump} and the emitted laser photon ω_{Signal} is dissipated as heat inside the active medium. During OPCPA in nonlinear crystal, the energy difference between the absorbed pump photon ω_{Pump} and the emitted signal photon ω_{Signal} is emitted as idler photon ω_{Idler}. E_{i} – real energy levels (CPA), E_{Vi} – virtual energy levels (OPCPA).

Ti:sapphire amplification

Ever since the first ultra-broadband Ti:sapphire oscillator was reported in [5], it was clear that the Ti:sapphire crystal with its broad amplification bandwidth is suitable not only as the active medium for amplifiers, but also as the source of femtosecond pulses at the beginning of laser systems generating ultra-short pulses. The principles behind oscillators based on Ti:sapphire generating femtosecond pulses are described in [6]. Some of the other techniques, enabling the generation of broadband spectra and femtosecond pulses by using narrow spectral bandwidth lasers are described later in section 3.1.3.

During amplification in laser active media, the energy needed for the signal pulses to be amplified is stored inside the crystal itself. On one hand, the pump pulses carrying this energy does not have to have perfect wavefront or pulse temporal profile (when compared to the amplification in nonlinear crystals) and multiple pump lasers can be used. On the other hand, due to the quantum defect, part of the pump energy is always converted to heat (the Ti:sapphire crystal typical quantum defect is 34%). The resulting temperature gradient inside the amplification medium creates mechanical stress and refractive index changes, which limits the average power of such lasers. The energy stored in the active medium can further amplify stray reflections, creating prepulses, or can be emitted as the amplified spontaneous emission (ASE) over timescales corresponding to the fluorescence lifetime of the active medium. Both effects degrade the laser pulse contrast ratio, which limits the usefulness of the laser system [7]. The limitation of the repetition rate of a given laser system originates mostly from limited repetition rate of the pump lasers, providing the energy necessary for amplification. These are also

affected by the quantum defect and the consequent cooling needs. Recently built laser systems are using pump lasers based on well known and developed flashlamp pump technology (usually Nd:YAG based lasers with repetition rate of up to 10 Hz and pulse energies of up to 100 J [8], [9]). The repetition rate of laser systems using such pump lasers is therefore limited to 10 Hz. For example the Berkeley lab laser accelerator (BELLA) with 1.2 PW at 1 Hz [10] or currently developed High Field Petawatt laser at ELI-ALPS with 2 PW at 10 Hz [11]. Approaching 10 PW peak powers seems to limit the repetition rate to one shot per minute [12], [13]. Pumping Ti:sapphire with diode pumped solid state lasers (DPSSL) instead of using flashlamp technology have the advantage of higher efficiency and less deposited heat into amplifier media. Therefore, the laser system can be run at higher repetition rates. The most recent result with a PW class laser, using DPSSL pumped Ti:sapphire amplifiers is the L3 High Average Power Laser System (HAPLS) at ELI Beamlines with energy of 16 J, pulse duration below 30 fs and repetition rate of 3.3 Hz [14].

OPCPA

OPCPA was first proposed by Dubietis in 1992 [15] and became a well established method of generating pulses with good contrast, high peak and high average powers. Following the schematic in Fig. 1, during the process, happening inside a nonlinear crystal, the presence of a signal photon with frequency ω_S can stimulate the conversion of a pump photon ω_P to another, newly created, signal photon ω_S, while an idler photon ω_I is created, which ensures the process conserves energy and momentum. The result of the mechanism are two signal photons ω_S, effectively amplifying the input signal radiation. The principle, including the phase-matching condition necessary for the amplification process to be effective, is described in more detail in section 3.1.4.

There are several advantages of OPCPA in comparison with amplification in laser active medium. OPCPA benefits from the fact that no energy is stored within the nonlinear crystal and the energy transfer between the pump pulse and the signal pulse happens only when the two are temporally and spatially overlapped in the crystal. Efficient conversion requires high quality of the pump beam profile. No ASE or prepulse is generated[1] and the resulting contrast for such a laser system is inherently higher when compared to the one using Ti:sapphire amplifier [17]. Due to the parametric character of the process and the absence of stored energy, no heat is generated within the crystal due to quantum defect. Although the absorption of idler frequencies can still be a problem at high average powers, cooling of OPCPA crystals is generally less demanding and systems with higher repetition rate can be realized. Other advantage of OPCPA is the gain bandwidth, which can exceed that of the laser active media based amplifiers, allowing for generation of few cycle pulses [18]. The fact that high gain can be achieved in short crystal lengths minimize the accumulation of detrimental nonlinear effects. Systems based on OPCPA scheme can hence benefit from simpler geometries, and do not require multi-pass arrangements. More demands, however, are placed on pump lasers.

When considering the pulse duration of the OPCPA based system, using pulses with a pulse duration in picoseconds have the following advantages over nanosecond pulse duration. One, the intensity of both pump and signal pulses incident on the crystal allows to use crystals with thickness of only a few millimeters. Two, picosecond OPCPA has better contrast, related to the absence of parametric fluorescence photons outside of the pump pulse [19].

In OPCPA based laser systems it is convenient to use robust pump lasers with wavelength centered

[1] There is an analogy to the ASE in the parametric process though, called amplified parametric fluorescence (APF). If the pump pulse is long, compared to the duration of signal pulse, the creation of the signal and idler photon can happen spontaneously, limiting the amplification effect and degrading the OPCPA contrast. It was observed for the first time in 1967 [16].

between 510 – 540 nm to amplify broadband signal pulses with a central wavelength around 800 nm. The technology of pump lasers with such wavelength is well established. Apart from the desired wavelength, other key factors for the required pump pulses need to be considered. Namely the picosecond pulse duration and high energy for effective pumping at high intensity. Pump lasers with high repetition rates enable achieving high repetition rate of the whole laser system, and with it, faster data acquisition. Another crucial aspect for a pump laser is good temporal synchronization of pump pulses with signal pulses, as any instabilities directly affect the stability of the amplified pulses. Pump lasers should also have beam profiles with high quality, and good beam pointing stability. The former can otherwise degrade the amplified beam profiles due to high parametric gain, the latter can cause a phase-mismatch. These requirements are met by diode-pumped solid-state lasers. While frequency doubled outputs of neodymium based laser systems can also be used as pump lasers, one of the frequently used active media are those doped with Ytterbium ions [20] (such as Yb:YAG or Yb:LuAG). Pump lasers based on ytterbium doped thin-disks were chosen as main technology for the L1 Allegra system and the development of three of them is described in this thesis. The following section summarizes the current development of ytterbium based lasers.

1.2 515 nm pump lasers based on Yb:YAG

Ytterbium based lasers have become available in different forms – ranging from fiber lasers, Innoslab amplifiers, cryogenically cooled active mirrors or thin-disk RA. They can now deliver up to kW of average powers or pulses with hundreds of mJ of energy at 1030 nm. In order to generate the 515 nm wavelengths, intra-cavity or extra-cavity nonlinear crystals are used.

One architecture is based on photonic crystal fibers doped with Yb^{3+}. It is capable of delivering 1030 nm pulses with high energy, good spatial beam quality, with duration around 1 ps at high repetition rates. Generated pulses can exceed 10 kW of average power at 80 MHz with pulse duration under 300 fs [21], due to the use of CPA technologies and recent progress with coherent combination. There are two main disadvantages of systems based on coherently combined fibers. One is the limited output pulse energy (usually below 10 mJ [22]), limited by the aperture of the available fibers. The other is the required phase stabilization to maintain constructive interference.

Another type of the solid-state laser system capable of generating sub-ps pulses with high repetition rate and higher energy are Innoslab amplifiers (described in detail in [23]). a system with an output energy as high as 20 mJ and a pulse duration of 830 fs at 12.5 kHz was reported in [24].

Another viable option of generating picosecond pump pulses is to use cryogenically cooled active Yb:YAG mirrors. This technology makes use of the improved properties of Yb:YAG at low temperatures [25] and uses thin crystals with high reflectivity coating at the back, placed in a cryostat. The seed laser pulses to be amplified are reflected from the coated back side of the crystal (hence the name "active mirror"). However, the maximum achievable average power of such system is limited by the necessary transmission through two vacuum cryostat windows. With crystal thickness of 0.5 mm, 1.5 J of output energy and 500 Hz repetition rate at 1030 nm was reported in [26].

Each of the laser architectures mentioned earlier might be suitable for pumping a different laser system. For L1 Allegra running at 1 kHz, the most suitable technology is thin-disk amplifiers. They can produce high energy with excellent beam quality at high repetition rates and prove to have excellent scalability both in terms of energy as well as repetition rate. For example, 720 mJ was reported from a multipass system in [27], and 300 kHz Yb:YAG thin-disk amplifier was reported in [28]. It is the key technology that was chosen for all the pump lasers in L1 Allegra system.

Second harmonic generation

SHG process utilized in nonlinear crystals (LBO, BiBO, KTP, KTA and others) is the common way of converting the 1030 nm photons generated by Yb-based lasers to 515 nm. By placing these crystals inside laser cavities with Yb-doped fibers [29], DBR tapered laser diodes [30], Yb:YAG crystals [31] or Yb:YAG thin-disks [32], continuous-wave (CW) green lasers can be realized. The output power of these systems is usually around few Watts and they start to replace Ar-ion based lasers for spectroscopy and metrology applications.

In pulse lasers, it is more common to place the nonlinear crystals for frequency doubling outside the cavity. Frequency doubling of pulses with femtosecond duration can be realized by using LBO, BBO or YCOB crystals. Systems based on Yb:YAG Innoslab [33], Yb:KGW [34], or Yb-doped fiber amplifiers (FAs) [35] demonstrated generation of 515 nm with efficiencies around 50%. These systems have repetition rate ranging from 166 kHz to 76 MHz and energies in μJ to nJ. Most recent SHG result, reaching 80% conversion efficiency and generating 1 J at 400 nm by frequency doubling Ti:sapphire pulses with 27 fs in 2 mm of LBO, was reached at 5 Hz in [36]. The systems producing femtosecond pulses at 515 nm are usually used directly for experiments instead of for pumping OPCPA.

L1 Allegra system is using picosecond OPCPA for amplifying the broadband seed pulses. Hence, the most relevant pump lasers for this thesis are those with an output pulse duration of few picoseconds. Only a handful of these pump lasers have been published and none of them have the right combination of high energy, picosecond pulse duration, and 1 kHz repetition rate suitable for pumping the OPCPA stages in L1 Allegra system. The ones with the highest achieved parameters are listed in Table 1, together with Joule-class systems with pulse duration in nanoseconds. This table also shows the type and thickness of nonlinear crystals used in these systems for frequency doubling and the achieved conversion efficiency, to provide the necessary context for the rest of the thesis. The table shows the necessary pump lasers for L1 Allegra are still not available commercially and had to be developed.

Tab. 1. Pump lasers literature research. Top part of the table describes results reached with lasers having a pulse duration in picoseconds, bottom part with lasers having a pulse duration in nanoseconds. I list the key results in recent years reached by using mostly Yb^{3+}- doped active media and extra-cavity SHG. The average second harmonic conversion efficiency is 67%. Except three references, all the output wavelengths are 515 nm. Some of the entries summarize the results of pump lasers development described in this thesis. L – crystal thickness, T stab – temperature stabilized crystal mount, τ – pulse duration, η – SHG efficiency, P – average output power at 515 nm, E – output energy at 515 nm.

Crystal	L (mm)	T stab	τ (**ps**)	Rep. Rate	η (%)	P (W)	E (mJ)	Year	Ref.
				In-house developed pump lasers					
LBO	2.2	no	3	1 kHz	73	68	2 x 34	2021	[[a]]
LBO	2	no	3	1 kHz	65	55	2 x 27.5	2021	[[a]]
LBO	1.7 – 2.2	yes	1.4 – 3	1 kHz	48 – 69	100	100	2021	[[b]]
				Other pump lasers					
LBO	2	no	1.9	1 kHz	74	4.4	4.4	2020	[37]
BBO	2	yes	1.2	100 Hz	70	0.5	5	2020	[38]
BBO	1	no	0.5	46.4 MHz	55	364	0.078	2019	[39]
LBO	1.5	no	1	5 kHz	70	70	14	2016	[40]
LBO	15	yes	30	574 kHz	43	8	0.0139	2016	[41]
LBO	6	no	38	3 MHz	72	131	0.044	2016	[42]
LBO	5	no	< 8	300 kHz	70	820	2.7	2015	[28]
BBO	2	no	2	400 kHz	75	253	0.6	2014	[43]
LBO[*]	(-)	yes	100	1 kHz	57%	150	150	2017	[44]

Crystal	L (mm)	T stab	τ (**ns**)	Rep. Rate	η (%)	P (W)	E (J)	Year	Ref.
LBO	13	yes	10	10 Hz	66	597	59.7	2021	[45]
LBO	14	no	2	1 kHz	89	580	0.58	2020	[46]
LBO[**]	(-)	(-)	10 – 100	3.3 Hz	56	129	39	2016	[47]
LBO	15	no	10	10 Hz	82	56	5.6	2016	[48]
CLBO[**]	14	yes	10	10 Hz	71.5	125	12.5	2013	[49]

[a] In-house developed thin-disk RA based pump laser.
[b] Three separate pump lasers for L1 Allegra system described in this thesis.
[*] This laser system uses Nd:YAG technology to generate frequency doubled pulses at 532 nm.
[**] This laser system uses Nd:glass technology to generate frequency doubled pulses at 527 nm.

1.3 ELI Beamlines

ELI Beamlines is a large scale laser facility, built by Institute of Physics of the Czech Academy of Sciences and is aimed at pushing the boundaries of fundamental science by providing the users with state-of-the art technologies. It provides high peak power and high average power lasers and secondary sources of radiation for user-driven fundamental and applied research, including the acceleration of electrons and ions, plasma physics experiments (topics are related to high-energy density physics, warm dense matter and laboratory astrophysics), ultra-high intensity laser-matter interactions, bio and material applications or various X-ray generation sources.

The four laser systems at ELI-Beamlines are based on a variety of amplification technologies such as Ti:sapphire [50], Nd:glass [12], and OPCPA [51]. They differ in designed maximum pulse energies, repetition rates, pulse durations and central output wavelengths. The overview of their designed parameters is in Table 2. This thesis describes the development of pump lasers for L1 Allegra laser system.

Tab. 2. Overview of the four laser systems at ELI Beamlines and their designed parameters. E – energy, τ – pulse duration, P – power, λ_c – central wavelength.

Laser system	Output E	τ	Rep. rate	Technology	Peak P	λ_c
L1 Allegra	100 mJ	15 fs	1 kHz	OPCPA	6 TW	830 nm
L2 DUHA	2 J	25 fs	50 Hz	OPCPA	80 TW	820 nm
L3 HAPLS	30 J	30 fs	10 Hz	Ti:sapphire	1 PW	805 nm
L4 Aton	1.5 kJ	150 fs	1/60 Hz	OPCPA + Nd:glass	10 PW	1057 nm

L1 Allegra laser system

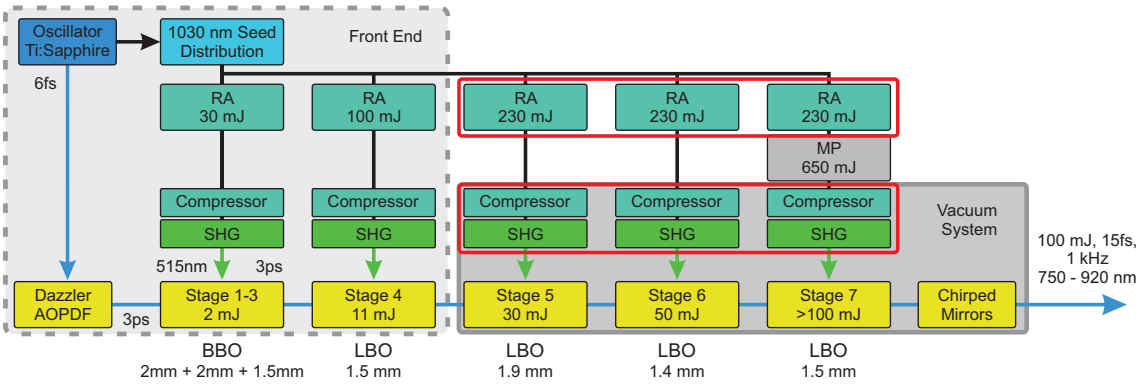

Fig. 2. Layout of the L1 Allegra system. Sections developed as part of this thesis are marked red. RA – thin-disk regenerative amplifier, MP – multipass amplifier planned upgrade, SHG – second harmonic generation stages with LBO crystals, AOPDF – acousto-optic programmable dispersive filter stretching the broadband pulses.

The L1 Allegra is an OPCPA based laser system designed to provide 100 mJ pulses at 1 kHz with a pulse duration below 15 fs and spectrum spanning 750 nm – 920 nm. The layout of the system is shown in Fig. 2. Its purpose is to drive various X-ray sources in experimental hall E1, such as a plasma X-ray source [52] and a high-harmonic extreme ultraviolet (XUV) source [53] for probing ultra-fast dynamics of processes in various types of samples. The system is based on a Ti:sapphire

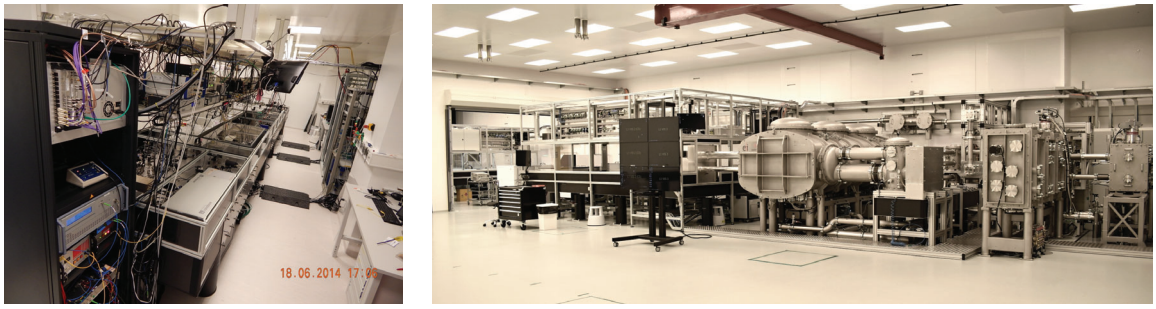

(a) (b)

Fig. 3. The progress of L1 Allegra system. (a) – small laser lab at ASCR premises at Ládví, Prague in 2014. (b) – complete system at ELI Beamlines, Dolní Břežany premises in 2018.

oscillator providing both broadband signal pulses as well as seed pulses at 1030 nm for the pump lasers. It has 7 OPCPA stages with non-linear crystals (either BBO or LBO) with combined thickness of only 12 mm and the pump pulses are provided by 5 pump lasers in total. The photos showing the progress of L1 development over the years starting from a small scale lab all the way down to the fully developed laser system are shown in Fig. 3.

The broadband signal seed pulses for the OPCPA stages are generated in the Ti:sapphire oscillator and are first stretched from 6 fs to 3 ps by applying a group delay dispersion (GDD) of roughly $+6000\,\mathrm{fs}^2$ with a Acousto–Optic Programmable Dispersion Filter (AOPDF). The AOPDF can also modify the higher order dispersion so that the final compression at the end of the L1 system can be optimized or so that experimental station in E1 hall using the L1 Allegra laser can modify the dispersion in order to reach the best conditions for the experiments. The compression of the amplified broadband pulses is realized with a set of 32 chirped mirrors, each providing about $-190\,\mathrm{fs}^2$ of GDD, ensuring high reflectivity. This method also limits the parasitic nonlinear effects when compared to compression in bulk materials. The pump pulses are provided by Yb-doped thin-disk based RA, generating pulses with 30 – 230 mJ energy at 1030 nm that are compressed by MLD grating compressors to 2 – 3 ps pulse duration and frequency doubled in LBO crystals to 515 nm. With the designed intensity of the incident 1030 nm picosecond pulses on the SHG crystal of $100\,\mathrm{GW/cm}^2$, crystals with a thickness of 1 – 3 mm should be enough to reach near maximum conversion efficiency.

The first two pump lasers within the L1 Allegra systems were developed by Jakub Novák [54]. They provide about 16 and 55 mJ at 515 nm and their compressors and SHG stages are placed in air. The last three pump lasers were developed as part of this thesis. They are based on commercial RA from Trumpf Scientific lasers, MLD grating compressors and SHG stages with LBO crystal. The compressors and SHG stages had to be placed in vacuum chamber and the final designed output energy of the pump lasers was 120 mJ at 515 nm. The details and results from the development are described in section 4.

1.4 Thesis outline

The thesis is divided into 7 sections. The first section provided an introduction to OPCPA laser systems, Yb-based pump lasers, ELI Beamlines project and listed details of the L1 Allegra system design. The second section describes the aims and objectives of this thesis. The third section provides the necessary context and theoretical background for all the technologies used and described within the thesis, covering the basic concepts for SHG or self-focusing, dispersion compensation, gain narrowing in amplification media or vacuum cleanliness.

Section four is the main body of the thesis. There, I describe the development of high energy pump lasers for the three most energetic OPCPA stages in the L1 Allegra laser system. I characterize the three commercially acquired thin-disk RA providing pulses with energy of 230 mJ at 1030 nm. I describe their commissioning and integration into the system and the development of their compressors and SHG stages, which are placed in a vacuum chamber to avoid detrimental nonlinear effects of high intensity pulses in air. I specify key problems with the seed distribution, with rising temperature of the SHG stages, with vacuum cleanliness and with beam profile imperfections. All of these issues prevent the pump lasers from generating the designed stable energy of 120 mJ with a pulse duration of 3 ps at 1 kHz. I also discuss the realized improvements.

In the last two sections, I summarize all the achieved results and I suggest some of the further enhancements of the pump lasers, which could be implemented in the near future. I also list my authored and co-authored papers, conference contributions, and finally, append my two peer-reviewed journal publications.

2. Aims and objectives of the thesis

Develop a system of 3 pump lasers for the final 3 OPCPA stages of L1 Allegra laser system.

1. Successfully commission 3 commercial regenerative amplifiers, delivering pulses with energy of 230 mJ, wavelength of 1030 nm at repetition rate of 1 kHz.
2. Commission the vacuum compressors and SHG stages for these RA.
3. Identify the problems behind low SHG efficiency, which prevent the pump lasers from reaching 120 mJ with a pulse duration of 3 ps at 515 nm. Propose their solution.
4. Solve the temperature stabilization of SHG stages in vacuum.
5. Improve the output beam profile of the RA with a linear cavity design.
6. Find a solution for mitigating laser induced contamination of optical components in vacuum chambers.

3. Methods and technology

In order to provide the necessary context for the experimental part of this thesis, several theory excerpts and concepts are introduced in the following sections. This includes parts from nonlinear optics regarding second harmonic generation and phase-matching, dispersion management, laser pulse characterization, gain narrowing or vacuum contamination.

3.1 Selected nonlinear optics phenomena

During the interaction of laser light with matter, the optical intensity can be high enough to modify the optical properties of the material, which in turn modifies the light waves. "Nonlinear optics" is the study of these exotic effects, which can change the frequency or temporal and spatial profiles of the interacting waves. The applications of nonlinear optical phenomena were often key moments in laser sciences. For example the first SHG in 1961 [55], development of all-optical switching for rapid optic fiber communications in 1983 [56], Kerr-lens modelocking of Ti:sapphire laser in 1991 [57], or optical frequency combs demonstration by use of cross-phase modulation (XPM) in 2000 [58]. The complete overview of all the nonlinear effects and their application is out of the scope of this work and can be found elsewhere [59], [60]. One of the key nonlinear effects related to this thesis is SHG, used to convert pump pulses for the amplification stages from 1030 nm to 515 nm. Another is difference frequency generation, utilized in the broadband signal amplifiers through optical parametric amplification. Also important are self-focusing and self-phase modulation, responsible for detrimental effects inside RAs and during propagation in air.

The response of a material to incident light is usually described by polarization (or dipole moment per unit volume) $\tilde{P}$, which appears as a driving part on the right side of the wave equation as follows

$$\nabla^2\tilde{E} - \frac{1}{c^2}\frac{\partial^2}{\partial t^2}\tilde{E} = \frac{1}{\varepsilon_0 c^2}\frac{\partial^2\tilde{P}}{\partial t^2}, \tag{1}$$

where $\tilde{E}$ is the electric field, c is the speed of light in vacuum and ε_0 is the vacuum permitivity. Unlike in linear optics, where the polarization $\tilde{P}(t)$ depends only linearly on the strength of the optical field $\tilde{E}(t)$, in nonlinear optics, the polarization $\tilde{P}(t)$ has terms that relies on $\tilde{E}^2(t)$, $\tilde{E}^3(t)$ and so on:

$$\begin{aligned}\tilde{P}(t) &= \varepsilon_0\chi^{(1)}\tilde{E}(t) + \varepsilon_0\chi^{(2)}\tilde{E}^2(t) + \varepsilon_0\chi^{(3)}\tilde{E}^3(t) + ... \\ &\equiv \tilde{P}^{(1)}(t) + \tilde{P}^{(2)}(t) + \tilde{P}^{(3)}(t) + ... = \tilde{P}^{(1)}(t) + \tilde{P}^{(NL)}(t).\end{aligned} \tag{2}$$

The tensor $\chi^{(1)}$ is the measure of proportionality and is called linear optical susceptibility and the $\chi^{(2)}$ and $\chi^{(3)}$ are nonlinear optical susceptibilities of the second and third order. $\tilde{P}^{\mathrm{NL}}$ consists of nonlinear polarization terms of the second and higher orders and are responsible for generation of new frequency components in an optical field or for modification of the propagating wave properties.

In relation to this thesis, $\chi^{(2)}$ is important for the special case of sum frequency generation (SHG) process and difference frequency generation process. $\chi^{(3)}$ is relevant for self-focusing of beams with high intensity.

3.1.1 Second harmonic generation

If we consider a simple monochromatic wave with single frequency component ω_1, we can write the spatial amplitude and the rapidly varying time dependence as

$$\tilde{E}(z,t) = A_1(z)e^{i(k_1 z - \omega_1 t)} + \text{c.c.}, \tag{3}$$

where $k_1 = \frac{n(\omega)\omega_1}{c}$ is called the wavevector and the variable $A(z)$ is the amplitude of the wave. If such a wave is incident on a material with second order susceptibility $\chi^{(2)}$, by substituting (3) into the second-order polarization

$$\tilde{P}^{(2)}(t) = \varepsilon_0 \chi^{(2)} \tilde{E}(t)^2 = \varepsilon_0 \chi^{(2)} A_1^2 e^{i2k_1 z} e^{-i2\omega_1 t}, \tag{4}$$

we see that during this process radiation with frequency $2\omega_1$ will be generated, due to the term $e^{-i2\omega_1 t}$. We call this second harmonic generation (SHG), or frequency doubling, and it is a key nonlinear process for converting the infrared photons of RAs at 1030 nm to green pump photons at 515 nm, which are later used to provide pump energy for the OPCPA stages of a laser system. The schematic of the interaction is shown in Fig. 4a.

3.1.2 Optical parametric amplification

If the incident light on a material with $\chi^{(2)}$ consists of two frequency components, $\omega_1 \neq \omega_2$,

$$\tilde{E}(z,t) = A_1(z) e^{i(k_1 z - \omega_1 t)} + A_2(z) e^{i(k_2 z - \omega_2 t)} + c.c., \tag{5}$$

the contribution to the driving term in the equation (1) will also contain components with frequency $\omega_3 = (\omega_1 - \omega_2)$. The process of creation of radiation with this frequency is called difference frequency generation (DFG). During this process, the energy of the "pump" photon with ω_1 is transferred to the newly created "signal" photon ω_2 and in order to satisfy the energy conservation rule, an "idler" photon with frequency $\omega_3 = (\omega_1 - \omega_2)$ has to be created as well. Although the energy levels involved in the process are virtual, it is similar to stimulated emission in laser active media in a way that the presence of the wave with frequency ω_2 stimulates the two photon emission from the higher energy level after the absorption of the photon with frequency ω_1. The incident radiation with ω_2 is hence amplified by the process. Often, this method of amplification is combined with stretching (chirping) the signal pulses in time and is referred to as optical parametric amplification (OPA)[2]. The geometry and energy diagram of the process are shown in Fig. 4b. Under certain conditions, the OPA process can be used for amplifying a wide range of incident signal frequencies with quasi-monochromatic pump pulses. The only difference would then be the larger spectrum of idler frequencies generated as the consequence of energy conservation. This way, the OPA process can be used to amplify the stretched broadband signal pulses from the Ti:sapphire oscillator centered around 800 nm by the energy from narrow spectral bandwidth pump pulses centered around 515 nm (provided by the pump lasers). The process of using OPA with stretched pulses is called OPCPA.

3.1.3 Self-focusing and Self-phase modulation

Not all materials exhibit both second as well as third order susceptibilities. Due to the material properties and symmetry rules, the susceptibility $\chi^{(2)}$ is non-zero only in noncentrosymmetric crystals (BBO, LBO, KDP and many others). Liquids, gases, glass and some crystals display inversion symmetry and only odd orders of $\chi^{(n)}$ can occur [61]. The third order susceptibility will never vanish though and has the form of

$$\tilde{P}^{(3)}(t) = \varepsilon_0 \chi^{(3)} \tilde{E}(t)^3, \tag{6}$$

[2]The process can occur also without the presence of the photon ω_2. The two photons ω_2 and ω_3 are then emitted spontaneously, the generated field is weaker, and the process is called optical parametric generation (OPG) [61].

Substituting a monochromatic wave with frequency ω_1 from (3) to (6) yields also a term with $e^{i\omega_1 t}$. This term describes a contribution to the polarization at the same frequency of the incident field, effectively modifying the refractive index. This can then be written as

$$n = n_0 + n_2 I(t), \tag{7}$$

where n_0 is the classical linear refractive index, $I = \frac{1}{2} n_0 \varepsilon_0 c E^2$ is the incident wave intensity and

$$n_2 = \frac{3}{2 n_0^2 \varepsilon_0 c} \chi^{(3)} \tag{8}$$

is a number called nonlinear refractive index, describing the strength of the effect.

Self-focusing

Intense beams with non-uniform spatial intensity distribution (typically Gaussian beams) passing through a medium with positive n_2 experience self-focusing as a result of third-order nonlinearity (often also called Kerr nonlinearity). In case of a Gaussian beam the material will act as a positive lens.The threshold critical power P_{cr} for self-focusing and the characteristic collapsed focal distance z_{sf} is [61]:

$$P_{\mathrm{cr}} = \frac{0.146\,\lambda^2}{n_0\, n_2}, \quad z_{\mathrm{sf}} = 0.765\, w_0^2 \sqrt{\frac{n_0}{n_2 P}}, \tag{9}$$

where laser parameters are the wavelength λ, waist radius w_0, and peak power P and material properties are the linear refractive index n_0 and the nonlinear refractive index n_2.

Assuming a RA with 230 mJ output energy at 1030 nm, 500 ps duration before compression, 10 mm beam diameter at $1/e^2$, $n_0 = 1.0003$ (air) and $n_2 = 31 \cdot 10^{-24}\,\mathrm{m^2/W}$ [62], the critical power for self-focusing of 5.2 GW is larger than the pulse peak power of 0.46 GW and the beam would collapse after a safe 160 m of propagation. After compression though, with the pulse duration of 3 ps, the collapsing distance is only 13 m. After frequency doubling to 515 nm, the distance will be even shorter. The reason is the dependence of beam waist radius and nonlinear refractive index on wavelength [63]:

$$w_0(\lambda) \sim \lambda,\, n_2(\lambda) \sim \frac{1}{\lambda^2}. \tag{10}$$

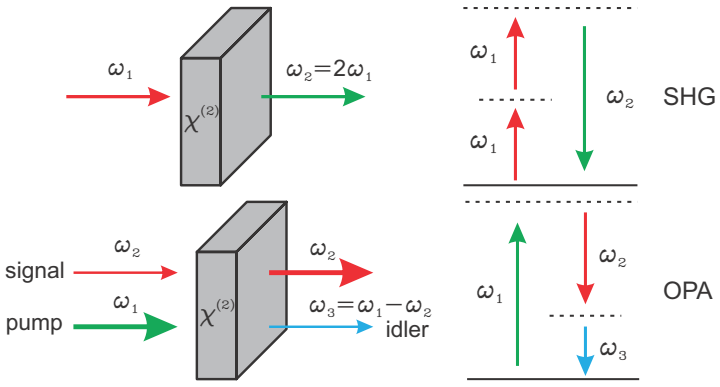

Fig. 4. Geometry and energy-level schematics of SHG and OPA processes.

Within the L1 Allegra system, self-focusing is a problem for all compressed pump pulses (having pulse duration of < 3 ps and energies well above several millijoules at both 1030 nm as well as 515 nm), for stretched picosecond broadband signal pulses after OPCPA stage 4 (3 ps and 5 – 12 mJ) and for compressed femtosecond signal pulses after the chirped mirror compressor. In order to avoid collapsing of the beams in air, last three pump laser compressors, the SHG stages, the last three OPCPA stages, the chirped mirror compressor, and all the consequent beam transport to experimental halls had to be placed in vacuum.

Self-phase modulation and B-integral

Another consequence of refractive index dependency on intensity is the self-phase modulation (SPM) effect. During the propagation of an optical pulse with frequency ω_0 (3) through media with nonlinear refractive index (7), the medium will change the phase of the transmitted pulse as follows:

$$\tilde{E}(z,t) = A(z)e^{ik_0 z}e^{-i(\omega_0 t - n_2 I(t)\omega_0 L/c)}, \tag{11}$$

where k_0 is the wave vector with linear refractive index n_0 and L is the length of the medium. The instantaneous frequency of such a wave can be written as

$$\omega(t) = \omega_0 + \delta\omega(t), \tag{12}$$

where

$$\delta\omega(t) = \frac{d}{dt}\left(n_2 I(t)\frac{\omega_0}{c}L\right) \equiv \frac{d}{dt}\phi_{\mathrm{NL}}(t) \tag{13}$$

describes its changes in time. The consequence of the time varying phase term is broadening of the spectra due to the self-phase modulation. The leading edge of the optical pulse shifts to lower frequencies, the trailing edge of the pulse shifts to higher frequencies when n_2 is positive. This effectively broadens the spectrum and introduces a positive chirp. The process is schematically shown in Fig. 5a. Depending on the strength of the spectral broadening due to self-phase modulation, the resulting spectrum, Gaussian initially for example, can get slightly broader with low $\Delta\phi_{\mathrm{NL}}$ or quite complicated with heavy modulation if the nonlinear shift is large enough (see Fig. 5b for example how the spectrum changes due to propagation in silica fiber).

In order to judge how much nonlinear phase shift will be introduced by the system, the variable B-integral is often used

$$\phi_{\mathrm{NL}}(t) = \frac{2\pi\omega}{c}n_2\int_0^L I(z,t)\,dz, \tag{14}$$

where L is the length of the material, n_2 is the nonlinear refractive index and I the intensity of a laser pulse with frequency ω. Usually, one strives to design the system so that the accumulated B-integral in all the material is less than 1 rad. This nonlinear phase can be compensated just as the linear phase can, but the phase function can be quite complicated with modulation and ripples in worst cases. The nonlinear effects can be compensated by introducing a material with opposite sign of n_2 (for example GaAs wafers, although with limited laser induced damage threshold [64]). More practical method of compensating the self-focusing and self-phase modulation might be the cascaded second-order nonlinear process in two subsequent nonlinear crystals [65], [66].

Self-phase modulation process is important for broadening of spectra inside fibers, crystals or hollow core fibers filled with gas [68]. This way, the bandwidth limit of the amplifying medium or the laser oscillator can be circumvented and few-cycle ultra-short pulses with < 5 fs can be generated after

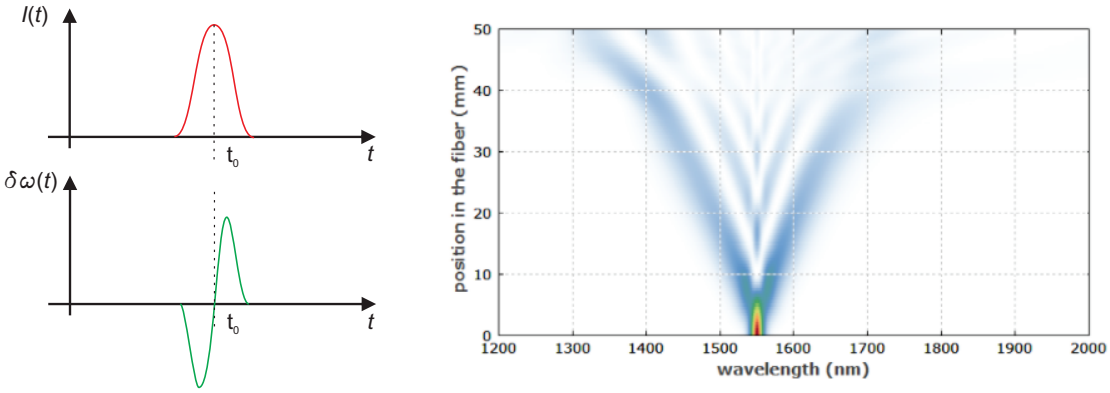

(a) (b)

Fig. 5. Self-phase modulation. (a) – Intensity of the incident pulse and change in instantaneous frequency. The leading edge of the optical pulse creates new red frequency components with respect to the central frequency, due to the negative $\delta\omega(t)$, (b) – Evolution of the spectrum after propagating the ultra-short laser pulse through optical fiber from RP Photonics Encyclopedia [67].

subsequent compression [69]. Self-focusing and self-phase modulation are important part of nonlinear processes responsible for ultra-broadband spectrum generation (called continuum, supercontinuum or whitelight) in crystals [70]. Continua can be used as seed signal pulses for parametric and laser amplifiers. For example, femtosecond pulses are commonly used to generate supercontinuum [71], [72] and picosecond pulses were used to generate supercontinuum in the NIR [73] or mid-IR wavelengths as well [74]. One of the advantages of a picosecond supercontinuum seed for the large laser systems is the need of only a single fiber oscillator at the beginning of the whole chain. This oscillator can provide seed pulses for picosecond pump lasers, those in turn generate supercontinuum as broadband signal source for the OPCPA stages. This way, no expensive Ti:sapphire oscillator or complicated synchronization of two oscillators is needed. One large laser system using a single Yb:KGW oscillator and the subsequent supercontinuum generation is the Sylos system of ELI-ALPS (with energy 53.8 mJ, $<$9 fs duration at 1 kHz, corresponding to $>$53 W average and 5.5 TW peak power [44]).

3.1.4 Phase-matching

The earlier described nonlinear processes of SHG or OPA will be efficient only under certain circumstances and only one of the processes can generally be dominant, depending on the so called phase-matching conditions. Using SHG as an example, we can derive the coupled-amplitude equation describing how energy of the second harmonic wave with amplitude A_2 is growing at the expense of energy from the wave with amplitude A_1. Assuming the amplitude $A(z)$ in (3) is only slowly varying with the distance z, we find the derived equation contains the term $e^{i\Delta kz}$:

$$\frac{\mathrm{d}A_2}{\mathrm{d}z} = \frac{i\omega_2^2 d_{\mathrm{eff}}}{k_2 c^2} A_1^2 e^{i\Delta kz}. \tag{15}$$

Here, d_{eff} is the effective nonlinear coefficient (related to the tensor $\chi^{(2)}$, dependent on incident radiation polarization and material properties) and

$$\Delta k = 2k_1 - k_2 = \frac{2\omega_1 n(\omega_1)}{c} - \frac{\omega_2 n(\omega_2)}{c} \tag{16}$$

is called a wavevector mismatch. Only when $\Delta k = 0$ can the process be efficient. It describes the momentum of interacting photons, which needs to be conserved. Energy conservation is described by the relation $\omega_2 = 2\omega_1$. If both energy and momentum are conserved, we say the process is perfectly phase-matched, as the two (in this case) interacting waves stay phase and the energy transfer from A_1 to A_2 can be most effective. Assuming a simplified case with monochromatic waves and undepleted pump (A_1 is constant), the integrated solution of the coupled-amplitude equation shows the efficiency of the second harmonic process inside a crystal with the length L is proportional to a function

$$\eta \sim \left(\frac{\sin(\Delta kL/2)}{(\Delta kL/2)}\right)^2 \equiv \mathrm{sinc}^2\left(\frac{\Delta kL}{2}\right). \tag{17}$$

When the efficiency of the process is high (for example typical 50 – 70% SHG efficiency generated by the lasers in this thesis), the undepleted pump approximation is no longer valid and the efficiency has to be calculated numerically (compare the two functions in Fig. 6a), but the equation (17) is a good example, as the SHG efficiency in depleted pump case also drops sharply for Δk values larger than zero. In order for Δk to be zero, the SHG process requires that

$$n(\omega_1) = n(2\omega_1). \tag{18}$$

In this case we conserve both energy and momentum at the same time and we can call this requirement the phase-matching condition for SHG. Typically, the refractive index will always be a monotonously rising function of frequency with $n(\omega_1) < n(2\omega_1)$ as shown in Fig. 6b. The equality (18) can only be satisfied in birefringent crystals, where the refractive index depends on the polarization of the incident radiation. By using orthogonally polarized photons, we can satisfy the equality of refractive indices if the photons of incident 1030 nm wave have ordinary polarization and the generated 515 nm have extraordinary polarization[3] $n_e(2\omega_1) = n_o(\omega_1)$.

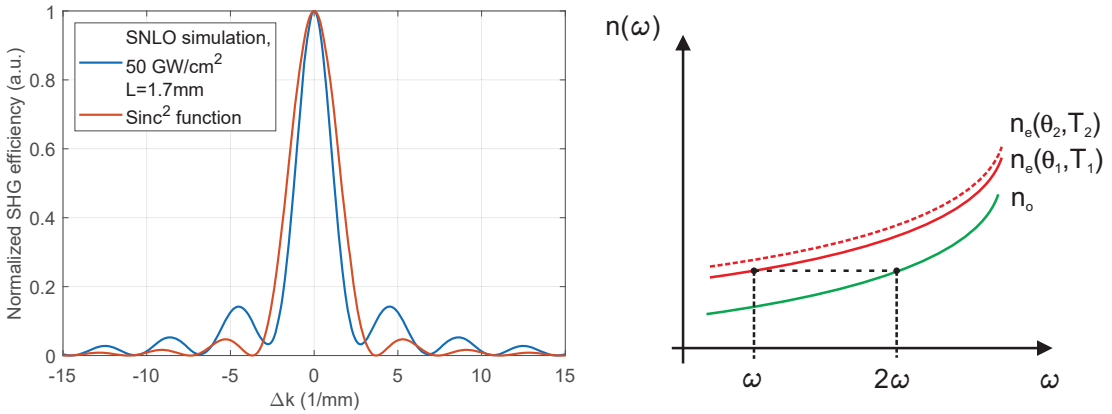

(a) (b)

Fig. 6. SHG vs Δk and phase-matching, (a) – Dependence of SHG efficiency on the wavevector mismatch for monochromatic wave (blue) as well as for the real RA output with 1 nm bandwidth at 1030 nm, 3 ps pulse (red). Crystal length is 1.7 mm. Simulated by the Selected non-linear optics software (SNLO) [75], (b) – Dispersion and matching of refractive indices for phase-matching.

[3] n_e is the refractive index for light polarized in the plane containing the propagation vector $\tilde{k}$ and the optical axis of the crystal. The n_e depends on both angle θ between the $\tilde{k}$ and the optical axis and on temperature T. n_o is the refractive index for light polarized orthogonally to the extraordinary polarization.

Angular (critical) phase-matching

This type of phase-matching is achieved by the correct orientation of the crystal relative to the incident and generated waves. In practise it is realized by cutting the crystal at the calculated angle so that the incident light can be perpendicular to the surface. The SHG process in a biaxial negative nonlinear crystal converting two ordinary polarized photons at 1030 nm to photon with extraordinary polarization at 515 nm (abbreviation used is ooe) is called SHG type I [76]. Other types (eeo, oee, eoo) can be realized in other crystals as well. Type I is used to generate photons at 515 nm in pump lasers developed as part of this thesis.

If a beam with extraordinary polarization propagates at an angle against the optical axes of a birefringent crystal, its intensity propagation will drift away from the initial direction of propagation $\tilde{k}$ (see Fig. 7). The effect is called spatial walk-off, affects the spatial overlap between the fundamental and second harmonic frequencies and with it, the energy transfer during the process. a typical walk-off angle ϑ in LBO at 515 nm is 8.31 mrad. It often causes issues when we use long crystals or beams with small radius and large divergence. In those cases, temperature phase-matching is preferred.

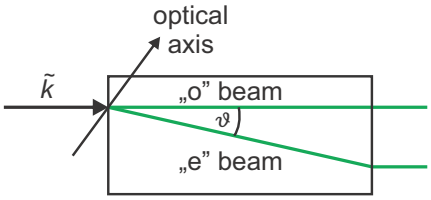

Fig. 7. Spatial walk-off. Beam with extraordinary polarization "e" drifts from the initial beam direction of propagation $\tilde{k}$. ϑ is called the walk-off angle. This effect influences the spatial overlap with the ordinarily polarized "o" beam and with it, limits the efficiency of a selected nonlinear process.

Temperature (noncritical) phase-matching

Both ordinary and extraordinary refractive indices are temperature dependent. By changing the temperature of the crystal, the Δn change can be described by the thermo-optic coefficient $\mathrm{d}n/\mathrm{d}T$ [77] as:

$$\Delta n = n_0 + \frac{dn}{dT} = n_0 + \left(\frac{\partial n}{\partial T}\right)_\rho + \left(\frac{\partial n}{\partial \rho}\right)_T \left(\frac{\partial \rho}{\partial T}\right), \tag{19}$$

where n_0 is the original refractive index at a given temperature and ρ is the density of the molecules comprising the optical material. The second term is always negative due to the negative thermal expansion $\frac{\partial \rho}{\partial T}$ and the resulting $\mathrm{d}n/\mathrm{d}T$ can be either positive or negative, depending on the material [78]. In practice, the noncritical phase-matching is achieved by fixing the value of the angle θ at 90° and varying the temperature of the crystal [61]. The nonlinear crystals are generally placed in ovens heating the crystals to temperatures around 150 °C (for type I SHG in LBO at 1064 nm). Noncritical phase-matching benefits from the absence of spatial walk-off and is less sensitive to beam misalignment. We chose angular phasematching in L1 Allegra SHG stages with LBO crystals, due to large beam diameter (10 – 15 mm) and small crystal thickness (a few mm).

Temperature influence during angular phase-matching

When the angular phase-matching is used to satisfy the condition $\Delta k = 0$, $\mathrm{d}n/\mathrm{d}T$ will affect Δk as well. The LBO crystals in the SHG stages of pump lasers described in this thesis are cut so that

the fundamental 1030 nm photons are polarized in parallel with Z axis and the extraordinary 515 nm photons with the X axis. The respective $\mathrm{d}n/\mathrm{d}T$ coefficients of LBO in those axes are [79]:

$$\begin{aligned} \frac{\mathrm{d}n_x}{\mathrm{d}T} &= (-3.76\,\lambda + 2.30)\cdot 10^{-6}, \\ \frac{\mathrm{d}n_z}{\mathrm{d}T} &= (1.5\,\lambda - 9.7)\cdot 10^{-6}, \end{aligned} \tag{20}$$

and the resulting calculated Δk and SHG efficiency change is plotted in Fig. 8. The temperature difference inside the 1.7 mm LBO crystal required for the SHG efficiency to drop by 50% is 11.55 °C.

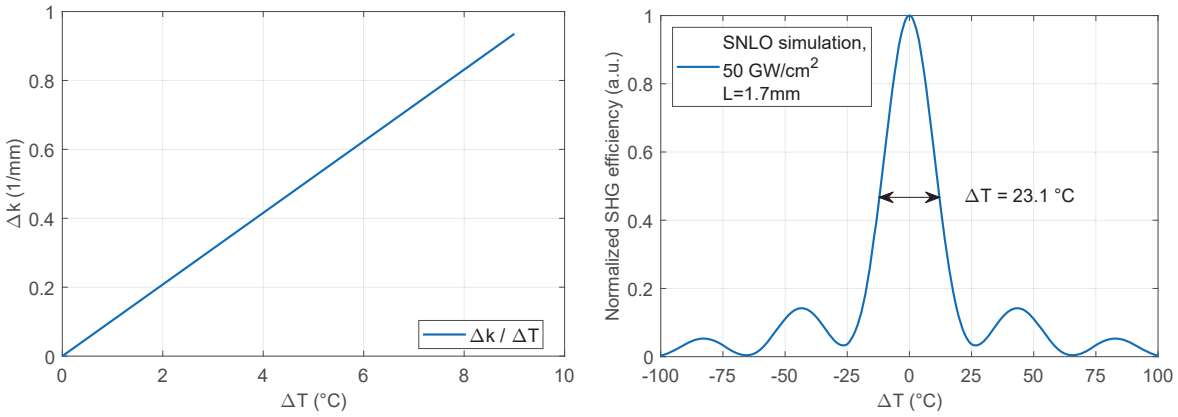

(a) (b)

Fig. 8. Temperature change of Δk caused by $\mathrm{d}n/\mathrm{d}T$ and related SHG efficiency in LBO, (a) – Δk change caused by $\mathrm{d}n/\mathrm{d}T$ as a function of temperature, calculated from (16), (b) – simulated SHG efficiency from Fig. 6a with ΔT instead of Δk on X axis.

3.2 Dispersion and CPA

Dispersion describes a dependence of some property (for example of the refractive index or of the laser pulse phase velocity) on frequency. During laser pulse propagation in optical media the phase and group velocity values are different, in contrast to propagation in vacuum. Dispersion of both phase and group velocities will cause a short pulse (with broad spectrum) to become longer in time after propagation. Dispersion management is important for modelocked oscillators, generation of femtosecond pulses and for all lasers using the CPA scheme in general. For this thesis, the key elements for controlling dispersion are chirped fiber Bragg gratings (CFBG) written in optical fibers for stretching the laser pulses before amplification in a RA and Treacy-type free space MLD grating compressors for shortening the pulses after amplification. These devices are related to geometrical dispersion and the fact that different wavelengths travel different path. Propagation in air, optical windows and crystals on the other hand are related to the dispersion of refractive index. More detailed information about the types of dispersion and devices capable of modifying it can be found in a nice review article here [80].

In order to easily model the laser pulse dispersion induced by propagation through a medium, a description of the pulse in the spectral domain is frequently used. By applying a Fourier transformation to the complex amplitude of the pulse $E(t)$ with intensity $I(t)$ and phase $\phi(t)$, we get the complex

frequency-domain pulse field $E(\omega)$:

$$E(t) = \sqrt{I(t)}e^{-i\phi(t)} \overset{F.T.}{\Rightarrow} E(\omega) = \sqrt{S(\omega)}e^{-i\varphi(\omega)}. \tag{21}$$

There, $S(\omega)$ and $\varphi(\omega)$ are the pulse spectrum and spectral phase. The resulting influence of a medium and its contribution to the spectral phase can be modelled[4] as a simple multiplication of $E(\omega)$ by a factor of $e^{i\varphi(\omega)_M}$. The spectral phase $\varphi(\omega)$, accumulated by frequency ω during propagation in medium with refractive index n and length L, can be written as

$$\varphi(\omega) = k(\omega)L = n(\omega)\frac{\omega}{c}L. \tag{22}$$

It can be expanded as Taylor series around the center frequency ω_0:

$$\varphi(\omega) = \sum_m \frac{1}{m!}\varphi_m(\omega_0)(\omega-\omega_0)^m. \tag{23}$$

where $\varphi_m(\omega_0)$ is the m$^{\text{th}}$ derivative of the phase function with units of ps$^{\text{m}}$ or fs$^{\text{m}}$ depending on the amount of dispersion.

The individual terms in the spectral phase expansions will affect the temporal profile of the pulse as follows

- the constant phase offset $\varphi_0 = \frac{1}{v_p}L$ is related to the phase velocity v_p of the pulse and the term will not affect pulses longer than few optical cycles;
- the group delay (GD) term $\varphi_1 = \frac{1}{v_g}L$ is related to the group velocity v_g of the pulse and shifts the pulse in time. Self-referencing pulse characterization techniques like autocorrelation (AC) cannot measure this term;
- the group delay dispersion (GDD) term (and further higher orders of dispersion for that matter) $\varphi_2 = \frac{\mathrm{d}}{\mathrm{d}\omega}\frac{1}{v_g}L$ increase the pulse duration. If $\varphi_{m\geq 2} \neq 0$, instantaneous frequency depends on time and we say the pulses are chirped;
- the third order dispersion (TOD) φ_3 and higher odd dispersion orders add oscillatory structures outside the main pulse envelope;

The key process in CPA is to first stretch the pulse in time by adding a certain amount of dispersion (preferably the GDD, chirping the pulse linearly) and later, after amplification, introduce a dispersion of the opposite sign. The goal is to compensate the modified phase of the stretched pulse and make it as flat as possible to compress the pulse back to its original duration, as only constant spectral phase produce the shortest pulse duration for a given spectrum [80]. Generally, each medium will affect the pulse by adding all orders of dispersion and the devices modifying the pulse spectral phase needs to be designed carefully so that even the higher orders of dispersion are compensated (for example, cubic phase needed to be compensated by prisms in [81] to reach 6 fs from Ti:sapphire laser). Otherwise, the efficiency of the subsequent nonlinear processes depending on the temporal distribution of the energy within the sub-optimally compressed pulse can suffer.

[4]This approach ignores the dispersion effects caused by spatial chirp, but can be used as a first approximation, which will be enough for the lasers described in this thesis.

CFBG stretchers and grating compressors

In L1 Allegra, the CPA technique is based on stretching the pulses in CFBG stretchers and compressing them in Treacy type grating compressors [82] with folded geometry. The advantage of CFBG stretcher is the ability to introduce large amount of dispersion into the pulse in a short length of material (20 cm of fiber) and no need for alignment. With thermo-electric cooling (TEC) elements controlling the temperature across the fiber, dispersion can be tuned to compensate extra phase accumulated inside the laser system due to B-integral. These stretchers are designed to match the dispersion of the compressors up to fourth order and the amount of GDD introduced by them is 269 ps^2 for the last 3 pump lasers in L1 Allegra. In contrast, trying to achieve the same stretch factor with single mode silica fiber at 1030 nm, having material dispersion of 22.5 ps^2 / km [83], would require about 12 km of fiber (with 99.6% losses). Detailed properties and dispersion parameters of the L1 Allegra stretcher and compressor are later mentioned in detail in Tab. 5.

For the purpose of this thesis, it is convenient to define the dispersion in wavelength rather than frequency domain as well. As linear phase in frequency domain is not linear in wavelength domain anymore due to the reciprocal relation $\omega = 2\pi\frac{c}{\lambda}$, transforming the spectral phase terms to wavelength domain uses following relations:

$$\mathrm{D}_2 = -\left(\frac{2\pi c}{\lambda_c^2}\right)\varphi_2. \tag{24}$$

For example the GDD of CFBG stretchers is often defined by dispersion parameter D_2 with units of ps / nm. Knowing the reflection bandwidth of the stretcher or full width at half maximum (FWHM) of the seed spectrum at any point, D_2 then enables quick calculation of stretched pulse duration. Higher order dispersion coefficients D_m for $m > 2$ can be calculated by derivating the previous orders as

$$\mathrm{D}_\mathrm{m} = \frac{\partial}{\partial\lambda}\mathrm{D}_{\mathrm{m}-1}. \tag{25}$$

The result always contains all the lower frequency dispersion coefficients as well. For this reason, when optimizing the spectral phase of a given laser pulse, it is good to start from the highest available order and finish with optimization of GDD.

Time-bandwidth product

In order to calculate the shortest Gaussian pulse duration that can be reached with a given spectral bandwidth, the time bandwidth product (TBP) $\tau\,\Delta\nu$ can be used. It will satisfy the inequality given by the uncertainty principle:

$$\tau\,\Delta\nu \equiv \tau\,\frac{c}{\lambda^2}\,\Delta\lambda \geq \frac{2\ln(2)}{\pi}. \tag{26}$$

The pulses with TBP equal to the value on the right side of the equation are called Fourier-transform or bandwidth limited. For example, the shortest pulse duration of the compressed 1030 nm pulses from one of the 230 mJ RA described later in the thesis with spectrum FWHM of 1.2 nm is 1.3 ps.

3.3 Laser pulse characterization

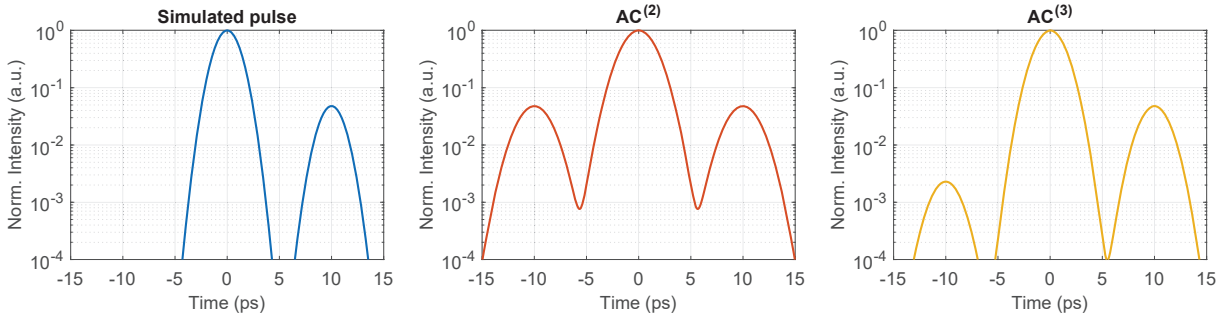

Fig. 9. Second ($AC^{(2)}$) and third ($AC^{(3)}$) order autocorellation of a simulated pulse with FWHM = 2.4 ps having a 5% postpulse at 10 ps. While the second-order autocorrelation cannot distinguish between the prepulse and postpulse, the third-order autocorrelation trace can. Neither of the two methods can be used to retrieve the potential temporal phase of a laser pulse.

In order to be able to calculate the laser pulse intensity, to evaluate or simulate the strength of the nonlinear effects (the SHG efficiency, laser damage threshold or self-phase modulation effects) and to optimize the pulse compression, the amplitude and phase of the pulse needs to be known either in temporal or spectral domain. For certain applications we can use the SHG-Autocorrelator, capable of measuring the temporal autocorellation function of the laser pulse. In it, a replica of the incident pulse is created by a splitter, delayed by an adjustable delay line and both are sent to a nonlinear crystal. There, the SHG signal is generated only when the two replicas of the pulse overlap. The measured intensity trace is always symmetric and cannot distinguish between a pulse with a prepulse or a post pulse. The trace is also ambiguous as different intensity profiles with different phase can generate the same autocorrelation (AC) trace.

In order to distinguish between prepulses or postpulse, a non-symmetric technique needs to be implemented, such as the third order autocorellation [84]. It is frequently used for measuring contrast of the pulses. The difference between the second and third order autocorellation results, generated by a simulated pulse having postpulse with 5% of the intensity is shown in Fig. 9.

To retrieve both intensity and phase of the measured pulse, a technique called frequency resolved optical gating (FROG) can be used. It comprises of the experimental device and an iterative algorithm [85] and the measured FROG trace is basically a spectrally resolved autocorellation trace. In the case of SHG-FROG, the measured trace is still symmetrical and contains an ambiguity in time. This can

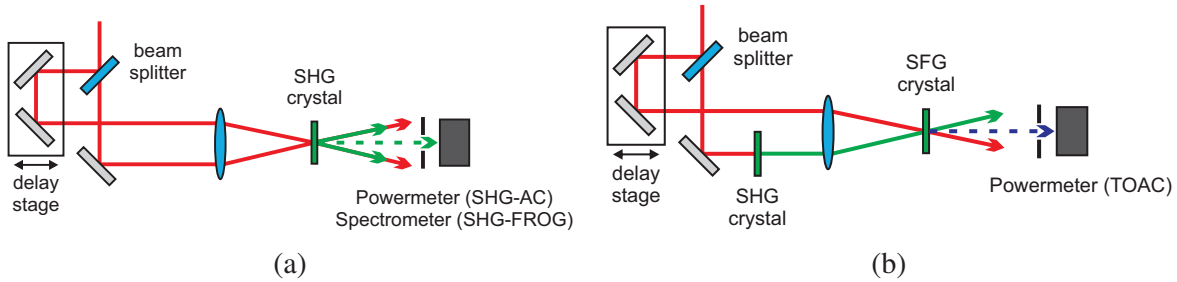

Fig. 10. Layouts of devices for characterization of laser pulse duration. (a) – 2nd order SHG autocorrelator (SHG-AC) using a powermeter to measure the SHG autocorrelation trace. By replacing the powermeter with a spectrometer, an SHG-FROG is realized. (b) – 3rd order autocorrelator layout.

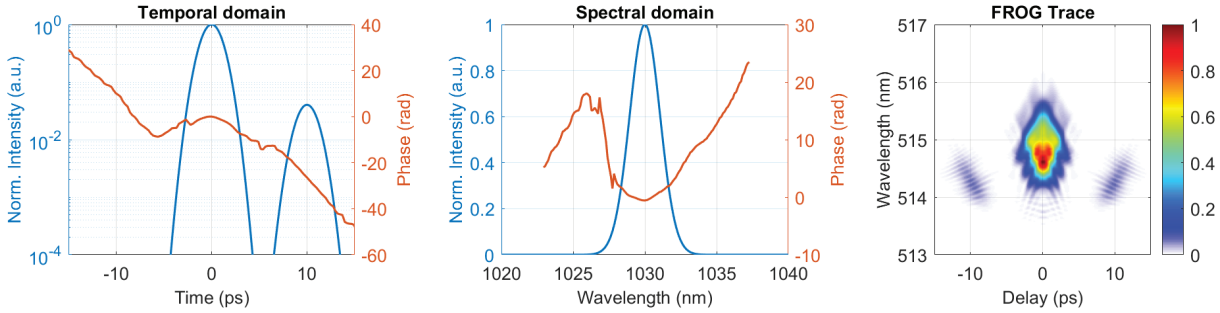

Fig. 11. Simulated FROG trace of a theoretical pulse from Fig. 9, having 5% intensity postpulse. Measured FROG traces can be used by an algorithm to retrieve the pulse spectral and temporal intensity profiles and both its corresponding phases. In this example, the opposite approach was adopted – the temporal and spectral intensity profiles were fixed, the respective phases were iteratively calculated by a similar algorithm used in the FROG method. Measured FROG trace can be used to retrieve the temporal phase of a laser pulse. *FROG trace was simulated by Alexandr Špaček.*

be solved by putting a piece of glass into the beam and comparing the traces with and without the extra material. Although for laser pulses with duration in order of picoseconds, such approach would require the thickness of a glass to be at least 10 m[5]. Basic layout of a typical 2nd and 3rd order autocorrelator and FROG device is shown in Fig. 10.

Retrieving the complex signal $E(t)$ from the FROG trace has a unique solution and the measured FROG trace of the same pulse with 5% postpulse having spectrum with 2 nm FWHM is shown in Fig. 11. Knowing the phase of the pulse is important for optimizing compression of laser pulses, as any residual phase will make the pulse temporal profile different (longer or with wings) when compared to the ideal Gaussian temporal profile. That can affect the SHG efficiency and this problem in particular needed to be addressed during the work described in this thesis.

3.4 Amplification in thin-disk regenerative amplifiers

The main technology used in the pump lasers in L1 system is the Yb-based thin-disk RA, due to its great scalability, generation of high energy pulses at 1030 nm with good beam quality and high average powers. Amplification of laser pulses by using thin-disk technology was developed in 1994 [86]. Small thickness (∼100 µm) much smaller than the area of the active medium (several mm) allows the disks to be backside cooled, while the pump light is entering the disk from the front. That minimizes the effect of thermal lensing. The thickness of the disc limits the single pass gain, which has to be compensated by multiple passes within laser resonator, known as roundtrips. Naming convention "regenerative amplifier" is used for these types of lasers.

The pumping of the thin-disks needs to overcome the limited absorption of the pump light due to the small thickness of the disk. This is solved by imaging the pump spot multiple times on the disk by a system of a parabolic mirror in front of the disk and roof-top mirrors around it. The disk is usually anti-reflection coated for both the signal and pump wavelength in the front and high-reflectivity coated for both wavelengths in the back. This optical setup, together with the disk glued to a water cooled coolfinger of copper or artificial diamond is called laser head and its design is shown in Fig. 12. The disks have usually diameters of several millimeters.

[5]The group velocity dispersion of BK7 glass is 25.1 fs^2 / mm at 1030 nm. To see a change in the FROG trace, dispersion of ∼1 ps^2 would be needed.

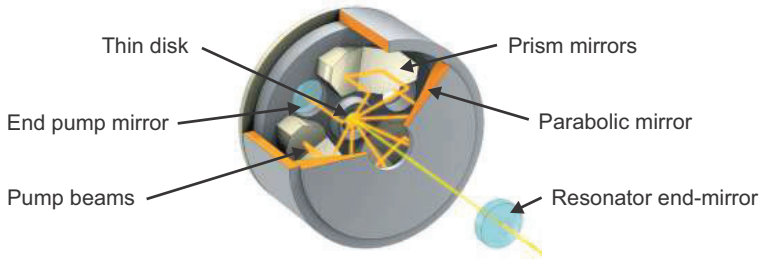

Fig. 12. Layout of the thin-disk laser head and its pumping (courtesy of TRUMPF Scientific lasers).

As an active medium, Yb-doped crystals (YAG and LuAG) are usually used, due to favourable properties of Yb^{3+} ion [86]:

- low quantum defect (8.6%)
- high slope efficiency
- broad absorption bands at 940 nm
- high doping levels possible without quenching[6] (> 20 at.%)
- no excited-state absorption or upconversion
- reliable pump diodes within the absorption region available, even at 969 nm
- long radiative lifetime on the upper laser level (∼1 ms in Yb:YAG)
- broad emission bandwidth (1 ps pulses possible)

RA cavity can be realised in two basic designs - linear cavity and ring cavity (Fig. 13). Ring cavities holds several advantages over the linear cavities. Namely the absence of a Faraday rotator, required to separate input and output beam and absence of isolation needed to protect the seed beampath from the amplified output. Two of the RA developed by Trumpf Scientific for ELI Beamlines L1 Allegra system have linear cavity design, a third prototype developed later has a ring cavity design.

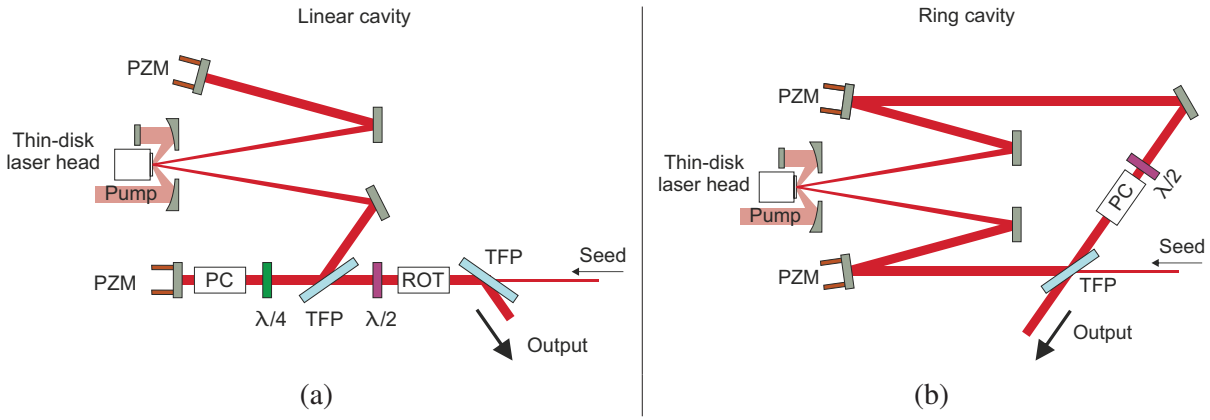

Fig. 13. Layouts of linear (a) and ring (b) cavity RA. PC – Pockels cell, TFP – thin film polarizer, ROT – Faraday rotator, PZM – mirror with piezoelectric adjuster.

[6] reduction of an excited-state population by unwanted effects

3.4.1 Temperature influence on the active medium spectral characteristics

The laser active media with crystal hosts doped by rare-earth elements such as neodymium or ytterbium have narrow peaks in the absorption and emission cross-section spectra. This is due to their specific electron configuration where the outer shell electrons protects the inner ones from the effects of the environment. Varying the temperature of the active media affects these spectral peaks in a several ways:

- The position of the spectral peaks can shift to shorter or longer wavelengths due to thermal expansion of the crystal host [87]. As thermal expansion affects the distance between atoms within the active medium, so does the energy levels position changes and with it, the wavelengths of the energy level transitions.
- The height of the peaks will change as the population of the individual energy levels within the active medium is governed by the Boltzmann distribution, which depends on the temperature. At lower temperatures, the lower energy levels within each manifold are becoming more populated, which affects the effective cross-sections in the absorption and emission spectra.
- The width of the spectral peaks will always decrease at lower temperatures. It is affected by difference in radiation lifetimes, the host atoms influencing the inhomogeneous spectral line broadening and Raman scattering [88].

Relevant for this thesis is the shift of the emission line of Yb:YAG from 1030 nm to higher wavelengths at higher temperatures. The 1030 nm peak typically shifts by 1 nm when the temperature of the thin-disk rises by 200 °C [89]–[91]. In L1 Allegra system, Yb-based RA with output pulse energy of 100 mJ have central output wavelength shifted to 1030.4 nm. RA with output pulse 230 mJ have central output wavelength shifted to 1030.7 nm.

3.4.2 Gain narrowing

Commonly, during the amplification of a laser pulse, not all wavelengths from the seed pulse spectrum will be amplified equally due to the spectral shape of emission line of the active medium. The spectral bandwidth of the amplified seed pulse will get smaller and, as the TBP stays constant, the shortest achievable pulse duration after compression will become longer. The shortest pulse duration limited by the gain narrowing effect can be estimated assuming an unchirped pulse and it depends on the gain G, spectral width of the emission line $\Delta\lambda$, central wavelength λ_c and the bandwidth limited input pulse duration τ_{in} as [92]

$$\tau_{out}^2 = \tau_{in}^2 + \frac{4\ln(2)\ln(G)\,\lambda_c^4}{(\pi c)^2 \Delta\lambda^2}. \tag{27}$$

Using one of the 230 mJ RA, described later in the thesis, the typical values of seed spectrum FWHM, centered around 1030 nm is 3.5 nm, the corresponding input pulse duration is $\tau_{in} = 450$ fs, gain is $G = 10^{10}$, the resulting gain narrowed minimum pulse duration at the output is $\tau_{out} = 1.67$ ps, corresponding to a spectral bandwidth of $\Delta\lambda = 0.93$ nm. The measured spectrum from this laser has a FWHM of 1.1 nm and output pulses can be compressed below 1.5 ps.

Gain narrowing effect can also be simulated by iterative multiplication of the RA input seed pulse spectrum by the emission spectrum of the active medium. To illustrate this idea, I assume an Yb:YAG thin-disk. The emission cross-section coefficients of Yb:YAG around 1030 nm differs slightly in literature, but the idea is captured in Fig. 14 where the seed spectrum with bandwidth $\Delta\lambda = 3.5$ nm is multiplied by the Yb:YAG emission spectrum measured at room temperature in [90], resulting in

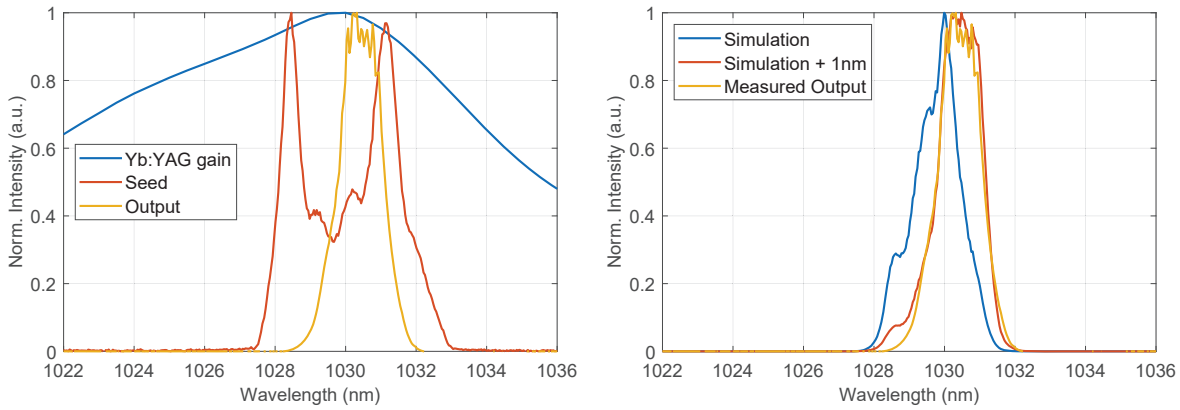

(a) (b)

Fig. 14. Gain narrowing simulation, using seed and output spectrum from the laser described later in section 4.2). (a) – emission spectrum of Yb:YAG around 1030 nm (blue), seed pulse spectrum (red), and output spectrum shifted to 1030.7 nm (yellow), (b) – simulated gain narrowed spectrum (blue and red) with measured output spectrum (yellow). 50 passed through thin-disk were assumed. The Yb:YAG emission spectrum from (a) had to be shifted by 0.55 nm during simulation to match the measured output spectrum.

the gain narrowed spectral bandwidth of $\Delta\lambda = 0.9$ nm. The actual measured spectrum at the output of the RA has a different central wavelength of 1030.7 nm. In order for the simulation to match the measured output spectrum, the gain spectrum of Yb:YAG had to be shifted by 0.55 nm to longer wavelengths. The most porbable cause is the higher thin-disk temperature mentioned earlier section 3.4.1. In Fig. 15, I plot the calculated dependencies between the input spectral bandwidth (FWHM) and output shortest pulse durations for different gain. We can see that even the seed pulses with spectral bandwidth of only 1 nm (with gain of up to 10^{10}) can still be compressed to 2 – 3 ps. This compressed pulse duration is required to reach the designed intensity at the SHG nonlinear crystal plane of 100 GW / cm^2. Knowing this, we were later able to replace the original stretcher in the seed distribution system of L1 Allegra system for an improved one with smaller reflection bandwidth. The improved version had better temperature tunability and with it enabled faster optimization of stretcher dispersion. That affects the compressed pulse duration and presence of prepulses or postpulses.

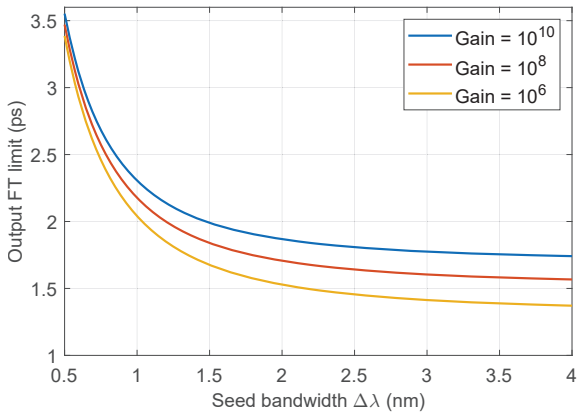

Fig. 15. Shortest output pulse duration dependency on the RA input seed spectral bandwidth. Perfect compression with flat phase assumed.

3.5 Vacuum cleanliness and laser induced contamination

Portion of the L1 laser system is placed in vacuum (see Fig. 2) to avoid self-focusing and turbulence related pointing instabilities in air. Great care should be taken when manufacturing vacuum chambers and placing components inside, as any contamination can lead to undesirable losses of energy inside the system and eventually to catastrophic failure through laser induced damage [93]. Particularly, hydrocarbon (C_xH_y) molecules are undesirable to be present in the chamber as they can contaminate optical components. As a consequence of certain level of contamination present in the vacuum chambers of L1 laser system, several optical components in 1030 nm pulse compressors and SHG stages developed distinct colored features. These laser induced contamination (LIC) features affected efficiency of MLD gratings in pump beams compressors and reflectivity of certain mirrors. Mitigation of this contamination was an important part of my thesis.

To identify potential contamination in vacuum chamber, we can use a measurement technique, called residual gas analysis (RGA). The RGA device contains electrodes producing high energy electrons that ionize the neutral gas molecules and atoms within the vacuum system and a detection system that measures the ratio between the ions charge and mass. The resulting spectrum shows distinct peaks and is a superposition of signals corresponding to a certain ion or ionized molecule with atomic mass units (AMU) on X axis and relative signal proportional to the number of detected constituents on Y axis. Molecules comprised of multiple elements (for example H_2O) will produce signal at multiple AMU (in this case strong peak of H_2O^+ at AMU 18, 5 times weaker peak of HO^+ at AMU 17 and 100 times weaker peak of O^+ at AMU 16). While typical and lighter gas contents are easy to identify and not problematic (O_2, CO_2, Kr, Ne, He, H_2O and others), complex molecules (for example vacuum pumps oils or parts lubricants) can create complex fragmentation (or cracking) patterns and their spectrum can be hard to analyze. Particularly, hydrocarbon (C_xH_y) molecules are undesirable to be present in the chamber as they can contaminate optical components and their presence in the RGA spectrum is recognizable by a comb of peaks with AMU period of 12 (CH_2 group). The processed spectra are usually normalized to AMU peak 44 (CO_2) and the number and height of the peaks above AMU 44 is the main focus of the analysis. In order to improve the cleanliness of chambers and components and minimize the amount of future outgassing, the vacuum chambers and components placed inside them can be baked out at high temperatures.

One of the leading facilities in terms of vacuum cleanliness is the Laser Interferometer Gravitational-Wave Observatory (LIGO) has produced vacuum cleanliness standards, which provide useful guidelines and requirements for RGA spectra. Apart from the list of materials that can be placed in vacuum they specify the main cleanliness criteria, which all the components prior to their placement inside the vacuum environment have to fulfill, as follows [94]:

- The ratio between the amplitude of the peaks with AMU 44 (CO_2) and AMU 43 (hydrocarbon C_3H_7) is below 1/10.
- The amplitude of peaks above AMU 44 is $\leq$ 1/100 of the AMU 44 peak.
- There are no "significant" high AMU components above the background or instrument noise floor (even if < 1/100'th of AMU 44) up to AMU 100.

A typical RGA spectra of the compressor vacuum chamber from the L4 laser system at ELI Beamlines containing some heavy contaminants creating complex fragmentation pattern is shown in Fig. 16. Initially, multiple peaks above the 1/100 value of peak 44 are visible, including the complex pattern with AMU 12 period, suggesting a hydrocarbon contamination. After running the vacuum pumps for 12 days, most of the contamination got pumped down. Still, this vacuum chamber does not comply with the LIGO cleanliness criteria due to a presence of peak at AMU 43, which is above 1/10'th of

peak 44, as well as due to a presence of multiple peaks with AMU 50, 55, 57, 58 and 69, still indicating the presence of hydrocarbon contamination (probably a pump oil, according to the reference cracking pattern table [95]).

This described detailed cleanliness analysis and care was not taken when the L1 vacuum system was designed and constructed. As a result, contamination issues had to be addressed during my PhD study and are further described in section 4.5.3.

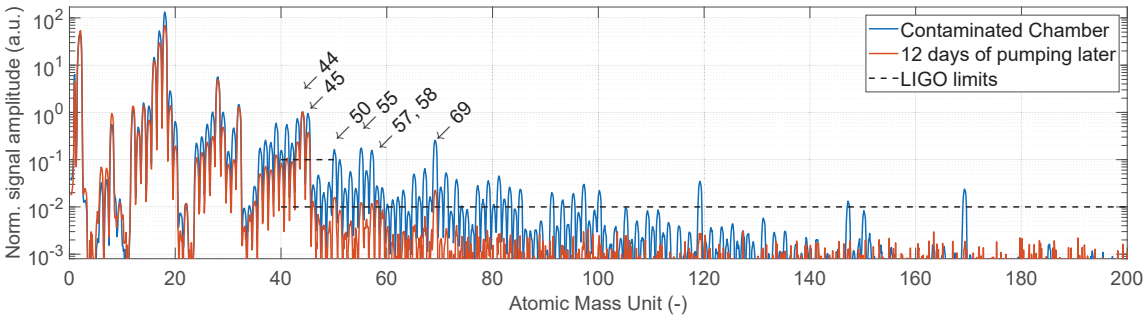

Fig. 16. The RGA spectra of the L4 compressor chamber. Even though the situation improved after 12 days of pumping, the chamber was not considered clean enough according to the LIGO standards and further cleaning procedures had to be carried out. Data are normalized to peak with AMU 44. *Data provided by Petr Szotkowski.*

4. Pump lasers for L1 Allegra

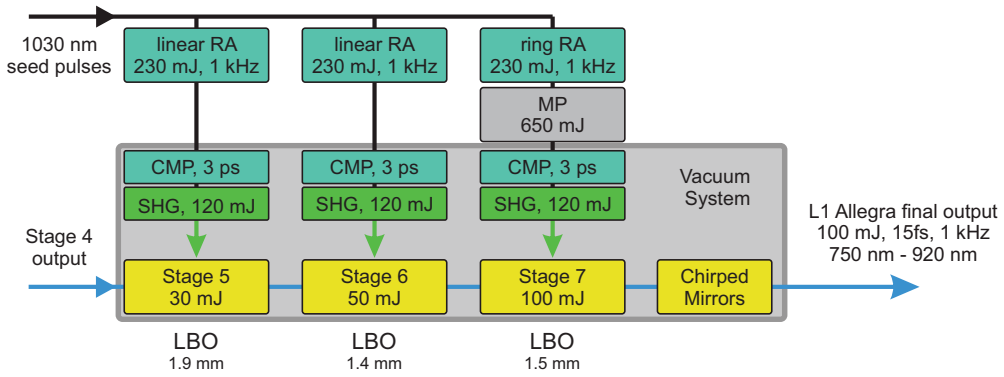

Fig. 17. Pump lasers for L1 Allegra layout with designed parameters. CMP – compressor.

L1 Allegra laser system is comprised of 7 OPCPA stages that are pumped by 5 pump lasers. All of them use diode pumped Yb-doped thin-disk RA to generate 1 kHz pulses at 1030 nm, MLD grating compressors to compress the RA output pulses to 2 – 3 ps and LBO crystals for SHG of pulses at 515 nm. The first two pump lasers for stages 1 – 4 were developed together with their RA as part of Jakub Novák's dissertation thesis [54]. The last three pump lasers use commercial RAs. These RA needed to be integrated to the system and tested, their beam transport, diagnostics and vacuum pulse compressors with SHG stages needed to be built. This integration, commissioning and later also improvements of the SHG efficiency were the main goals of this part of my thesis. This section mentions all the parameters of the three pump lasers (RAs, compressors and SHG stages, including the initial results). It then describes the steps taken to improve the SHG efficiency, temperature stability of the SHG mounts, beam profile improvements of two RAs with linear cavity and to mitigate the LIC.

The pump lasers are based on commercial Yb-doped thin-DIsk Regenerative Amplifiers (the manufacturer's naming convention is DIRA 200 – 1) from TRUMPF Scientific lasers, operated at 230 mJ, 1030 nm, 1 kHz and pulses stretched to about 500 ps before compression. The 230 mJ output energy was a technological limit, given by the B-integral in the cavity, laser induced damage threshold (LIDT) of intra-cavity mirrors, and thermal distortions allowing to keep the output beam quality factor M^2 below 1.2. Assuming compressor efficiency around 90% and SHG efficiency of 60%, the designed output energy at 515 nm was 120 mJ at 3 ps, 1 kHz. The compressors and SHG stages with LBO crystals for frequency doubling were placed inside vacuum chambers, to avoid problems with self-focusing of pulses at high intensities. The layout is shown in Fig. 17.

The first two of the RA from TRUMPF were delivered to ELI between 2014 and 2016. They had a linear cavity design, matching in principle the one described in Fig. 13a. The third RA was delivered in 2017 with an improved ring cavity design and multiple upgrades, based on the experience from the first two.

In order for the L1 system output to reach 100 mJ at 15 fs, a multi-pass booster amplifier is planned after the final RA. This upgrade should later boost the energy of the pump pulses of the last pump laser to about 650 mJ at 1030 nm or 300 mJ at 515 nm and is currently being constructed. Some of the improvements introduced during my work were designed with this upgrade already in mind. All 7 OPCPA stages were tested at one point, reaching 55 mJ out of the designed 100 mJ at the end of L1 system. This result was limited by the energy from the last three pump lasers at 515 nm, reaching only 100 mJ.

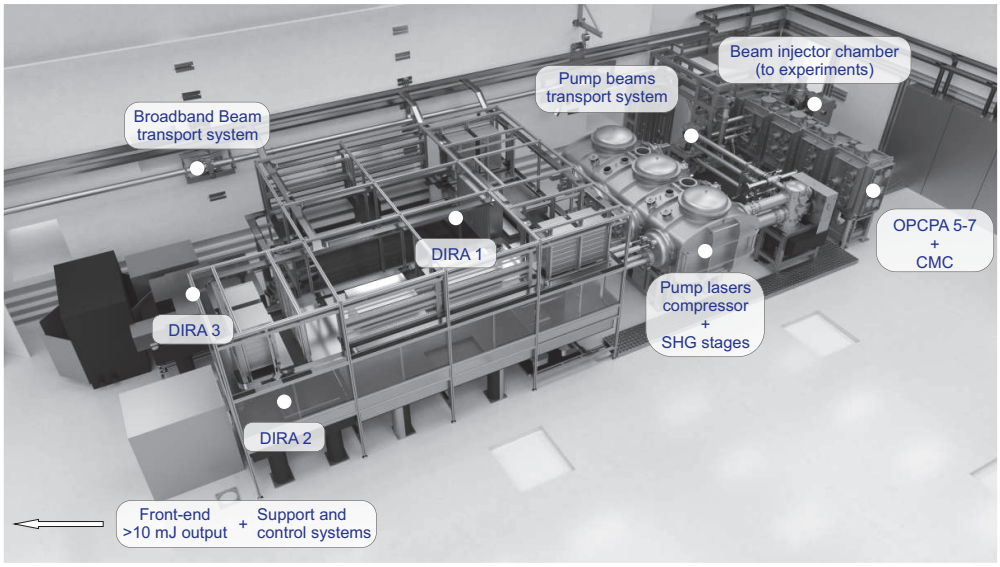

Fig. 18. Rendering of L1 beamline. Render contains 3 RA (DIRA 1 – 3) with their beam transport covered by the table enclosure system, pump beams compressor chamber with SHG stages, two smaller chambers and vacuum beam transport tubes for three beams at 515 nm. On the right side is the vacuum chamber housing the last 3 OPCPA stages with chirped mirror compressor (CMC) and also injector chamber, sending the compressed broadband signal pulses down to E1 experimental hall.

The sections that follow describe the seed distribution system with Ti:sapphire oscillator at the beginning, performance of the three RA themselves, results with compressed pulses and the SHG results (with emphasis on laser parameters, affecting the pump laser performance). Separate sections are dedicated to temperature stabilization of SHG mounts, improvements of the RA output beam profile, contrast of fundamental pulses, and to cleanliness of the vacuum chamber.

4.1 Seed generation

Seed pulses for the pump lasers are generated inside the Ti:sapphire oscillator (Femtosource Rainbow CEP). The broadband (750 – 920 nm) output pulses from the oscillator are used as signal to be amplified in the OPCPA stages. By focusing portion of the output into a few mm long magnesium oxide-doped periodically poled lithium niobate (MgO:PPLN) crystal, the spectrum is broadened by SPM. Portion of the broadened spectra around 1015 nm is then picked by a filter and coupled into a fiber in the seed distribution system. The resulting spectrum is shown in Fig. 19a. By using a single oscillator as a common source of both signal and seed pulses, their basic synchronization later in the OPCPA stage is assured. The temporal overlap of signal and pump pulses inside the nonlinear crystals with femtosecond precision is achieved using in-house developed optical crosscorellators [96]. Without this effort, the temporal (as well as spatial) jitter and long-term drift between the signal and pump pulses limits the OPA efficiency and affects the shape of the OPA output spectrum.

The seed distribution system of L1 Allegra laser system for stretching of the 1030 nm pulses and their delivery to individual RA is described in the published paper here [97] and only the key components will briefly be mentioned. Following the layout in Fig. 20, the 80 MHz seed pulses from the Ti:sapphire oscillator (spectrum is shown in Fig. 19b) were originally stretched in a CFBG fiber stretcher (Teraxion), introducing negative dispersion of $-477\,\mathrm{ps/nm}$ with a reflection bandwidth of

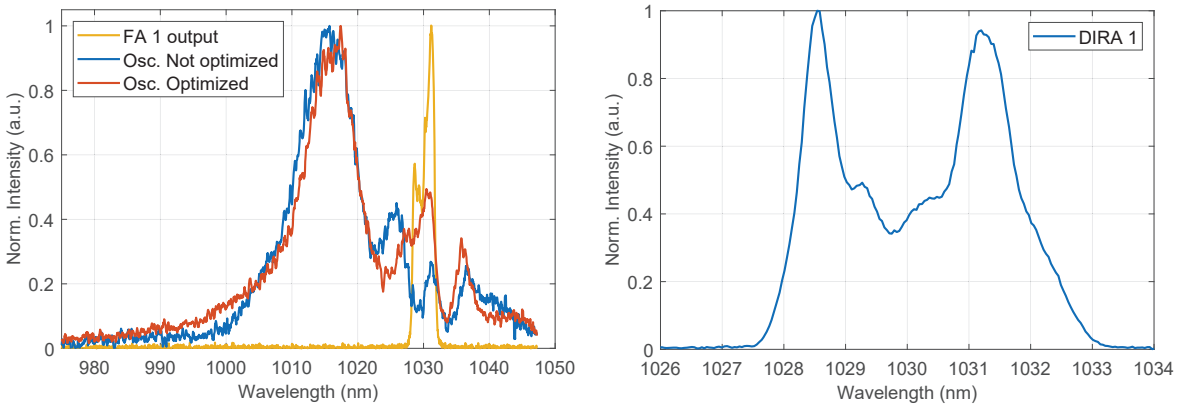

(a) (b)

Fig. 19. Portion of the Ti:sapphire output spectra, spectrum after the first fiber amplifier (FA 1) and a typical spectrum of the seed pulse, (a) – portion of the broadened spectra generated in the Ti:sapphire oscillator. Depending on the oscillator performance and pointing into the MgO:PPLN crystal, the seed distribution input spectra shape can differ (red and blue). Only a portion (10%) of the Ti:sapphire output spectrum around 1030 nm is amplified in FA 1 (output spectrum in yellow) due to a spectral filter inside the amplifier. (b) – typical spectrum of seed pulses at the input of the RA. The dip in the middle of the spectra is a result of the first two FAs in the seed distribution system.

3.5 nm (FWHM). Such a stretch factor was chosen to avoid problems with nonlinear effects otherwise caused by short pulses inside the RA cavity. This resulted in an 80 MHz train of pulses with roughly 1.7 ns pulse duration separated by 12.5 ns. The dispersion of this stretcher was tuned by an in-house built setup with TEC elements (with details described in section 4.3). This solution was later replaced by an improved stretcher module from Teraxion. Although the reflection bandwidth of the new stretcher is only 2.5 nm, it is still sufficient to support pulse durations below 2 ps (see Fig. 15).

An acousto-optic modulator is used in the seed distribution system to create 10 µs bursts of 80 MHz

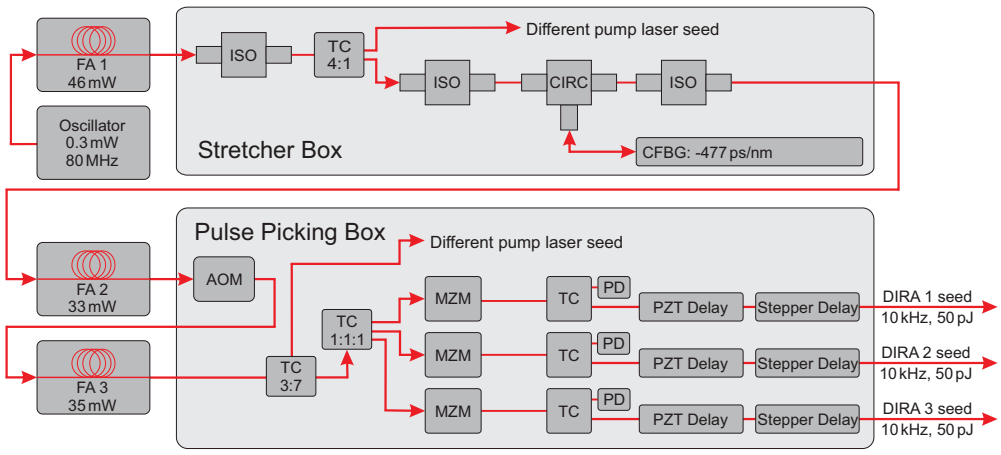

Fig. 20. L1 Seed distribution layout. Oscillator – Ti:Sapphire module generating 1030 nm, FA – fiber amplifier, ISO – isolator, TC – tap coupler / divider, CIRC – circulator, CFBG – fiber stretcher with Bragg grating, AOM – acousto-optic modulator, MZM – Mach-Zehnder modulator, PD – photodiode, PZT Delay – fine tunable fiber delay using piezo effect for changing the fiber length.

Tab. 3. Seed pulse energy for all 3 RAs. The combination of a fiber isolator and a fiber collimator introduces high losses. Thus, the available seed energy from the seed distribution system and at the input to RA cavity differs.

Seed pulse Energy/Power	Single pulse (10 kHz)	RA cavity input
DIRA 1	54 pJ	12.5 pJ
DIRA 2	58 pJ	14.3 pJ
DIRA 3	56 pJ	29 pJ

pulses with repetition rate of 10 kHz, which are later amplified by the third FA from layout in Fig. 20. This solution was chosen in order to be able to provide seed pulses with enough energy to 4 different RAs while keeping the seed average power within safe limits for the FA 3. When full power operation of the RA is needed, a Mach-Zehnder modulator (MZM) in the seed distribution is used to pick one pulse from the burst for seeding the RA, at which point the seed pulses have energy around 50 pJ. The spectrum of seed pulses at the input to RA is shown in Fig. 19a. Instead of picking a single pulse, the interferometer can be set to let the complete burst pass. This increases the average power and is used for characterization of the seed and cavity alignment of the RA.The individual pulse energies available for each of the RA are in Tab. 3.

After the MZMs, the seed pulses travel through fiber delay stages, that form part of the feedback loop with optical cross-correlators to ensure temporal overlap of signal and pump pulses in OPCPA stages. After the delay stages, the seed pulses passes through a fiber isolator and are then coupled into the RA cavities with a collimator. This last portion of the seed distribution can introduce losses between 48 – 77%. Later in the conclusions, I recommend replacing these parts for some with lower losses.

Ti:sapphire performance

One of the major downsides of using a Ti:sapphire oscillator for generating seed pulses for 1030 nm RA is the limited amount of energy available at this wavelength. Although the FA requires the input pulse energy to be above 1.25 pJ, the highest available energy at 1030 nm is only about 0.25 pJ. This causes the first FA in the seed distribution system to always generate certain amount of ASE.

On top of that, the day to day performance of our oscillator is not always the same. The amount of energy available for the seed distribution system at 1030 nm gradually decreases over a few days, sometimes it can degrade within several hours. This is caused by gradual crystal surface contamination. It is usually solved by either physically moving the crystal to a new position by moving the crystal holder or by cleaning the faces of the Ti:sapphire crystal. Typical example of the seed energy degradation during a day and its recovery by turning the oscillator off and cleaning and shifting of the Ti:sapphire crystal is shown in Fig. 21a.

When the energy at 1030 nm decreases, the first FA introduces higher amount of ASE into the system. With the degradation of the oscillator performance, the total energy of the 1030 nm seed pulses decreases as well (see Fig. 21b), which in turn negatively affects the SHG efficiency. Amplifying pulses with tens of picojoules to 230 mJ requires gain around 10^{10}. Such amplification is possible, but when compared to similar laser systems having lower gain (being seeded by pulses with higher energy), the ASE generated as a consequence inside our RA is higher. RA will also amplify whatever ASE is already present in the seed pulses. I show later in section 4.5.5 how the frequency doubling efficiency of 1030 nm pulses suffers from excessive ASE and how the contrast of compressed 1030 nm pulses depends on the gain in the RA. For the best pump laser performance, the RA needs to be

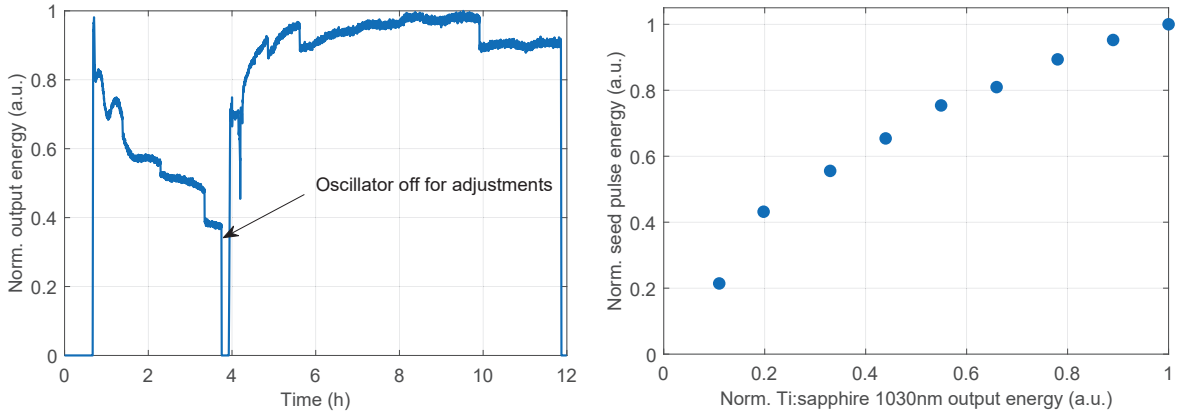

(a) (b)

Fig. 21. Ti:sapphire oscillator output performance. (a) – After degradation to below 40% of the total output after 4 h, the crystal was cleaned and shifted, (b) – seed pulse energy at the input of the RA, dependent on the 1030 nm oscillator output.

seeded with a clean pulse with as low ASE and with as high seed energy as possible from the seed distribution system. I discuss the necessary improvements of the seed distribution system to achieve this in our system on page 83.

The issue of degrading oscillator performance made all the SHG efficiency measurements difficult. For example, an energy drop at 515 nm could be explained by decreased performance of the oscillator rather than by changed parameter of the RA.

These days, laser systems based on a single common Yb-based modelocked oscillator exist. The IR output pulses from these oscillators are directly used as seed pulses for pump lasers. In order to generate the broadband signal pulses for OPCPA stages, these systems utilize supercontinuum generation driven by the pump laser rather than a Ti:sapphire oscillator. One of such systems is the Sylos system at ELI Alps [44], using OPCPA scheme with signal and pump pulses with duration of 100 ps and 1 kHz repetition rate. In order to address the issues with the Ti:sapphire oscillator as the source of seed pulses for pump lasers, we are considering two options. One would be to use the Yb-based oscillator as a source of seed pulses while synchronizing it with the Ti:sapphire oscillator, which provides the signal pulses for OPCPA. Another option would be to replace the Ti:sapphire oscillator completely and utilize supercontinuum generation for signal pulses. Experiments testing both possibilities are planned in the near future.

4.2 Regenerative amplifiers

The three RA from TRUMPF Scientific lasers are designed to generate 230 mJ, 1030 nm at 1 kHz with $M^2 < 1.2$. Photo of the system with linear cavity design is shown in Fig. 22. Layout details are proprietary information and cannot be presented here. Nevertheless, all three RA (two are based on a linear cavity, one on a ring cavity design) follow the well known and widely used designs of RAs with key elements of each type described earlier in Fig. 13.

Each of the three cavities include a single laser head with a Yb-doped thin-disk mounted on a cooling finger with a diamond substrate. The disks are pumped by two diode modules at 940 nm at 1 kHz repetition rate (each module can provide up to 2 kW of average power). All 3 systems have similar output characteristics (see 4). For this reason, I usually show the measured data from DIRA 1 only.

Fig. 22. DIRA 200 – 1 photos from [98]. Details of the layout and cavity design are proprietary information of TRUMPF Scientific lasers and cannot be disclosed.

The linear cavity length is about 11 m with roundtrip time of 72 ns. The seed pulse is kept in the cavity by the Pockels cell (PC) for about 50 roundtrips and amplified (typical build-up is shown in Fig. 23a) to 230 mJ (gain of $\sim 10^{10}$). The output pulses have to travel through a Faraday rotator in order to be coupled out as the linear cavity design requires the output pulse polarization to be rotated (see Fig. 13 for details). A set of motorized $\lambda/2$ waveplate with thin-film polarizer (TFP) controls the amount of output power from the laser. One of the last optical components inside the RA is the output telescope, magnifying the beam diameter in order to reach the designed pulse intensity of 100 GW / cm^2 after compression on the SHG crystal. All the RAs have M^2 of 1.2 or better in both axes, with a typical measurement shown in Fig. 23b. The key parameters of each of the RA are listed in Table 4.

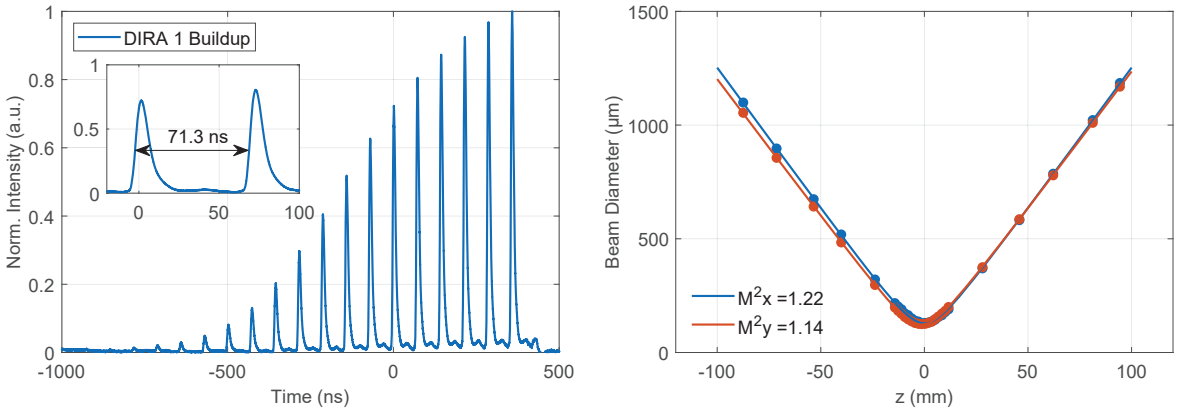

(a) (b)

Fig. 23. DIRA 1 pulse build-up and beam quality, (a) – A typical build-up of energy inside the RA cavity of DIRA 1, roundtrip time of 71.3 ns. (b) – a typical M^2 of DIRA 1 at 1030 nm before compression, measured at output energy of 230 mJ with a lens having a focal distance of 1000 mm, Newport FMS300CC Motorized Linear Stage, and BeamGage camera BGP-GIGE-SP920G.

Tab. 4. Key parameters of the three RA with the latest settings (DIRA 3 beam diameter was increased by a diverging mirror in preparation for the multipass upgrade experiments). The amount of ASE was estimated from temporal profile of the RA output pulse, measured with a photodiode and an oscilloscope. σ – standard deviation.

Parameter	DIRA 1	DIRA 2	DIRA 3	
Cavity design	linear	linear	ring	
Seed pulse energy	12.5	14.3	29	[pJ]
Output power	230	230	230	[W]
Long-term power σ	0.2	0.2	0.2	[%]
Pulse to pulse energy σ (1030 nm)	~ 1	~ 1	~ 1	[%]
Gain	18.4 x 10^9	16.1 x 10^9	7.9 x 10^9	[-]
Roundtrip time	71.5	72.1	74	[ns]
Cavity length	10.7	10.8	11.1	[m]
Number of roundtrips	53	50	50	[-]
PC $\lambda/2$ Voltage	7400	6300	7500	[V]
Highest prepulse	< 0.3	< 0.3	< 0.3	[%]
Highest postpulse	< 2	< 2	< 2	[%]
M^2 in X/Y	1.22 / 1.14	1.37 / 1.16	< 1.2	[-]
Output beam X/Y diameter[a]	11.3 / 10.9	10.2 / 10.3	12.1 / 11.9	[mm / mm]
Beam X/Y diameter on LBO[b]	13.1 / 13.3	12.7 / 10.8	17.9 / 17.9	[mm / mm]

[a] @ $1/e^2$, measured with BeamGage camera BGP-GIGE-SP920G
[b] @ $1/e^2$, calculated from diagnostics leakage with Basler camera acA1600-20gm.

Output spectrum central wavelength

The output spectra of the RAs in Fig. 24a are affected by gain narrowing as the spectrum FWHM of the pulses (and original stretcher at that point) decreased from 3.5 nm to 1.1 nm. The output wavelength of the 230 mJ RA is shifted by 0.3 nm to longer wavelengths when compared to the output spectra of two other in-house built thin-disk RA generating double pulses with 50 mJ. This could usually be explained by two factors. One being the etalon effect in plan-parallel thin-disk and second being the shift of the gain spectral bandwidth towards longer wavelengths at higher temperature of the active medium.

The etalon effect, observed in plan-parallel disks [99], can (for 3 degree angle of incidence of cavity mode on the disk) suppress the gain at 1030 nm and prefer 1030.7 nm. We know all our disks are wedged and the etalon effect was not the reason for shifted output spectrum.

To assess the influence of the disk temperature on output spectra, I used FLIR ONE thermal camera. I monitored the temperature in the center of the disk of DIRA 1 while pumping at 940 nm with no lasing in the cavity. Starting at 21 °C with no pumping, the temperature of the disk rose to 80 °C at 50% of pump setpoint and the data are shown in Fig. 24b. The final setpoint during fullpower operation of RA is usually around 69%. Linear extrapolation of the data shown in Fig. 24b estimates the final temperature of the disk as 110 °C. Similar disk temperatures were measured in [100] where a temperature difference of 120 °C was reached in a ∼ 200 µm thick Yb:YAG disk pumped by 1.5 kW at 969 nm. Taking into account the temperature effect on spectral peaks described earlier in section 3.4.1, such a temperature difference would shift the gain spectrum of Yb-doped active media by more than 0.5 nm to longer wavelengths.

The other two RAs providing the 2 x 50 mJ mentioned in Fig. 24a are pumped at 969 nm with about 500 W of incident power over the disk (instead of ∼ 2 kW in DIRA). This means lower heat deposited inside the disk due to quantum defect. The maximum measured disk temperature of one of the 2 x 50 mJ RA show at least 25% lower value when compared to maximum DIRA disk temperature. The most probable reason for this temperature and spectrum shift difference is the difference in thin-disk thickness between the RA, with DIRAs having thicker disks.

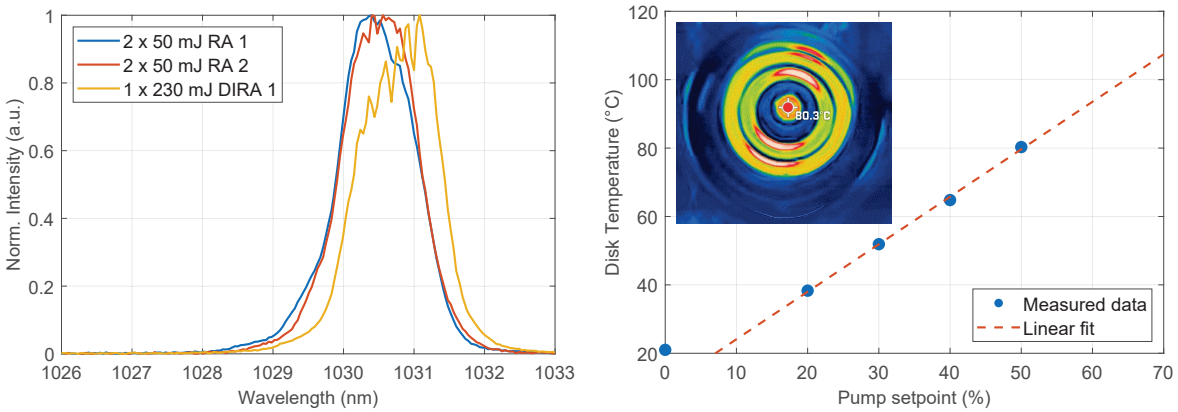

(a) (b)

Fig. 24. RAs output spectra and temperature of the disk. Spectrometer – Ocean Insight HR4D2250 with 0.15 nm resolution, thermal camera – FLIR One (a) – Output spectra of two DIRA 1 and two other in-house built RAs. Central wavelength is $\lambda_c = 1030.4$ nm for RA 1 and RA 2 and $\lambda_c = 1030.7$ nm for DIRA 1, (b) – DIRA 1 Disk temperature at different pump levels without lasing. Inset – thermal camera image at 50% pumping.

Shifted output spectrum of RA will affect the pulse compression and affect the dispersion tunability of the stretcher designed for 1030 nm. This issue, which limits the SHG efficiency, is further described in section 4.3.

Cavity energy stabilization

Each RA is equipped with an internal photodiode (PD) monitoring the energy inside the cavity. PID loop then stabilizes this energy reading by modulating the power of the pump diodes. This feedback loop can compensate long-term drifts and speed up the warm-up time of the RAs. By keeping the cavity energy constant, it also ensures constant accumulated phase due to B – integral. This keeps the pulse duration after compression stable, which prevents the SHG efficiency from changing due to a different intensity on the LBO crystal. A typical graphs of the RA cavity and output energy for the case with active stabilization off and on is shown in Fig. 25. Cavity energy was measured by an RA internal PD, output energy was measured by an external PD outside the RA.

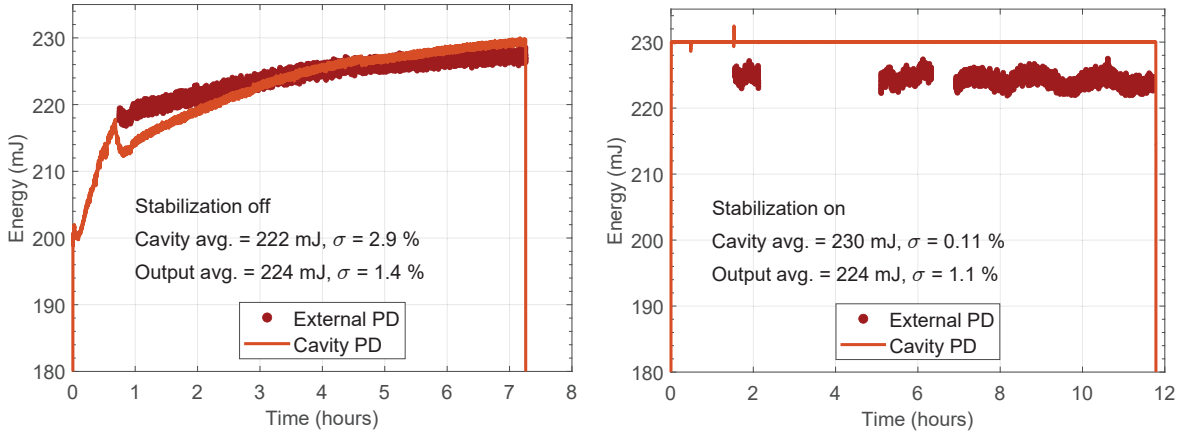

Fig. 25. Comparison of DIRA 2 cavity energy and output energy with diode pump stabilization loop off and on. The stabilization loop speeds up warm-up time and compensates for long-term drifts. External PD data plotted only at maximum output energy from DIRA 2. (a) – Loop off, (b) – Loop on, missing portions of the output energy data caused by minimized output from DIRA 2.

ASE and prepulses at the output of the RA

One important aspect that can affect the SHG efficiency is the amount of ASE around the main pulse at the output of the RA. The main portion of ASE originates from the seed distribution system and gets further amplified in the RA. It is visible as 10 – 15 ns pedestal around the main output pulse when measured with a fast PD (EOT ET-4000F, rise-time < 30 ps) and an oscilloscope with enough bandwidth (Agilent-Infiniium 16 GHz oscilloscope). An example of two RA output pulse measurements on different days with differently strong ASE pedestals is shown in Fig. 26. The duration of the ASE pedestal in this example is related to the opening window of the MZM in seed distribution system.

The height of the pedestal is mostly affected by the performance of the Ti:sapphire oscillator. Since the output spectrum of the oscillator used for pump lasers seed is not centered at 1030 nm (Fig. 19b), only a limited amount of energy is utilized during amplification in the first FA. Depending on the oscillator performance and FA input fiber coupling, the useful seed average power for the FA can be as low as 5 – 25 µW at 80 MHz. The minimum seed power requirement from the FA datasheet is

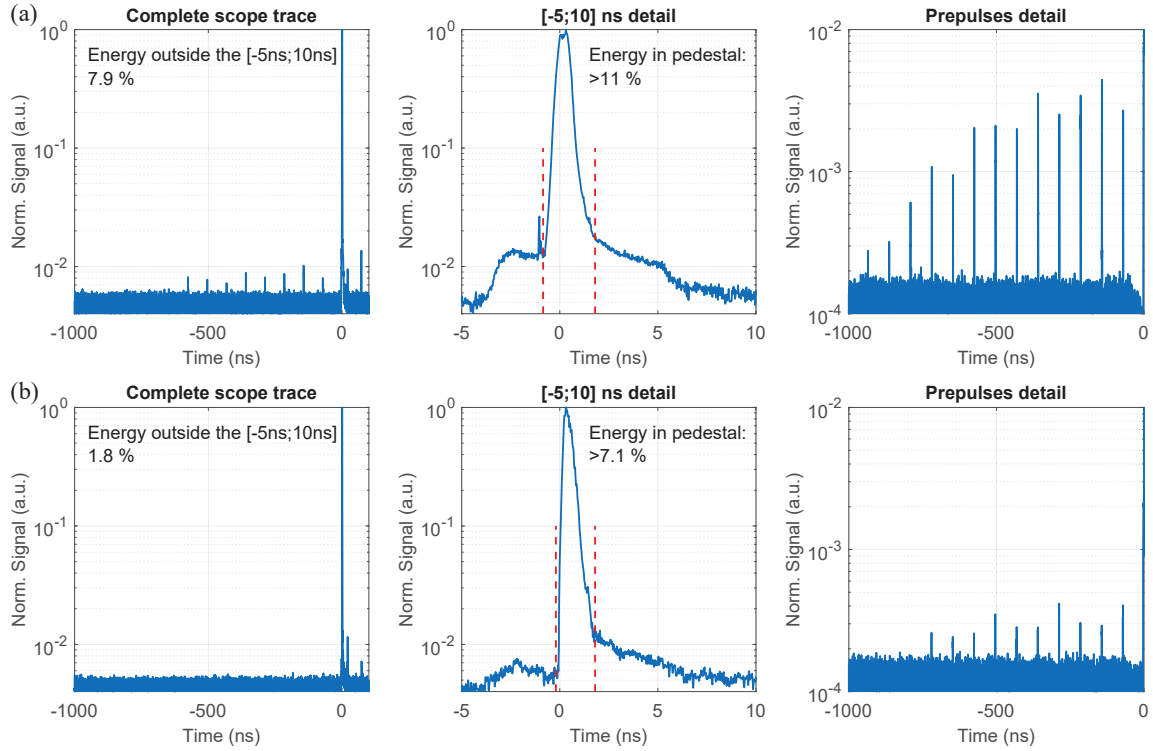

Fig. 26. The output pulses of DIRA 2 recorded over two different days with different Ti:sapphire oscillator performance. Measured at the same output energy with the same signal level on the oscilloscope. Prepulses are one cavity roundtrip (~ 72 ns) apart and are caused by leakage through the cavity TFP. The height of the prepulses and postpulses is affected by cavity and the consequent PC crystal alignment. It is not affected by the oscillator performance and is not related to the ASE level. (a) – day 1, (b) – day 2.

100 µW. Simulation of the amount of ASE generated inside the first FA show that ASE can be as high as 25% of the output signal [101]. It is no surprise that the output pulses from RA contain ASE pedestals as a consequence of this. Usually, around 5 – 10% of total output energy can be contained within the pedestal. As a consequence of this, the contrast of the 1030 nm pulses after compression is affected (shown later in Fig 41b). Without a well performing oscillator the SHG efficiency of the pump lasers is lower and the problem is further described in section 4.4. An experiment confirming that the amount of ASE can be decreased by using a different frontend with Yb:fiber modelocked oscillator is described in section 4.5.5 and key improvements to the seed distribution system are later suggested on page 83.

The ASE originating from the RA itself, rather than from the seed distribution is visible either as a gradually growing baseline in the measurement of RA pulse build-up inside the cavity or as pedestals of the Q-switch (~ 100 ns) duration around the output pulse. Both examples are shown in Fig. 27, which illustrates the extreme case with seed pulse energy below 20% of the usual value. Such low value was achieved by deliberately decreasing the amplification in the last FA in the seed distribution system. The ASE pedestal from the RA is clearly present. This pedestal is usually not visible on the PD and oscilloscope measurement of the output pulses, suggesting the ASE added by the RA is usually lower than the ASE originating from the seed distribution system itself.

One of the other aspects that could affect the SHG efficiency is the amount of energy contained in prepulses and postpulses. The height of the prepulses for the same signal level in two different days

with two different PC crystal alignment and voltage level is shown in Fig. 26. The highest prepulse should, according to the experience of the RA manufacturer, be lower than 0.3% of the total signal height while the height of the postpulse should be lower than 3%. Otherwise a significant portion of the energy will not be contained in the main pulse. This can be affected by optimizing the PC crystal alignment, the PC crystal voltage and the rotation of the waveplate next to it. The quality and the orientation of TFP in the RA cavity can also play a role.

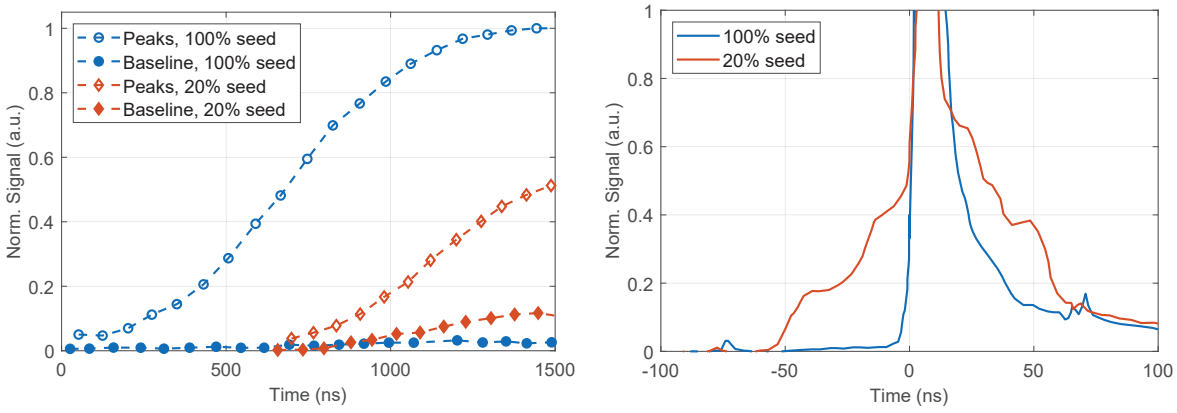

(a) (b)

Fig. 27. RA ASE contribution to build-up and output pulse traces. RA seed pulse energy was decreased by more than 80% by changing the gain of the last FA in the seed distribution. (a) – pulse build-ups for different relative seed energy. Empty markers indicate the top of each build-up peak, filled markers indicate the bottom baseline. The baseline indicates how much ASE is generated in the RA. (b) – output pulse for different relative seed energy. Measured at the same signal level. With lower seed energy, output pulse contains a visible ASE contribution originating from the RA.

4.3 Pulse Compressor

In order to reach the designed intensity for efficient SHG of 100 GW / cm^2 at the LBO crystals, output pulses from RAs are compressed to 1.5 – 3 ps. Compression is achieved via a Treacy type compressor with MLD gratings. A grating compressor based on Treacy design and MLD gratings when compared to compression by volume Bragg grating is larger, but can handle high average powers and high energies easily. In order to shrink the footprint of the required 4 m beampath between the two MLD gratings of each compressor, the geometry is folded by an extra mirror between the gratings and the optical layout of the compressor for one of the RA is shown in Fig. 28. The key parameters of the compressors are listed in Tab 5. The compressor for DIRA 2 and DIRA 3 laser have different optics dimensions, as they are designed to handle 1 J pulse energy. This supports any potential upgrades in the future (the main one being the 650 mJ pulses from the multipass upgrade of DIRA 3 laser). With the RA output spectrum with FWHM around 1.1 nm, the compressor allows compression of the 1030 nm pulses to 1.4 ps. During L1 Allegra system operation the pulses are usually compressed to 3 ps (while being negatively stretched). Originally, the main reason for 3 ps duration was to keep the beam diameter smaller without using optics with larger apertures. Compressing to 3 ps also prolongs the life of optical components, allows safe operation below LIDT values of optics and matches the 3 ps signal pulse duration in OPCPA stages 5 – 7. During optimization and SHG efficiency measurements, the pump pulses had to be compressed to shorter pulse duration between 1.4 – 2 ps. The reason was lower contrast and lower energy contained in the main RA output pulse and the consequent lower intensity on the LBO crystal.

Tab. 5. Key parameters of the three compressors for 1030 nm pulses from DIRA 1 – 3. CMP – compressor, η – efficiency. The GDD value in brackets is related to units in wavelength domain.

	DIRA 1 CMP	DIRA 2 CMP	DIRA 3 CMP	Units
Grating 1 dim.	84 x 96 x 25	154 x 134 x 30	154 x 134 x 30	[mm^3]
Grating 2 dim.	150 x 70 x 25	230 x 100 x 40	230 x 100 x 40	[mm^3]
Central wavelength, λ_c		1030		[nm]
Groove density, b		1740		[mm^{-1}]
Angle of incidence, β		62		[°]
Diffraction angle, β'		-65.4		[°]
Diffraction order		-1		
Gratings separation, d		1655		[mm]
GDD, $\varphi^{(2)}$		269 (-477.2)		[ps^2 (ps / nm)]
TOD, $\varphi^{(3)}$		-4.62		[ps^3]
FOD, $\varphi^{(4)}$		0.13		[ps^4]
Gratings avg. η		97		[%]
Compressor η	86	86	82	[%]
Min. pulse duration, τ	1.6	1.5	1.4	[ps]

Each of the three 1030 nm pulse compressors for DIRA 1 – DIRA 3 are placed on two separate levels of an optical bench comprising of two optical tables and the bench is placed inside a vacuum chamber[7] (photo of the open chamber is shown in Fig. 29a). The layout of the vacuum chambers related to compression, frequency doubling and the subsequent transport of 515 nm pulses is shown in Fig. 30. This configuration avoids transmission of high intensity pulses through vacuum windows and the associated nonlinearities. It also eliminates self-phase modulation and self-focusing effects in air, which would otherwise corrupt and focus both 1030 nm and 515 nm laser pulses over the distances we are using.

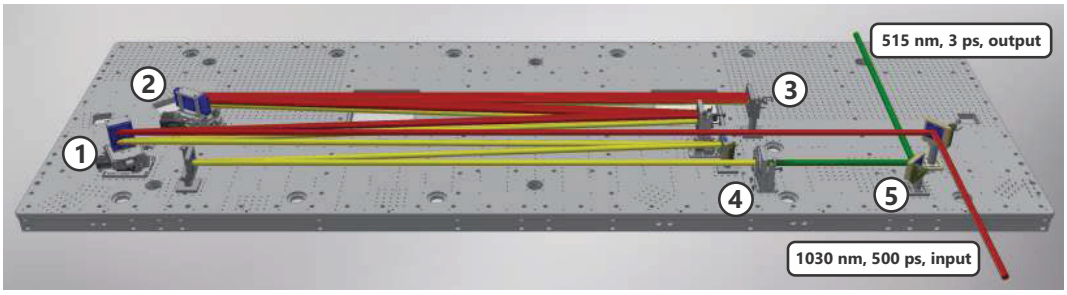

Fig. 28. DIRA compressor layout inside the chamber. The table dimensions are 3.6 x 1.2 m^2. 1 – first diffraction grating, 2 – second diffraction grating, 3 – end mirror, which folds the beam back through the compressor under a slightly different angle, resulting in 2 distinct laser spots on both gratings where the laser beam hits both gratings, 4 – SHG crystal, 5 – dichroic mirror separating 515 nm from residual 1030 nm.

[7]The 515 nm beam transport, the last 3 OPCPA stages, the final chirped mirror compressor and the injector chamber housing the final mirror sending the broadband fs pulses down to experimental hall are also placed in vacuum.

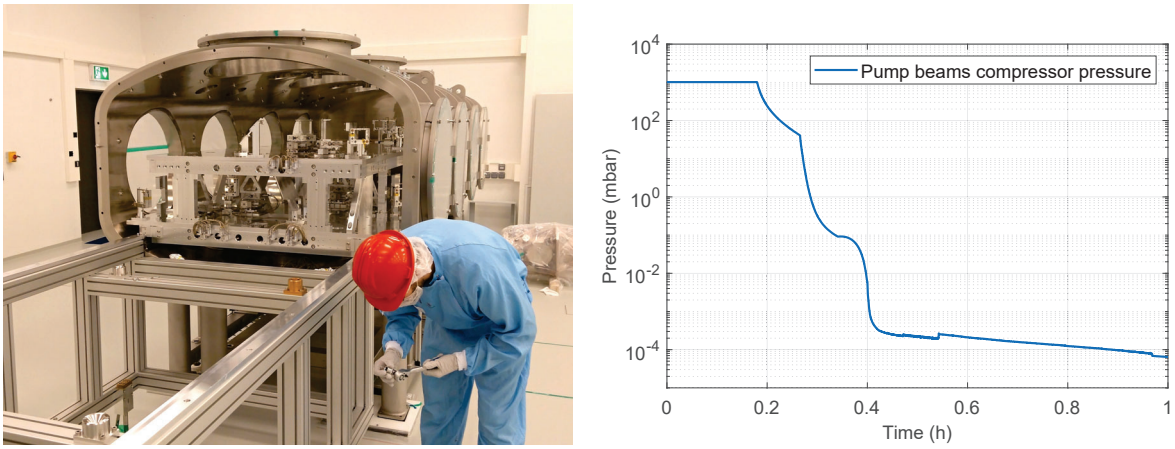

Fig. 29. Compressor photo and pressure. (a) – photo of the open compressor chamber during installation. The optical components can be accessed from 4 large doors on each side of the chamber. For larger maintenance tasks, the whole bench can slide out on rails when the front part of the chamber is removed. (b) – Pressure in the compressor during pumping. It takes 16 h to reach pressure of $2 \cdot 10^{-6}$ mbar.

The pump beam compressor chamber dimensions are about 3.8 x 1.9 x 1.4 m^3 and it takes about an hour to reduce the pressure in the chamber below 10^{-4} mbar (see Fig. 29), which is safe for full power operation. All vacuum chambers in the system are evacuated using turbomolecular pumps with dry screw vacuum pumps for pre-vacuum. Flanges and doors are sealed using unbaked Viton o-rings.

The leakage of compressed pulses through one of the 1030 nm mirrors inside the compressor is used for diagnostics. The leaked diagnostic beam is split and is incident on a camera where it is used for beam pointing stabilization. The other part is used to measure the pulse duration either by an in-house built autocorellator or an SHG-FROG (Picosecond FROG – PS10 from Femtoeasy). The dispersion tunability is an important factor of a CPA system. Here, it is achieved by temperature tuning of the CFBG stretcher or by limited movement of motorized folding mirror between the gratings. The mirror is capable of changing the compressor length by a total of 40 mm (that is 3 ps^2 of GDD change, compared to the tunability range of 64 ps^2 in the upgraded stretcher module).

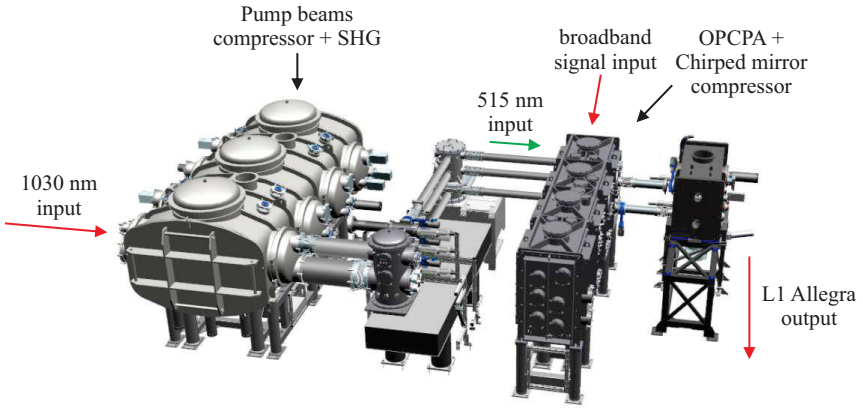

Fig. 30. 5 chambers of the L1 Allegra vacuum system. The broadband vacuum beam transport into the OPCPA chamber is not shown.

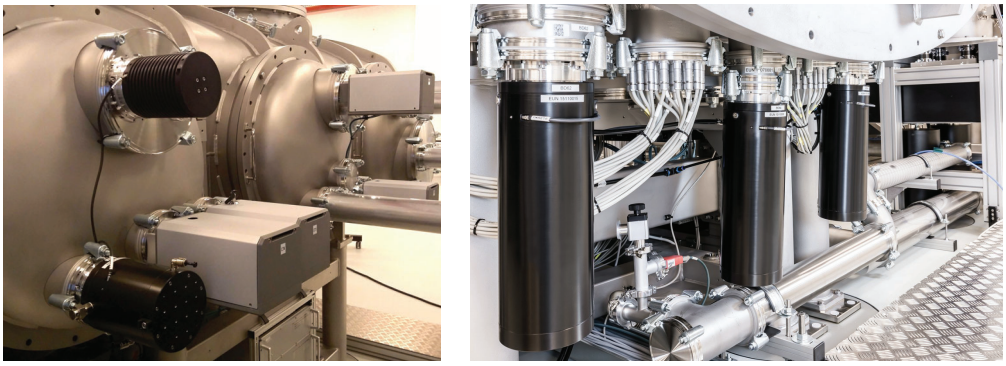

(a) (b)

Fig. 31. Beamdumps and camera boxes attached to the viewports of pump beams compressor chamber. (a) – photo of beamdumps for 0^{th} diffraction orders of compressor gratings and camera boxes, monitoring the LBO crystals and the gratings. (b) – water-cooled beamdumps for the residual beams at 1030 nm after SHG.

In order to be able to control the mirrors and gratings axis of rotation, most of the optical components within the chamber are motorized. The mechanical parts with motorized stages, optical benches and the chamber was manufactured in Delong company, Brno, based on ELI Beamlines design. Several inspection cameras designed to monitor the LBO crystals and diffraction gratings are placed in separate boxes and mounted on flanges on the side of the chamber (see Fig. 31a). We use water cooled beamdumps placed around the chamber in key positions to absorb the 0^{th} diffraction orders from compressor gratings and to absorb the residual 1030 nm beams after SHG (see Fig. 31b).

Compression and dispersion compensation

The shortest compressed pulse duration from the RA with a given output spectrum can only be reached with flat spectral phase spanning over the whole output spectrum. Any residual phase in the laser pulse will prevent us from reaching such duration. The main contribution to this extra phase can originate either from dispersion mismatch between the stretcher and compressor, present due to manufacturing tolerances of the CFBG stretcher, or as a consequence of self-phase modulation due to B – integral in the RA cavity.

The pump lasers were designed to generate pulses with energy of 120 mJ at 3 ps and 515 nm. Ideally, the CFBG stretcher should be able to compensate the dispersion necessary to reach FT limited pulse duration and then introduce only negative GDD to stretch the pulses to 3 ps (the advantage of negative stretching is described here [102]).

In theory, the 7 TEC elements placed underneath the original stretcher from Teraxion as part of the in-house built setup [97] should be able to change the amount of dispersion introduced by the stretcher (concept, first published in 2007 [103]). Unless the spectral phase is heavily modulated, this approach usually leads to good compression results. In our case, our TEC setup lacked the spatial resolution to fully optimize the compression and additionally we could only control the temperature and not the individual dispersion coefficients (although good results were still achievable with compressed pulses having more than 90% of energy in the main peak). That is why we bought an improved commercial solution with improved dispersion tuning capabilities in 2021. The comparison between the properties of the two stretchers is summarized in Table 6.

The advantage of the new module (Teraxion, TPSR-Xtended 1200ps) is the calibrated tuning of

Tab. 6. Properties of two CFBG stretchers. The original stretcher introduced an extra dispersion due to larger manufacturing tolerance. Values after symbol ± show the tunability of the calibrated dispersion coefficients of the new stretcher. Lower bandwidth of the new stretcher (2.5 nm FWHM) decreases the gain-narrowed RA output spectrum to 1.1 nm FWHM, which still supports 1.4 ps pulses.

Parameter	Original stretcher	New stretcher	Compressor	Units
Model	PSR	TPSR-Xtended 1200		
Year	2015	2021		
Fiber type	PMCMS	PMCMS		
Central wavelength, λ_c	1030	1030		[nm]
Bandwidth, $\Delta\lambda$	5	2.5		[nm]
Reflectivity, R	73	79		[%]
Measured GDD, $\varphi^{(2)}$	267	270 ± 64	269	[ps^2]
Measured TOD, $\varphi^{(3)}$	-5.32	-4.62 ± 196	-4.62	[ps^3]
Measured FOD, $\varphi^{(4)}$	0.89	0.13	0.13	[ps^4]

each dispersion coefficients ($D_2 - D_5$) separately, the disadvantage is the limited tuning range, corresponding to a smaller reflection bandwidth of 2.5 nm (compared to 3.5 nm of the original stretcher). The actual output spectrum from DIRA lasers is centered at 1030.7 nm (shown in Fig. 24a). Smaller tuning range and the fact that the new stretcher was specified for central wavelength at 1030 nm still prevents us from optimizing the dispersion completely. The best achieved result is a Gaussian temporal profile with about 10% of the energy still distributed outside the main peak and is shown in Fig. 32b.

The fact that 4 nominally identical, but different pump lasers are sharing the same stretcher inside the seed distribution system (see Fig. 20 for details) made it impossible to find optimal stretcher setting for all RA at the same time. For example, after optimizing the RA pumping OPCPA stage 4[8] to 2.5 ps with all the energy contained within the main temporal peak, DIRA 1 output pulse has a prepulse with an amplitude of 30% that of the main pulse at -5.7 ps. That means DIRA 1 itself needs a different stretcher settings for best compression. The difference between the measured FROG traces with their retrieved temporal pulse profiles of DIRA 1 at those two settings are shown in Fig. 33.

On top of that, measured FROG traces of each DIRA with fixed stretcher settings being different (shown in Fig. 34) demonstrate that each of the RA must have slightly different parameters (either differently curved thin-disks, different PC crystal lengths or different cavity modes), causing the output compressed pulses to be different at the same nominal power. The pulse duration between the three, affected by GDD and evaluated from the central peak, might be different due to different grating distance of each compressor, so only the presence and intensity of prepulses or postpulses should be taken into account. It is clear from this investigation that all four pump lasers need their own tunable stretcher in order to reach the optimal compression. I discuss the necessary design changes of the seed distribution on page 83.

[8]This RA has smaller linear cavity with two laser heads and smaller gain than DIRA 1 with 2 x 50 mJ at the output.

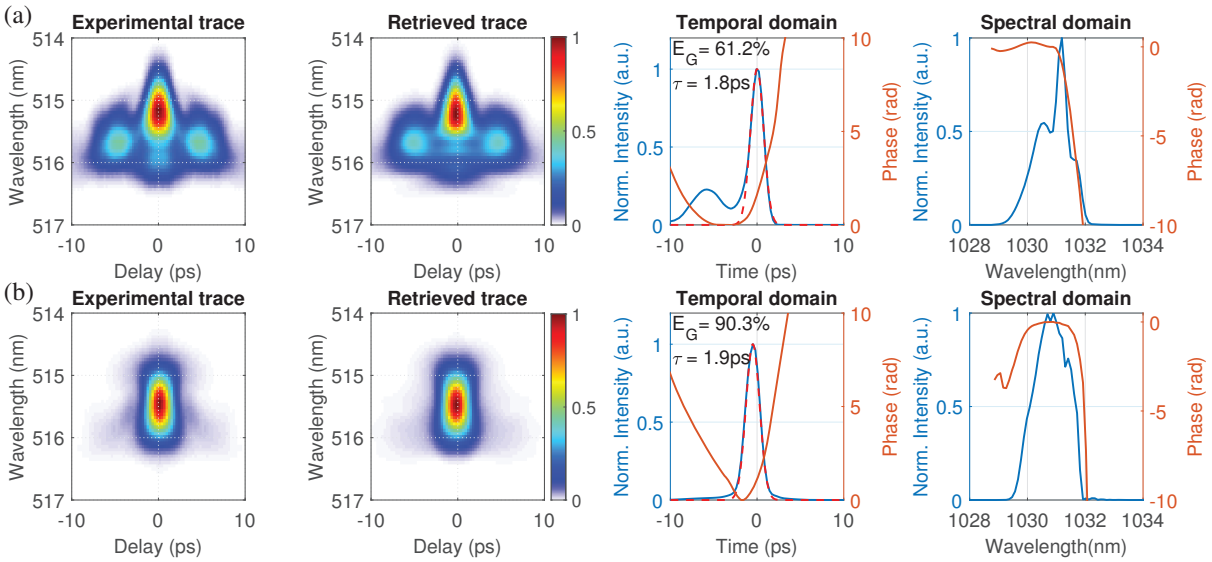

Fig. 32. New stretcher FROG results using DIRA 1, comparing the stretcher default settings (a) with optimized settings (b).

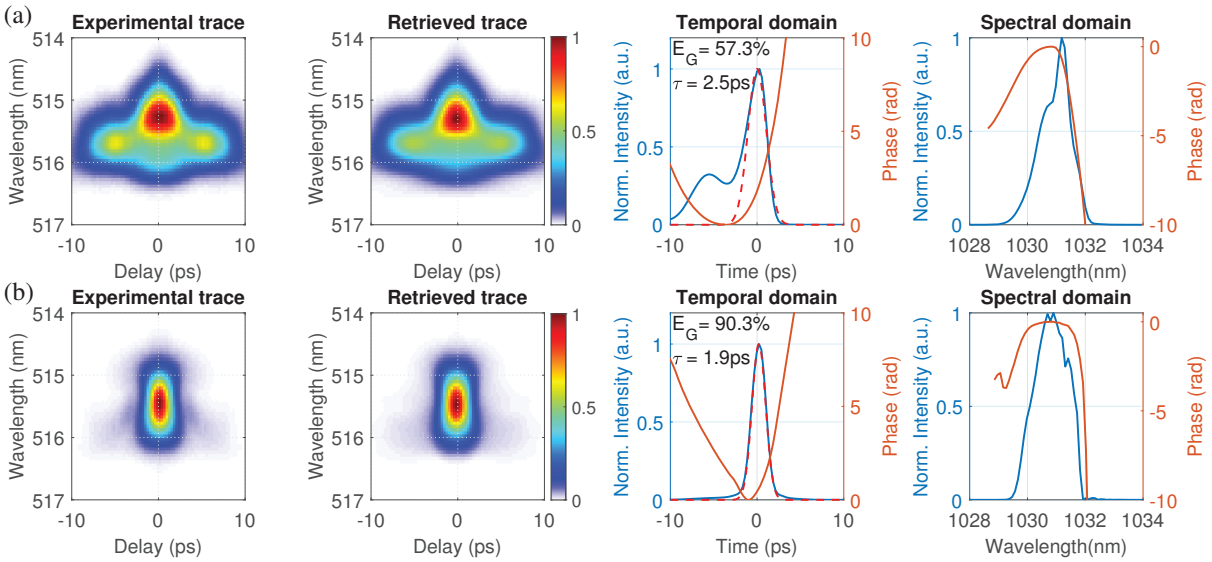

Fig. 33. Stretcher optimization for different pump lasers. E_G – laser pulse energy distributed within the main Gaussian peak, τ – retrieved pulse duration. (a) – FROG trace of DIRA 1 while the 2 x 50 mJ RA was optimized for 2.5 ps with nice FROG trace. (b) – optimized DIRA 1 FROG trace.

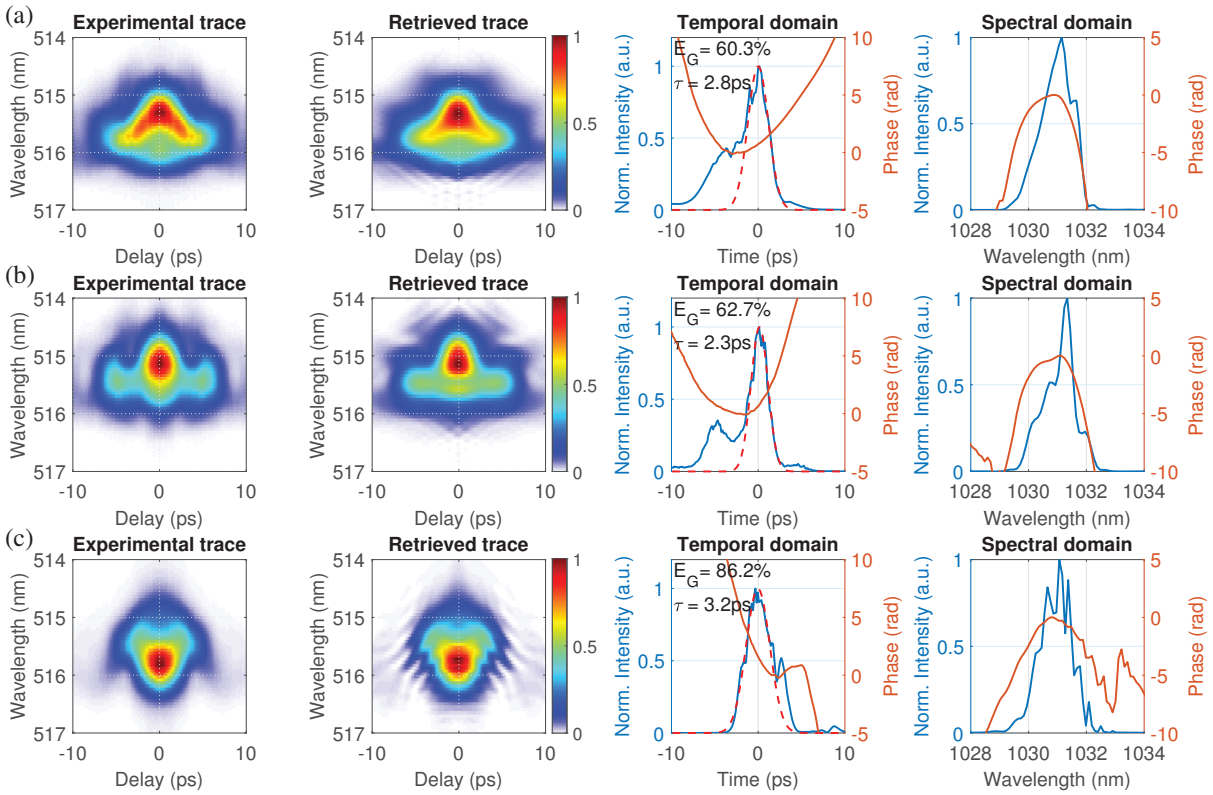

Fig. 34. Measured and reconstructed SHG-FROG traces with retrieved spectral and temporal intensity profiles and phases. Measured with fixed stretcher settings at 230 mJ output energy. E_G – laser pulse energy distributed within the main Gaussian peak, τ – retrieved pulse duration. (a) – DIRA 1, (b) – DIRA 2, (c) – DIRA 3. These FROG traces proves each RA needs custom stretcher settings in order to fully optimize the output pulse compression at 1030 nm.

4.4 Initial SHG results

The 515 nm pulses needed for pumping the OPCPA stages are generated through frequency conversion in LBO crystals and the SHG stages are placed in the same vacuum chamber as the three compressors. The SHG stages were designed to convert pulses with 3 ps duration, 200 mJ (assuming RA geneating 230 mJ and compressors with 87% efficiency) at beam diameter of 13 mm at $1/e^2$. The resulting intensity on LBO crystal was to be 100 GW / cm^2 and with reasonable 60% conversion efficiency, the energy at 515 nm was expected to be 120 mJ. This section describes the initial results with low SHG efficiency and how it is affected by the Ti:sapphire oscillator performance and by the rising temperature of the SHG stages in vacuum. It also shows pointing and pulse to pulse energy stability, and M^2 measurements at 515 nm.

We chose LBO crystals for SHG[9] due to their many favourable properties. Compared to crystals like YCOB, BBO or KTP, they have superior manufacturing quality, laser damage threshold as well as available aperture sizes[10]. They also have large angular acceptance bandwidth for type I phase-matching (1942 GHz cm), limited spatial walk-off angle (7.55 mrad) and reasonable effective coefficient describing the strength of the desired nonlinear process d_{eff} (0.83 pm/V [75]). With the crystal thicknesses we use, their lower temperature acceptance (7 K cm, which is five times less than BBO for example) is not an issue. The LBO crystals were manufactured by Cristal Lasers (France) and they were anti-reflection (AR) coated for 1030 nm as well as 515 nm on both surfaces. The default crystal dimensions were 33 x 33 x 1.7 mm^3. SHG process in *XY* plane of the crystal was chosen for type I SHG (ooe) and they were cut at angles $\theta = 90^\circ$ and $\phi = 13.6^\circ$, while the Z axis was perpendicular to the optical table.

The SHG stages, which hold the LBO crystals (see Fig. 35), are manufactured from aluminium and are designed as kinematic mounts with 2 axes, held together by a set of 6 springs. The horizontal axis of rotation (yaw) of the kinematic mount is controlled by a picomotor and allows remote angle tuning for phase-matching optimization. The vertical axis of rotation (pitch) can be optimized by a manual screw and has not been needed after the initial optimization. The LBO crystal is mounted between two indium foils to ensure good thermal and mechanical contact and placed in a round insert. Rectangular aluminium spacer and a spring loaded front part, secures the LBO crystal within the insert. Even

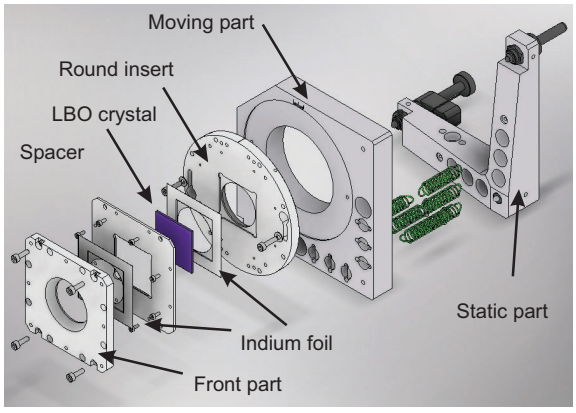

Fig. 35. SHG mount details. *Design by Petr Strkula.*

[9]They were also chosen for as crystals for the OPCPA stages pumped by the pump lasers described in this thesis.
[10]LIDT of 40 J/cm^2 at 10 ns and 1064 nm with aperture sizes of up to 100 x 100 mm are available these days according to [104].

though the design with the insert has the advantage of fast removal of the crystal from the chamber for inspections or replacement, the whole kinematic mount has the following disadvantages:

- **Low thermal contact** between the insert and moving part of the kinematic mount and between the moving and static part of the kinematic mount, limiting the possibility of establishing thermal equilibrium quickly during operation.
- **Large weight** of the moving part of the kinematic mount holding the crystal and the round insert, causing the mount get stuck sometimes as the picomotor is worn out by regular use.
- **Rotation without encoding** meant phase-matching optimization without any reference, always maximizing the output power.

4.4.1 Initial SHG results

With each pump laser requiring its own stretcher settings for optimal compression, the SHG results described in the following paragraphs were never measured at the same time and the laser used to generate those results is always specified either in the text or the figure caption.

Initial results using DIRA 1 compressed to 1.4 ps with 1.7 mm thick crystal generated only 85 mJ at 515 nm. The calculated SHG efficiency at that point was merely 43%. Additionally, this amount of energy was not stable over a longer period of time and was gradually decreasing, requiring frequent phase-matching corrections of the LBO crystal in horizontal axis (see Fig. 36a). Trying to match the measured data with simulation in SNLO software, several parameters can be assumed as a deviation from an ideal case (see Fig. 36b). Simulation assuming larger beam diameter, longer pulse duration, or suboptimal phase-matching (that is $\Delta k \neq 0$) influence the SHG curve differently and do not match the measured data. In this case, the reason for generating less than 120 mJ at 515 nm was the lack of energy in the main pulse for efficient frequency conversion.

In this work, I focused on finding out reasons for low SHG efficiency and on finding ways how to improve it.

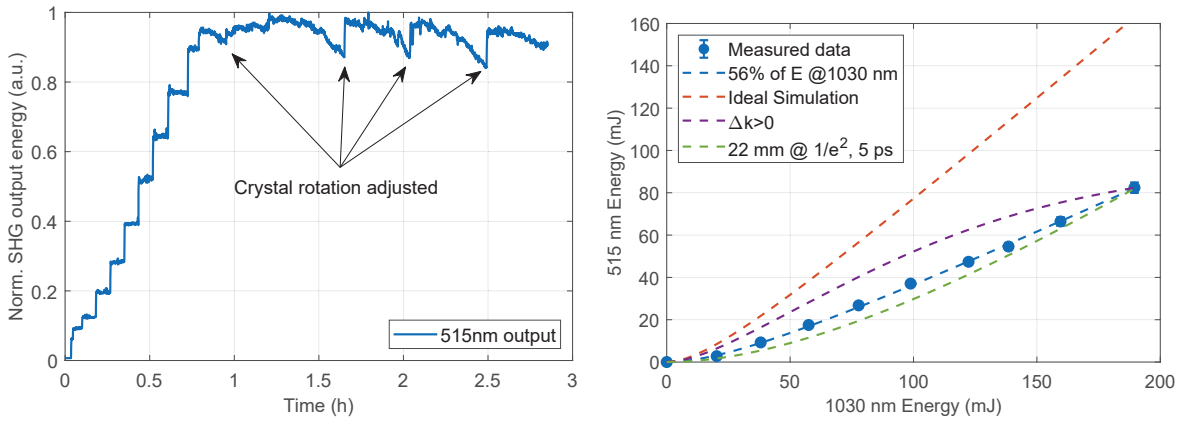

(a) (b)

Fig. 36. Initial SHG results and simulations with DIRA 1. Data measured with beam diameter of 15 mm @ $1/e^2$, 1.4 ps pulse duration, using LBO with thickness of 1.7 mm. E – energy, (a) – SHG output energy regularly decreasing, requiring phase-matching corrections by rotating the crystal. (b) – SHG data from the first 1 h ramp up in (a) compared with simulation using different parameters. When fixing all the parameters except the energy, the SNLO simulation matches the data well when 44% of energy is assumed to be distributed outside of the main Gaussian peak.

Different LBO crystal thickness and beam diameter

In order to improve the SHG efficiency as fast as possible and generate pulses with higher energy, we bought and installed LBO crystal with thickness of 2.2 mm. We also decreased the output beam diameter from the RA from about 15 mm at $1/e^2$ to 13.5 mm, by changing the magnifying telescope at the output. This allowed work on OPCPA stage 5 and running the L1 Allegra system for experiments while the work on further improving the SHG efficiency continued. Smaller beam diameter had also an impact on heating of the SHG mounts described in section 4.5.2. The resulting SHG efficiency with 2.2 mm thick crystal and 13.5 mm diameter at 1.4 ps was 50% and the generated energy was 100 mJ. The SHG efficiency with the two crystals is plotted in Fig. 37. In perfect case, a theoretical model in SNLO software predicts SHG conversion efficiency approaching 90%. This assumes perfect Gaussian spatial profile, perfect contrast, and all the energy contained within the main Gaussian temporal peak after compression.

Apart from the suboptimal dispersion compensation, causing the presence of pre/postpulses after compression, other factors influencing the SHG performance I found are described in sections that follow: pulse duration stability, temporal contrast of the 1030 nm pulses, rising temperature of the crystal mounts, non-ideal RA spatial beam profile and LIC in vacuum chambers. I also discuss the results of M^2 measurement at 515 nm and pulse to pulse energy stability.

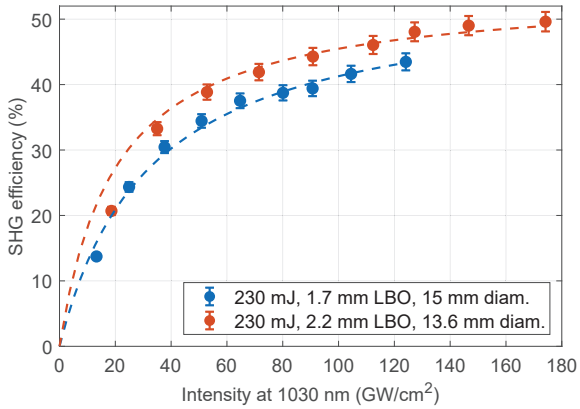

Fig. 37. Initial SHG result with DIRA 1 using different LBO crystal thickness (1.7 mm and 2.2 mm) and different output beam diameter (15 mm and 13.6 mm). Full points – measured data, dashed lines – SNLO simulation. The intensity on X axis was calculated from the measured average RA output power. It was changed by rotating the RA output waveplate. To match the measured data with simulation in SNLO using Gaussian spatial and temporal profile, I had to assume 45% of energy at 1030 nm is not available for efficient frequency conversion.

4.4.2 Importance of cavity energy stabilization

If the energy inside the cavity of the RA changes, different nonlinear phase acquired inside the cavity can affect the temporal pulse profile after compression and with it, the SHG efficiency. I already described in section 4.2 how this energy stabilization loop works. Fig. 38 shows the output energy at 515 nm for different RA cavity energy. The loop is not active at that point and the cavity energy is changed manually by more than 20 mJ by adjusting pump diodes output. In this particular case, the compressed temporal profile of the RA is better at 205 mJ. The output at 515 nm is later not changing, despite more energy available at 1030 nm. Different amount of higher order dispersion at higher

energies within the RA cavity causes the extra energy in the pulse after compression to be distributed outside of the main peak. To illustrate the situation further, Fig. 39 shows FROG measurement of the same RA running at 25 mJ and 230 mJ. By keeping the cavity energy stable with the pump stabilization feedback loop, the compressed temporal profile stays the same (for a given stretcher settings) and with it the intensity on the LBO crystal.

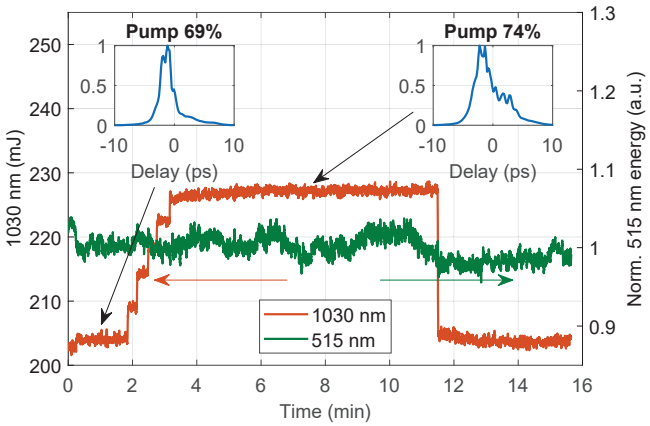

Fig. 38. DIRA 2 output energy at 1030 nm and 515 nm at different pump levels. Higher cavity energy is contributing differently to B-integral, adding extra phase, causing the temporal pulse profile after compression to be different. Worse compression result balances the higher energy available at 1030 nm and the 515 nm output stays the same.

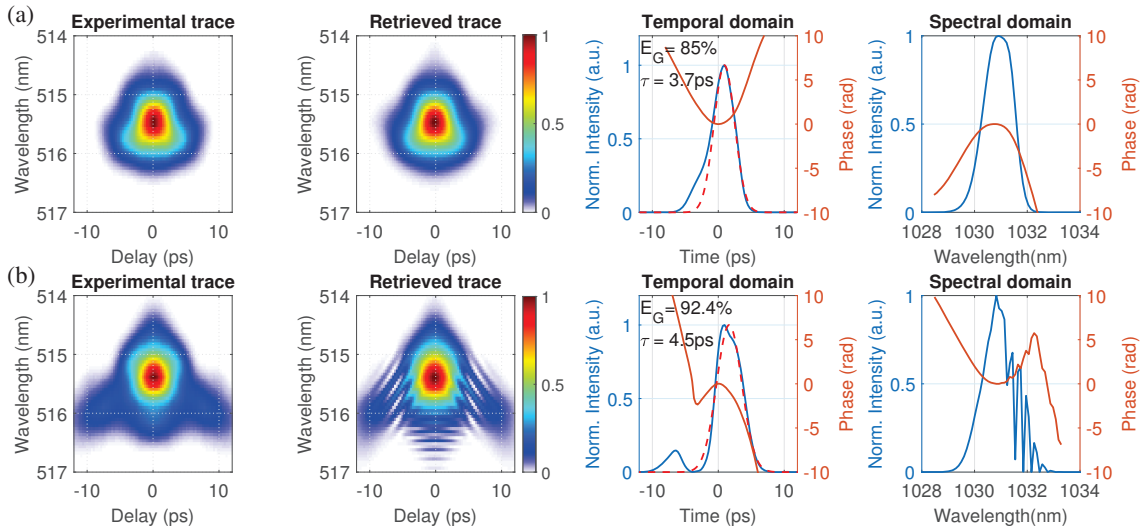

Fig. 39. DIRA 2 SHG-FROG traces at different cavity energies. Stretcher was not optimized at this point, hence the pulse duration around 4 ps. (a) – 25 mJ in the cavity, (b) – 230 mJ in the cavity.

4.4.3 Picosecond Contrast and Oscillator performance

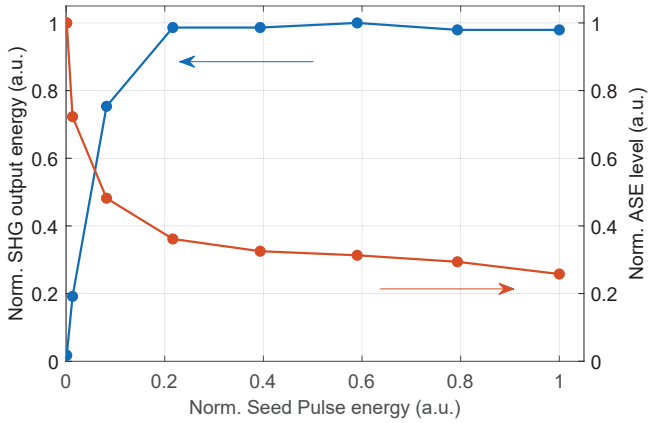

Fig. 40. SHG output energy dependence on the RA seed pulse energy. Measured data are suggesting the absolute seed pulse energy is not so crucial for the output SHG energy. *Data measured by Robert Boge*.

For the pump laser performance and the SHG efficiency, the amount of ASE in seed pulses is usually more crucial than the seed energy itself, to a certain point. By changing the gain of the last FA, the RA seed energy can be affected (the resulting build-up oscilloscope trace and RA output pulse profile were shown earlier in Fig. 27). This has little effect on the SHG efficiency though, as seen in Fig. 40. The SHG output energy stays about the same until the energy of seed pulses drops below a critical value. It is only at that point when the ASE contribution from the RA itself starts to play a significant role for the SHG efficiency.

The oscillator output energy at 1030 nm is much more critical. The SHG efficiency starts to drop as soon as the oscillator output starts to decrease, visible in Fig. 41a. The reason is the amount of ASE in the seed pulse as a consequence of low seed energy for the first FA in the seed distribution system. An important diagnostic tool to measure the amount of ASE present in compressed 1030 nm pulses is the third order autocorrelator (Tundra from Fast Innovations, with maximum delay range of 600 ps and detection limit of 10^{-8}). Contrast measurement of two different RA compressed pulses using this device is shown in Fig. 41b. It shows three sets of data - two from the DIRA 3 laser, measured at different Ti:sapphire performance, and one from a different pump laser providing 2 x 50 mJ pulses and using Yb:fiber modelocked oscillator instead of Ti:sapphire. While the SHG efficiency of DIRA 3 was between 45 – 55%, the other RA with better contrast had SHG efficiency of 73%.

The disadvantage of the third order autocorrelator is the energy requirement on the input pulses in picosecond regime (in this case about 500 mW). Since the maximum energy of the diagnostic leakage beams from the compressor is about 50 mW with RA output at full power, contrast measurements can only be done in air at low powers, with extra mirrors inserted into the beam path, sending the compressed beam out to the autocorrelator. Since the stretchers were optimized for vacuum conditions, the closest interval around the main peak of DIRA 3 data at 0 ps might be misleading, especially when compared with the different RA build and optimized in air.

Data plotted in Fig. 41 show that the Ti:sapphire oscillator performance can affect the contrast of the RA output pulses after compression. And that the SHG efficiency decreases, when the the performance of the oscillator drops. It also shows that a different RA using a seed distribution system based on Yb-modelocked oscillator can have much better contrast. I later show in section 4.5.5 how the same Yb-modelocked oscillator based front-end can be used to seed DIRA laser can benefit when using the same and how it improves the SHG efficiency.

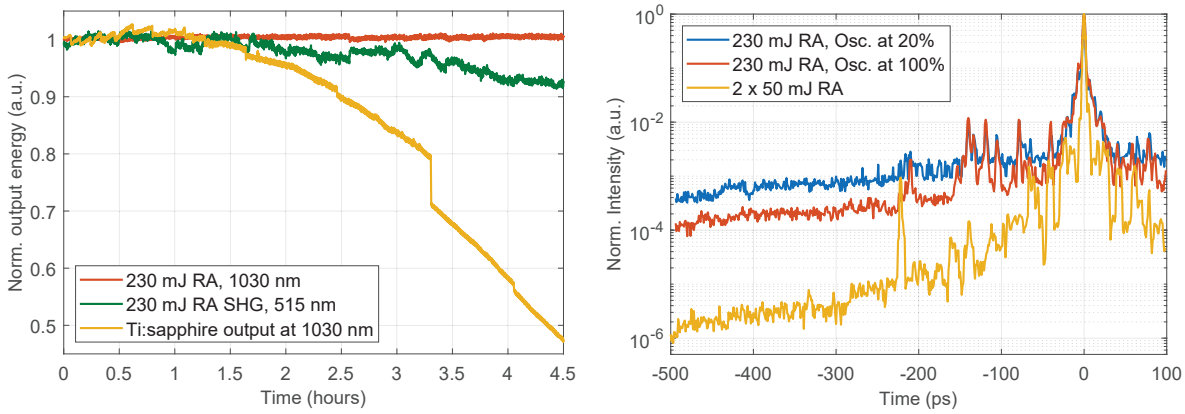

(a) (b)

Fig. 41. Oscillator performance, contrast and related SHG efficiency. (a) – Oscillator performance affecting the SHG efficiency. Even though the RA still generates the same output energy at 1030 nm, the SHG output drops due to lower energy from the Ti:sapphire oscillator available for the seed distribution. This also affects the 1030 nm contrast. (b) – Contrast measurement of 2 different RA, the 230 mJ one is DIRA 3. The 2 x 50 mJ RA is seeded by Yb-based oscillator and different seed distribution system. Detection limit of the device is 10^{-8}. SHG efficiency of the 50 mJ RA is 73%. The exact values of SHG efficiency of DIRA 3 (< 55%) were not measured at that point. This graph show one – Ti:sapphire oscillator performance affects the DIRA 3 contrast and two – a different RA using a different front-end have inherently much better contrast.

If using a different front-end would not be an option, there are other methods for improving the contrast of the RA, which would positively affect the SHG efficiency. One of them is the double chirped pulse amplification method (DCPA, published first in 2005 [105]). In this scheme, the partially amplified pulses (for example having energy of 2 mJ) are compressed, filtered with cross-polarized wave generation (XPW[11]), then stretched again, amplified further and compressed for the second time. Such IR pulses have better contrast (values better then 10^{11} were reported here [108]) and hence could be frequency converted with higher efficiency. This approach would require building a separate preamplifier and stretcher for each DIRA and would require significant financial resources.

4.4.4 Rising temperature of the SHG mounts

Frequency doubling of 1030 nm pulses at high energies and high average powers in vacuum might be influenced by absorption in nonlinear crystals. With bulk absorption being generally low (values mentioned by the LBO crystal manufacturers are below 2 ppm / cm [104]), it is usually the absorption in the antireflection crystal coatings that dominates for thin crystals. Our crystals were AR coated for both 515 nm and 1030 nm and the maximum measured absorption coefficients for both wavelengths realized on a 4 mm thick coated sample by a commercial company showed values of up to 50 ppm at 1030 nm and 100 ppm at 515 nm (see Fig. 42 for a typical graph of absorption measurement data, showing higher absorption in the coatings).

[11] XPW is a $\chi^{(3)}$-based nonlinear process, where a radiation with the same frequency but orthogonal polarization is created. As a third-order nonlinearity process, its efficiency for portions of the laser pulse with low intensity (ASE pedestals for example) suffers and the newly generated pulse have improved contrast. Separating the two pulses after XPW is done by polarization filtering. The disadvantage of this process is its overall low efficiency (10-15% for the XPW plus additional losses in the first compressor and second stretcher in DCPA scheme). As a consequence of XPW, the pulse duration and beam diameter are decreased by a factor of $\sqrt{3}$ [106]. It was first published in 2004 [107].

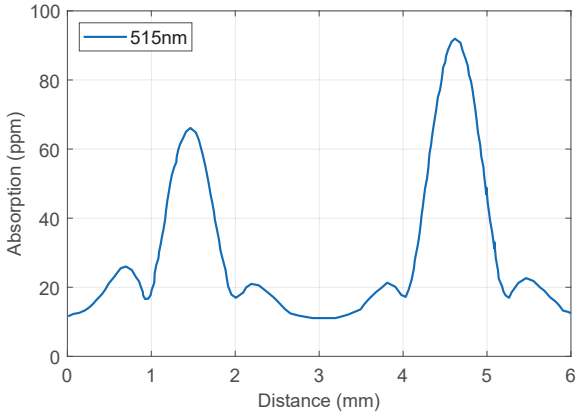

Fig. 42. Photothermal Common-Path Interferometry (PCI) Absorption Measurements of LBO at 515 nm (data measured by Coherent company). Absorption in the coatings is represented by value at the top of each peaks. Bulk absorption values are below noise threshold between the two peaks.

Let's assume the incident energy on the crystal at 1030 nm to be 200 mJ, SHG efficiency to be 50% and the absorption of the 515 nm beam only at the back surface coating of the crystal. In this case, the absorbed power in the LBO back coating will be 30 mW.

The limited thermal contact between the round insert (holding the LBO crystal, two indium foils, spacer and front rectangular part, see Fig. 43a) and the static part of the kinematic mount can be considered negligible for the following illustration. Due to vacuum environment and the lack of convective crystal face cooling provided by the surrounding air, this amount of absorbed energy should heat up all the parts of the insert by 0.56 °C every hour, causing the SHG output to slowly decrease by a few percent during several hours of operation. The actual measurement of the insert temperature in the chamber, holding the LBO crystal for DIRA 1, showed a temperature rise of 6 °C /h instead (Fig. 44a). Clearly, there was another source of heat, warming up the mount so much.

Such a temperature rise of the mount actually caused the SHG energy to change by more than 50% every hour. The mount temperature measurement (shown in Fig. 44a) can be used to simulate the effect on SHG output energy. This set of data was measured together with the SHG output energy showed in Fig. 44b. By using the temperature change of Δk calculated from $\mathrm{d}n/\mathrm{d}T$ (20), the simulated SHG output energy matches the measured data really well in Fig. 44b. This explained the need for frequent phase-matching corrections shown previously in Fig. 36a. In addition, the moving part of the kinematic mount was basically insulated from the static part of the mount and with it, from the rest of the optical table inside the chamber. The only few point contacts between the two parts of the kinematic mount, showed in Fig. 43b, did not allow any thermalization through conduction.

During my work on the pump lasers, I discovered this problematic temperature rise of the SHG mounts is caused by two issues. First of them was a thin carbon layer, deposited on the surfaces of the LBO crystals as a consequence of LIC in the vacuum chamber. This layer was causing extra absorption on the crystal and its process of creation and its mitigation are described in more detail in section 4.5.3. This investigation led to a paper published in Applied Optics journal [109]. Second of them was related to non Gaussian beam profiles from the first two RA, having portion of the energy contained in diameter larger than the clear aperture of the SHG mount. The mitigation of the rising SHG mount temperature is described in section 4.5.1. The parallel beam profile improvements are described in 4.5.2).

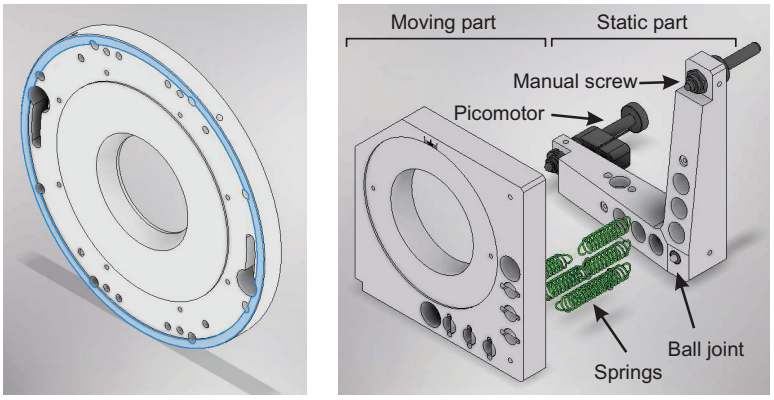

(a) (b)

Fig. 43. Parts of the SHG mount with poor thermal contact. (a) – the round insert, holding the LBO crystal, with milled out channel to allow all the screw threads to be vented. The surface area in contact with the rest of the kinematic mount is shaded blue. (b) – details of the contact between the moving and static part of the kinematic mount. The two parts are thermally connected mainly through 3 points (picomotor, manual screw and the ball joint). This effectively caused the moving part to be almost thermally insulated.

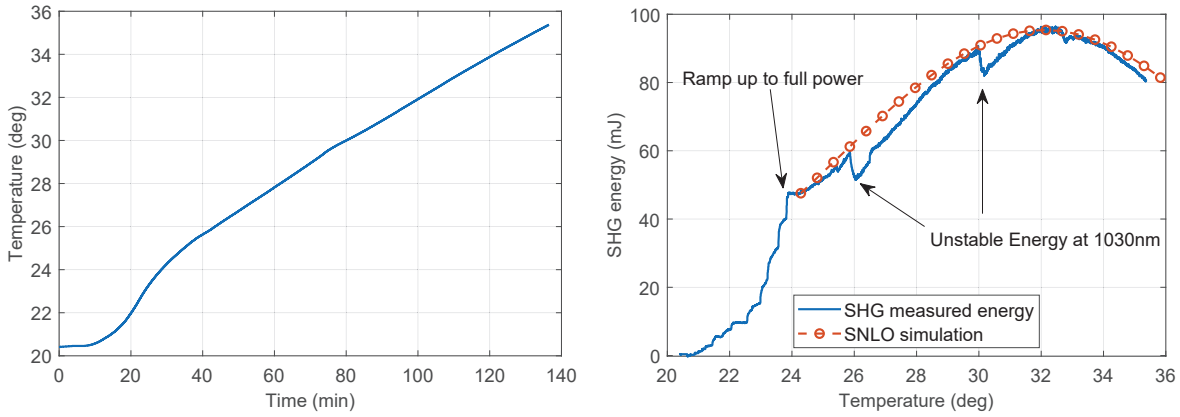

(a) (b)

Fig. 44. SHG performance using DIRA 1 and 2.2 mm LBO crystal. (a) – rising temperature of the front rectangular part of the SHG mount securing LBO crystal during the measurement, (b) – SHG output energy dependence on temperature during the same time. Phase-matching angle was optimized from the previous day for mount temperature of 32 °C and was not changed. Cavity energy stabilizing loop was not used in this case and the 1030 nm drops 3 times during the measurement. Red curve is simulated in SNLO assuming the maximum measured energy and phase-matching Δk changing as a consequence of refractive index change $\mathrm{d}n/\mathrm{d}T$.

4.4.5 Other SHG related results

Three small diagnostic setups are built for each of the pump lasers described in this thesis. They are placed in air and use leaked beams transmitted through vacuum windows. The position of the leaked beams used to measure the following pump laser parameters is shown in Fig. 45:

- compressor input and output beam profile, and input energy at 1030 nm
- output beam profile and energy at 515 nm
- pulse duration (with AC or FROG)
- pulse to pulse energy stability at 1030 nm as well as 515 nm
- M^2 at 1030 nm as well as 515 nm

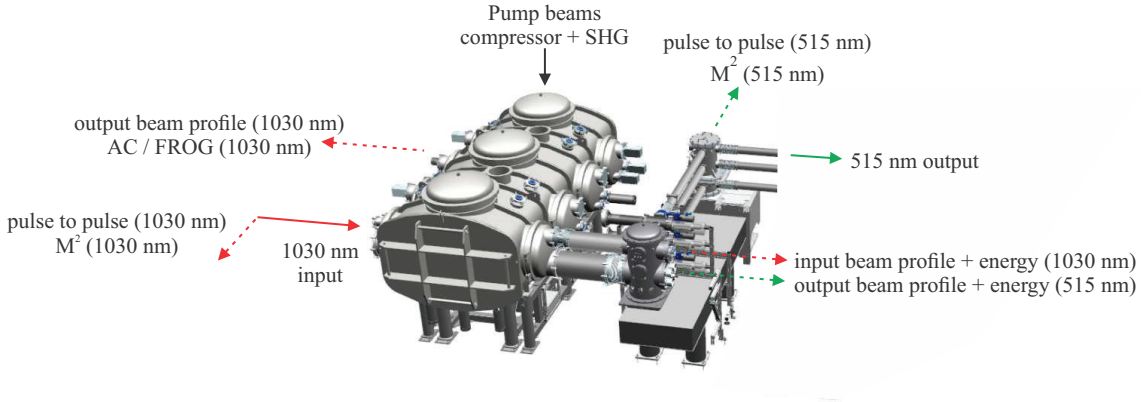

Fig. 45. Layout of the diagnostics for 1030 nm and 515 nm. Dashed lines – leaked beams for diagnostics, Full lines – input and output beam paths.

Beam quality measurement at 515 nm

M^2 measurement of the 515 nm beam from the SHG stage for DIRA 1 was carried out by using a remotely controlled translation stage[12]. This setup measured a beam leaking through one of the mirrors in the 515 nm beam transport and a nearby viewport with an uncoated vacuum window. Measurement was realized at two output energies at 515 nm – 10 mJ and 110 mJ. Data, showing M^2 values of 1.15 and 1.20 in X and Y axis at full power operation are plotted in Fig. 46a,b.

Before the above mentioned experiment, I also measured the M^2 of DIRA 3 at 515 nm, using the compressor and SHG stage for DIRA 1 [110]. This M^2 measurement was realized with older mirrors in the beam transport of DIRA 1 and the data are shown in Fig. 46c,d. They show the M^2 degrading from about 1.2 at low power to 1.9 and 1.6 in X and Y axis at full power operation. We currently see similar degradation of DIRA 2 M^2 as well. After replacing two mirrors in the DIRA 1 515 nm beam transport the M^2 measurement of DIRA 1 show no degradation (see Fig. 46a,b). That indicates an issue (with defects or small damaged spots for example) with some of the mirrors inside the beam transport for 515 nm pulses, rather than an issue with thermal deformation of optics inside the compressor or with thermal lensing inside the LBO crystals. Further investigation of the beam transport optics is necessary, as the degrading M^2 might be affecting the stability of optical cross-correlators synchronizing the pump and signal pulses.

[12] With a lens having a focal distance of 1000 mm, Newport FMS300CC Motorized Linear Stage and BeamGage camera BGP-GIGE-SP920G.

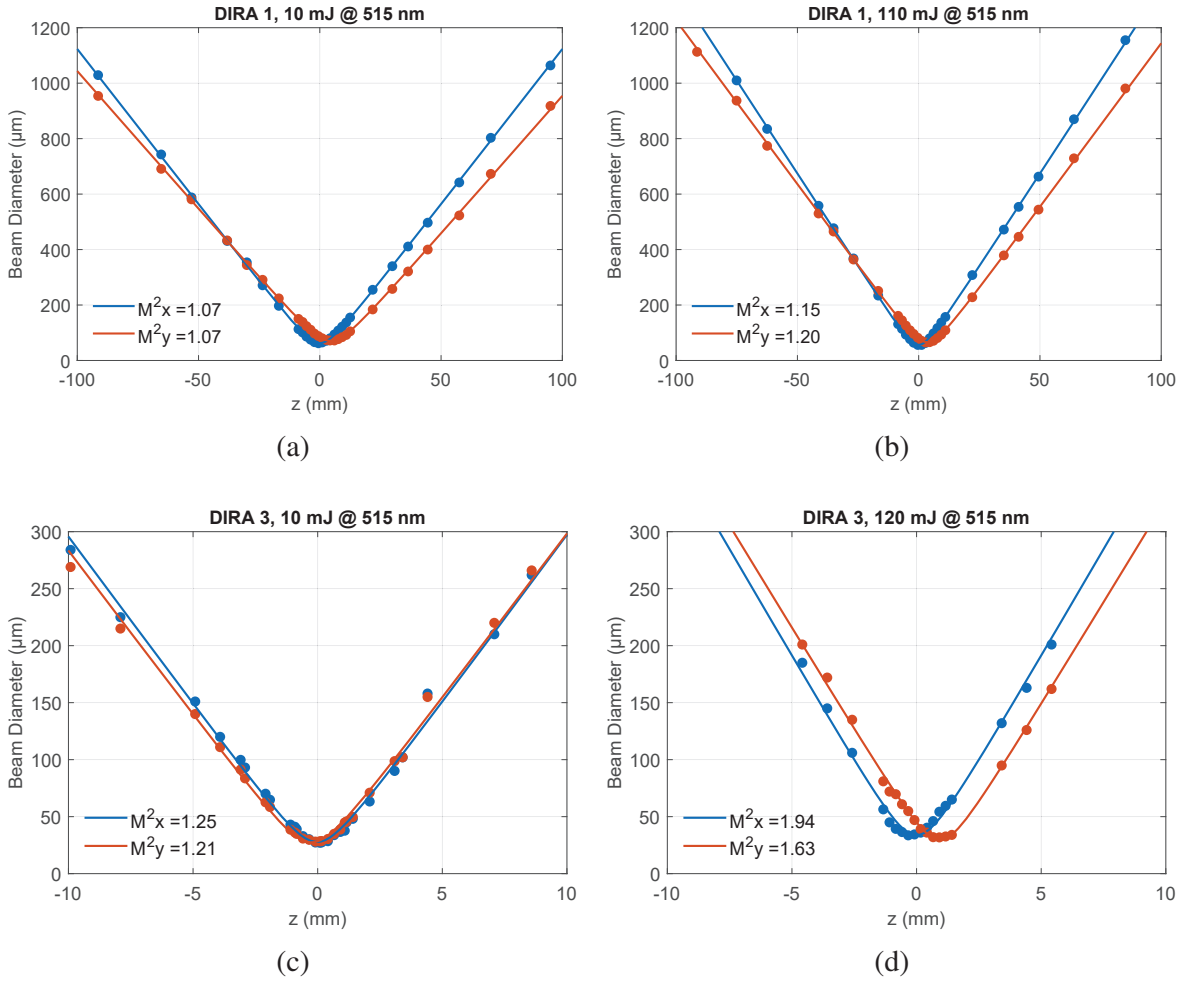

Fig. 46. M^2 measurement of DIRA 1 and DIRA 3 515 nm beam. (a) – SHG output with DIRA 1 at 10 mJ (low output power). The M^2 of X and Y axis is 1.25 and 1.21, respectively. (b) – SHG output with DIRA 1 at 120 mJ (maximum output power). The M^2 of X and Y axis is 1.9 and 1.6 respectively. (c) – SHG output with DIRA 3 at 10 mJ (low output power). The M^2 of X and Y axis is 1.1. (d) – SHG output with DIRA 3 at 110 mJ (maximum output power). The M^2 of X and Y axis is 1.2.

Pointing and pulse to pulse stability at 515 nm

The input and output beam profiles at 1030 nm are used for active beam pointing stabilization of the 1030 nm beam through the compressor. Active beam pointing stabilization ensures the standard deviation of the beam angular displacement is below 10 µrads in each axis (Fig. 47). The beam profiles of 1030 nm compressor input and 515 nm compressor output with their respective lineouts are in Fig. 48.

Measurement of the pulse to pulse energy stability of DIRA 1 at 1030 nm and 515 nm shows slightly larger standard deviation at 515 nm (2.2 mm crystal, 2 ps, 100 mJ at 515 nm) in Fig. 49. Decreased stability at 515 nm might be linked with lower SHG efficiency and might improve when higher output energies are reached in the future with improved compression and contrast.

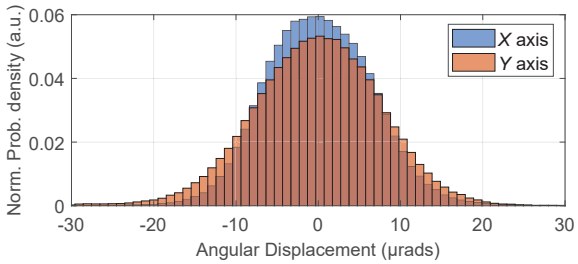

Fig. 47. Angular beam pointing stability, measured from the center beam axis during the 8 h of operation. Normalized probability density is plotted in *Y* axis. The standard deviation in *X* and *Y* axes is 6 and 7 µrads, respectively. The total area of each histogram is normalized to 1.

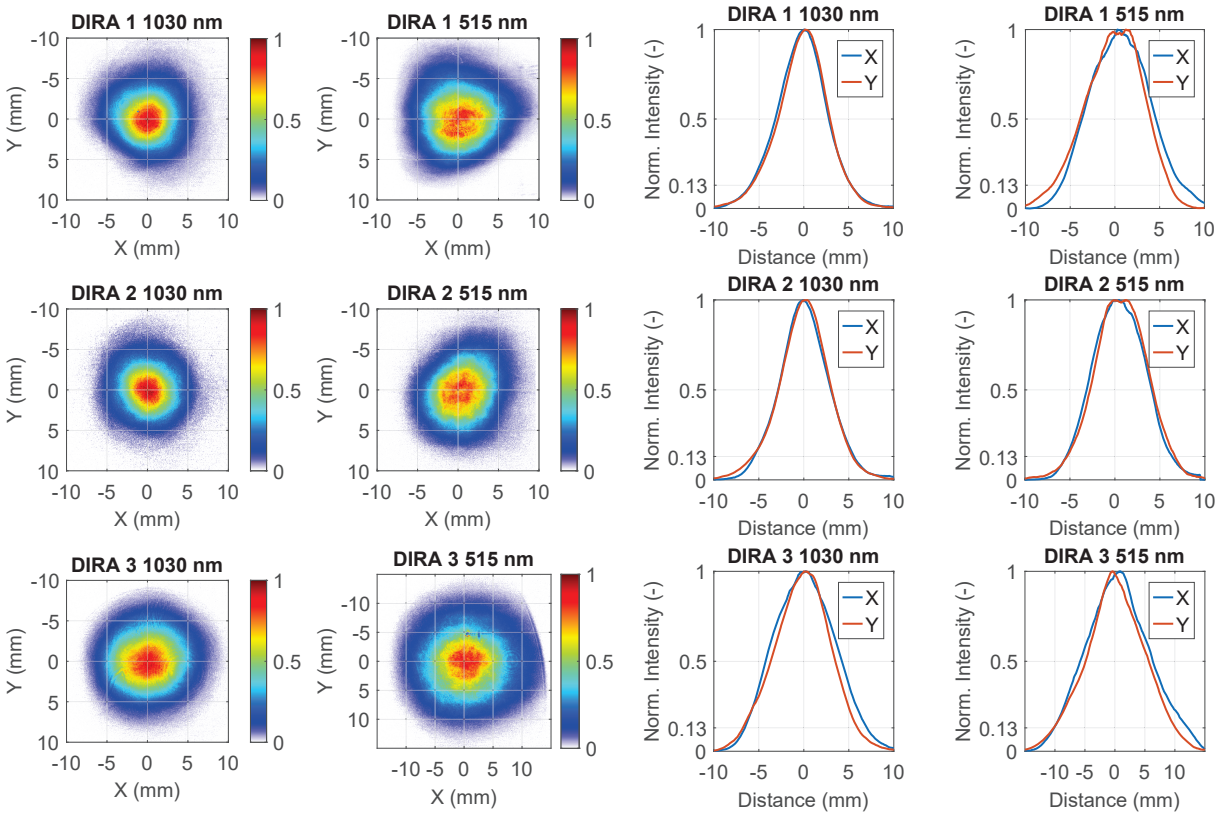

Fig. 48. Camera beam profiles of compressor input at 1030 nm and 515 nm output for each of the RA. Lineouts of the beam profiles show the *X* axis data in blue, *Y* axis data in red. It is important to mention that the beam profiles of the linear cavity DIRA 1 and DIRA 2 were recorded after I solved the issues with non-Gaussian beam profiles, described in section 4.5.2. The beam profiles of DIRA 3 were saved after installing a magnifying mirror with 50 m radius of curvature in order to prepare the beam path to OPCPA stage 7 for the future multipass upgrade. Hence the larger diameter at 515 nm for the third RA.

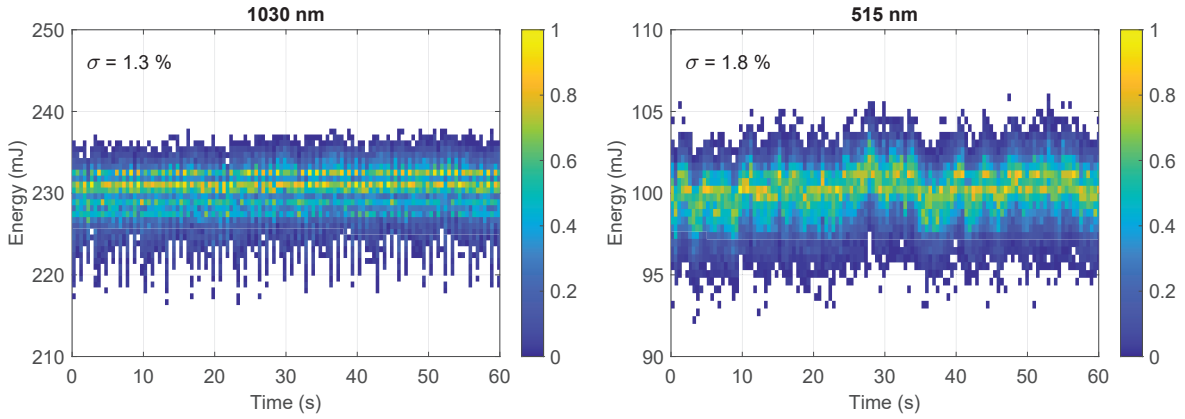

(a) (b)

Fig. 49. DIRA 1 pulse to pulse stability for both 1030 nm and 515 nm. Measured with 2.2 mm LBO crystal, pulse duration of 2 ps at 515 nm. The data were measured with 1 kHz repetition rate acquisition, the X – axis is averaged over 0.5 s. Slightly worse stability at 515 nm might be caused by the lack of energy in the main pulse and lower SHG efficiency (50%), not yet reaching saturated values. (a) – energy stability at 1030 nm, (b) – energy stability at 515 nm.

4.5 SHG drifts and efficiency improvements

This section addresses the issues with SHG performance, some of them already mentioned in section 4.4. It describes how the temperature of the SHG mounts was stabilized and how the SHG mounts were redesigned, how the two beam profiles from RAs with linear cavity were improved, how the problems with LIC were mitigated, and how a new front-end improves the pulse contrast at 1030 nm and with it, the SHG efficiency.

4.5.1 Temperature stabilization of SHG mounts

In order to mitigate heating of the LBO crystal mount described in Fig. 44, I first installed an aluminium mask in front of the SHG mount. This mask had the same clear aperture as the SHG holder and was meant to block most of the stray light otherwise hitting the mount and heating it up. a photo of the setup with the mask and two temperature sensors mounted on two places of the SHG holder is shown in Fig. 50a. Even with the extra mask, the temperature of the SHG mount was still rising[13], the situation did not improve, and the measured temperature data from the front part of the insert and the part of the kinematic mount holding it are in Fig. 50b.

In order to assess the best cooling options for the SHG stages, I modelled heating of the crystal mount[14]. The parameters of the model were optimized to match the data shown in Fig. 50b. In the simulation, I used laser beam with 15 mm diameter at $1/e^2$. I simplified the model by assuming only the absorption of the laser beam at 1030 nm in the front face of the LBO crystal and absorption coefficient was used as a free parameter (with thin crystal, the absorption of 1030 nm and 515 nm in the crystal's back surface could be simulated by larger absorption coefficient for the front surface). The simulation covered a time-period lasting 1 h, no convective cooling was used (to simulate vac-

[13] It was at this point I realized there must be another process responsible for the extra absorption. It eventually lead me to to discovery of the problems related to LIC.

[14] Simulation was done in Ansys [111].

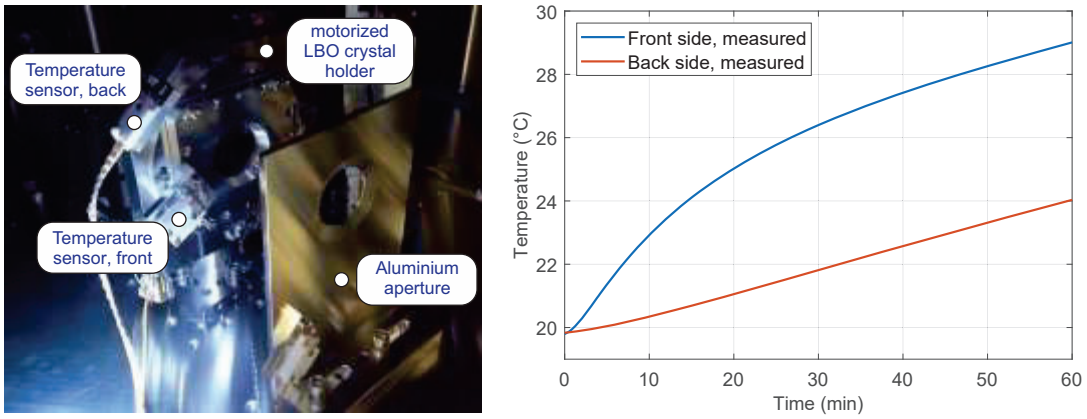

(a) (b)

Fig. 50. Rising temperature of the SHG mount. (a) – Setup with aluminium aperture, blocking portion of the beam otherwise hitting and heating up the SHG mount. Temperature sensors used for gathering the data highlighted. (b) – data measured by the two temperature sensor on the SHG mount.

uum conditions) and heat radiation effects were neglected[15]. The material properties of aluminium, indium and LBO were considered constant and isotropic and are listed in Tab. 7. The thermal contacts between the front aluminium part, the LBO crystal, two pieces of indium foil surrounding the crystal, and the round insert, which holds them, were considered perfect. The bottom surface of the round insert contact with the rest of the mount was limited (as explained in Fig. 43a) and the thermal resistance was used as a free parameter.

The thermal contact between the static and moving parts of the kinematic mount in the model was realized only through 3 points (two screw tips and one ball joint in the corner, following Fig. 43b) and heat transfer by the springs was neglected. The only boundary condition in this model was the temperature at the bottom of the static part of the kinematic mount, where it was secured to the optical table through a small optical post. It was set to match the measured temperature of the table near the mount, which rose from 19.8 °C to 21 °C within 1 h of operation used to gather the data in Fig. 50b. The absorbed power from the beam and the thermal resistance between the round insert and the moving part of the mount was optimized so that the resulting temperature in the model agreed with the real measured values. The best agreement between the simulated model and the real measured values was found with absorbed power of 1.4 W and thermal resistance of 50 W / m^2. Compared to the expected absorbed power of 0.03 W calculated from the measured absorption in the coatings (50 ppm at 1030 nm and 100 pm at 515 nm mentioned in section 4.4.4), this higher value was caused by the

Tab. 7. Thermal properties of the SHG mount materials used in the simulation. Source: [112]–[115]

	LBO	Aluminium alloy 5083	copper	indium	
thermal conductivity, κ	3.5	117	390	84	[W m^{-1} K^{-1}]
specific heat capacity, c_p	0.875	0.9	0.39	0.24	[kJ kg^{-1} K^{-1}]
density, ρ	2.47	2.66	8.94	7.31	[g cm^{-3}]

[15] Stefan–Boltzmann law describes the radiated power P from a given surface area A_S with a given emissivity ε, and ambient temperature T_0 to the surface temperature T difference as $P = A_S \sigma_B \varepsilon (T^4 - T_0^4)$. σ_B is the Stefan-Boltzmann constant of proportionality. The radiated power of the model is less than 1% of the assumed heat load causing the temperature rise of the SHG stage.

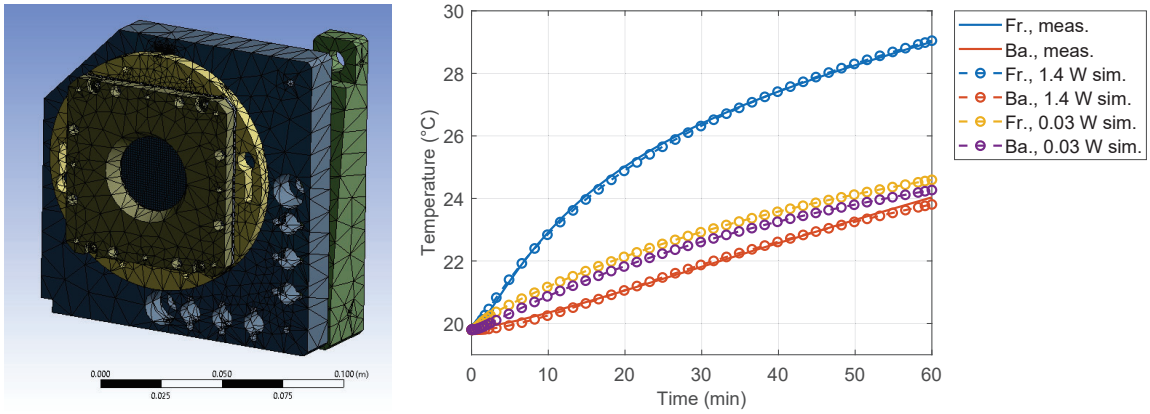

(a) (b)

Fig. 51. Simulation of the SHG mount heated by an absorption in the LBO crystal. (a) – meshed model of the SHG mount in Ansys, (b) – simulated data matching the measurement. The absorbed power and the thermal resistance between the round insert and the rest of the mount were used as free parameters and the best agreement was found with values of 1.4 W and 50 W / m^2 (blue and red). Simulation assuming fixed absorption of 0.03 W instead and perfect thermal contact between the insert and the rest of the moving part of the mount is shown as well (yellow and purple). Fr. – temperature at the front side of the mount, Ba. – temperature at the back side of the mount, meas. – measured, sim. – simulated.

LIC layer on the crystal and the simplifying assumptions of the model. Mitigation of the LIC and its effect on the temperature of the SHG mount is described in section 4.5.3. The resulting comparison between the measured data and simulation are in Fig. 51b.

I considered several solutions to improve the thermal contact between the insert with the crystal and the rest of the mount or with the optical table. The goal was to decrease the slope of the temperature rise and to speed up the thermalization of the mount. I modelled two of the most promising solutions (0.5 mm copper plate on the side of the mount and 4 flexible copper straps on the front part of the mount). Both still allow the rotation of the mount, do not require complete redesign of the stage and could be easily implemented. When the thin copper plate was added to the model, a perfect thermal contact with both sides of the kinematic mount was assumed, other boundary conditions stayed the same. When the 4 copper straps were added to the model, the temperature of their end facets was fixed to the same boundary condition present already at the bottom of the optical post (assuming these straps would later be secured to a metal heatsink, placed in front of the mount and attached to the table). The results, showing the advantage of the straps solution are evident from Fig. 52.

The copper straps solution feasibility was tested by mounting a single copper braid designed for high current transmission in electric industry to the front of the SHG mount (Fig. 53a). Copper, with its high thermal conductivity and vacuum compatibility is a good material for transferring heat in vacuum environment [116]. Since the front part of the mount secures the LBO crystal in place by pushing on it through 4 screws with springs, the copper braid mounted at the bottom created a lever tilting the front rectangular part. In order to avoid damage to the LBO crystal, the crystal was removed from the mount. The laser beam from DIRA 1 was used for this test and the aluminum aperture, otherwise blocking portion of the scattered light, was removed. Fig. 53b shows how the installation of the braid improved the thermal situation.

After the successful test with the copper braid, proving the thermalization can be sped up by removing the heat from the front part of the mount, the strap solution design was further modified. In order to avoid damage to the crystal, the placement of the copper straps was shifted from the front part to

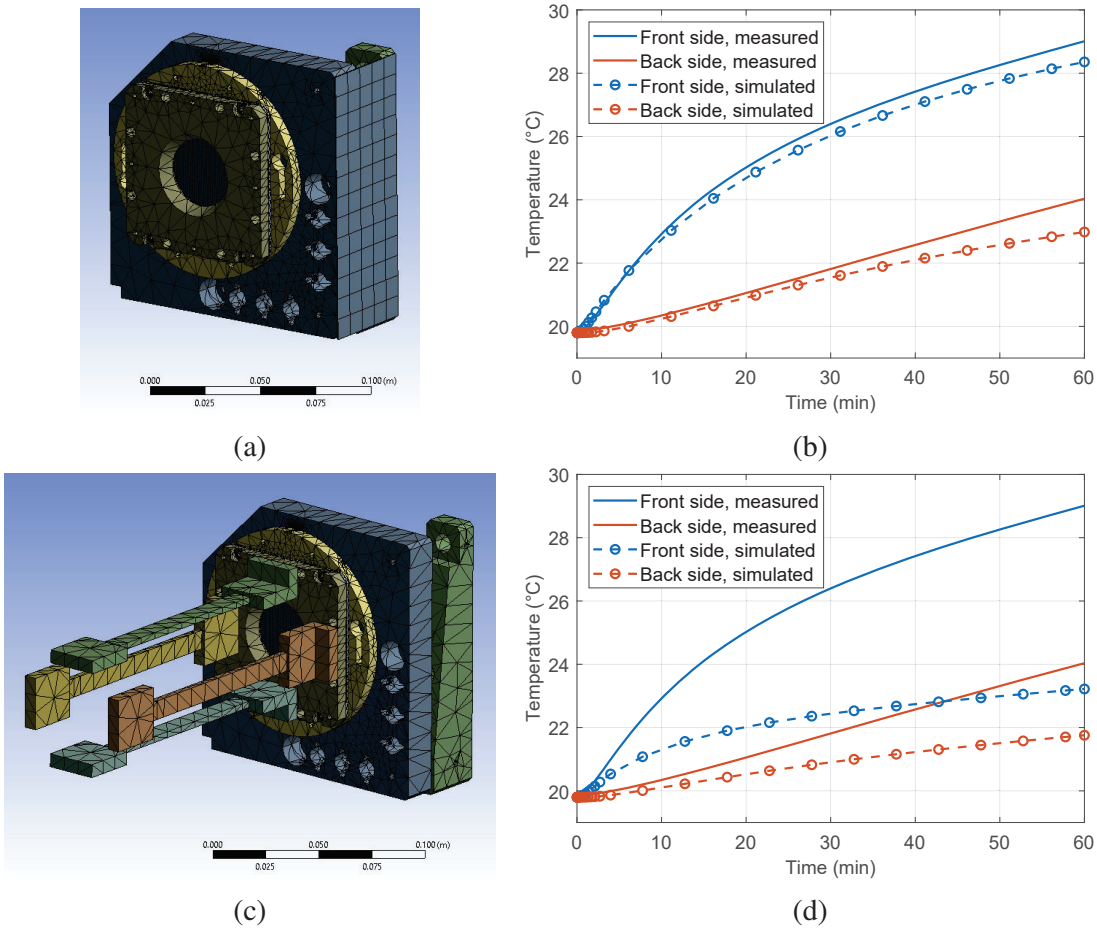

Fig. 52. Simulation results of the SHG mount heated by an absorption in the LBO crystal with two improvements considered. The original measured temperature is plotted as well for reference. Absorbed power of 1.4 W and insert thermal resistance of 50 W / m^2 is still assumed. (a,b) – 0.5 mm copper plate mounted on the side to increase the thermal contact between the two parts of the kinematic mount. The effect on the temperature of the mount is minimal. (c,d) – 4 copper straps mounted on the front with the same temperature boundary condition at the end of the straps as on the bottom of the mount. Copper straps significantly reduces the heating of the mount.

the circular insert to avoid any levers acting on the crystal through the front part of the mount. Also to allow reaching thermal equilibrium faster and avoid crystal temperature changes whenever the output of the RA is changed, 3 vacuum compatible TEC elements (Thorlabs, TECD2) were included in the new design as well. Due to the limited space in the chamber around the mount and the diagnostic beam propagating close to it, the TECs could only be mounted on one side of the SHG stage. a new aluminium U-shaped piece secured to the round insert was used to enable mounting of the TECs on the insert. The copper straps were used as a heatsink for the hot side of the TECs and were mounted on top of them. The other ends of the copper straps were secured to the aluminium heatsink, connected to the optical table and providing a thermal contact. The layout and photos of the setup are in Fig. 54.

The TECs were powered and controlled by a commercial temperature controller placed outside the vacuum chamber and built by Martin Horáček. The temperature controller was powered by laboratory DC power supply with current limited to 2.4 A to prevent overheating of the three TECs connected in

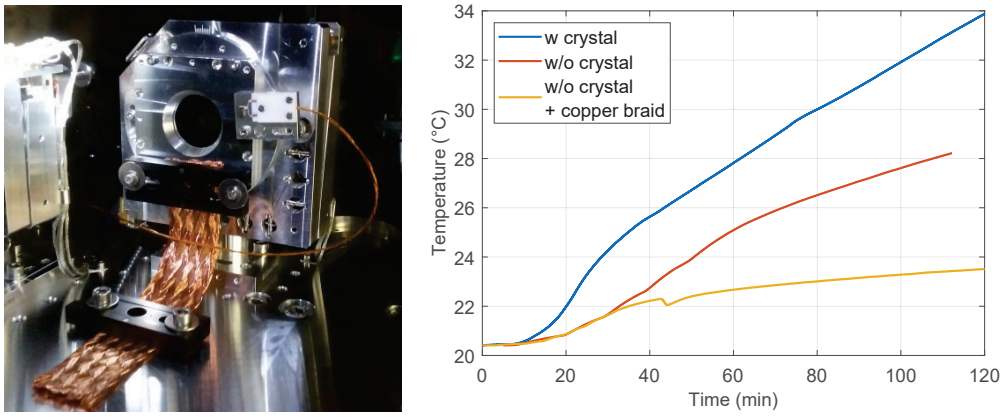

(a) (b)

Fig. 53. First test of improved heat transfer with copper braid secured to the front of the SHG mount. (a) – The SHG stage without the crystal with copper braid and a temperature probe secured to the front rectangular part, (b) – comparison of temperature measurement for three separate cases - the initial case of the mount with crystal inside without any copper braid attached (blue), the empty mount without crystal without any copper braid attached (red) and the empty mount without crystal with copper braid attached (yellow). The measurements without the crystal show how much the mount heats up due to the scattered light hitting the mount.

parallel due to the limited passive cooling capacity of the copper straps. The feedback for the PID loop controlling the TECs was provided by a little thermistor placed right underneath the TECs to avoid PID loop delays. The disadvantages of this design were later addressed by designing an improved air cooling setup described in section 4.5.4.

The described thermal stabilization solution with the TECs was capable of maintaining stable temperature of the LBO crystal holder for DIRA 1 and DIRA 2 throughout the day. It allowed the pump lasers with linear cavity design to generate stable SHG output, which was frequently used to pump the OPCPA stages 5 and 6 during experimental campaigns. No phase-matching angle correction were needed. The graph of the DIRA 1 SHG mount temperature and the SHG output during a typical day of L1 Allegra system operation is shown in Fig. 55.

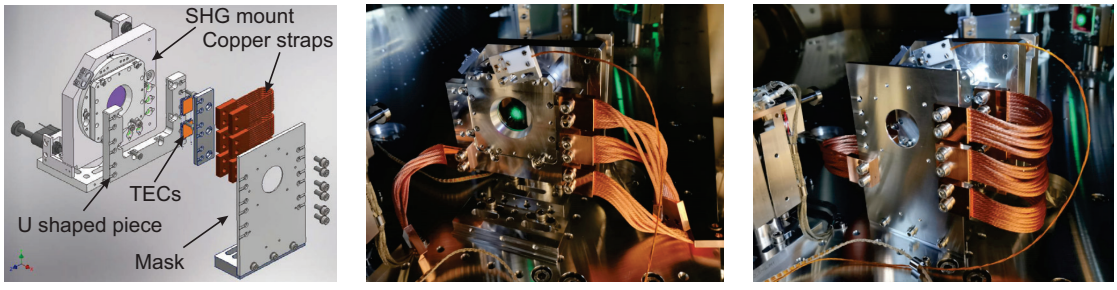

(a) (b) (c)

Fig. 54. The solution to allow the LBO crystal in the SHG mount to reach thermal equilibrium, allowing several hours of adjustment free operation. (a) – 3D model, (b) – kinematic mount with the crystal and copper straps (front mask removed for visibility). TEC elements stabilizing the mount are placed under the copper straps on the right side. (c) – the same setup with the aluminium mask in front. a combination of the connected straps, mask and optical table acts as a heat-sink for the TECs. The extra strap mounted on the left side was eventually removed before full operation. *Design by Petr Strkula.*

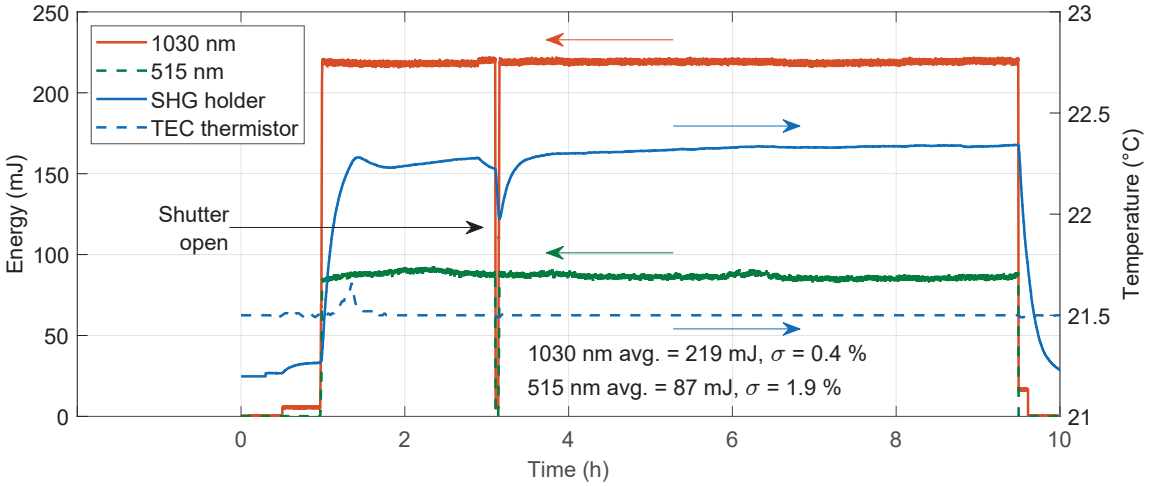

Fig. 55. Typical values of DIRA 1 output energy and SHG mount temperature during the L1 Allegra system operation with TEC stabilization on. Temperature monitored by the thermistor (blue dashed line) close to the TECs was set to 21.5 °C, the second temperature sensor mounted in the top of the moving part of the kinematic mount measured slightly higher values (blue full line). The 1030 nm (orange) and 515 nm (green) energy were measured by PDs in the diagnostic section of the compressor chamber. After an hour of running the laser, the 1030 nm output power was minimized briefly to allow the shutter to be opened and the 515 nm beam (green) was sent to the OPCPA stage 5. The improvement of SHG output stability is visible especially when compared with data shown in Fig. 36a and Fig. 44b.

4.5.2 Beam profile improvement at 1030 nm

The rising temperature of the SHG mount without the crystal inside showed in Fig. 53 indicated the SHG mount was also heating up due to scattered light (when using the RA with linear cavity). a quick measurement was carried out to find out how much power is not transmitted through the clear aperture of the SHG mount by measuring the temperature of the aluminium mask, used in the TEC temperature stabilization setup in Fig. 54 without the copper straps connected. The mask had the same clear aperture of 31 mm as the SHG mount. It was mounted on a peek pedestal to thermally insulate it from the rest of the optical table[16].

At full output power from the RA with linear cavity, the temperature of the mask rises by 31.2 °C / h (Fig. 56). From the known mask dimensions and material, the amount of light not passing through the clear aperture of the mask was calculated to be 1.3 mJ (0.6% of the total 200 mJ after the compression). The $1/e^2$ diameter of the RA beam was 15 mm at that time and the aperture blocking the same 0.6% of the incident energy would normally have to be 24 mm in diameter instead of 31 mm. More careful analysis of the RA output beam profile after 20 m of propagation from the RA (the distance to the LBO crystal plane) showed 0.7% of the energy is distributed outside the clear aperture of the mask and the beam profile is not strictly Gaussian (comparison between the measured beam profile and an ideal Gaussian profile with the same diameter at $1/e^2$ is shown in Fig. 56b).

We decreased the output beam diameter from the two RA from about 15 mm at $1/e^2$ to 13.5 mm, by changing the magnifying telescope at the output. Smaller beam diameter would avoid clipping on the 31 mm clear aperture of the SHG mount and would increase the intensity on the crystal - compensating for the lack of energy in the main temporal peak after compression. Decreasing the beam diameter and using a longer LBO crystal led to an improvement of SHG efficiency showed earlier in Fig. 37.

[16] thermal conductivity of peek is 0.26 W m^{-1} K^{-1} so it provides reasonably good thermal insulation [117].

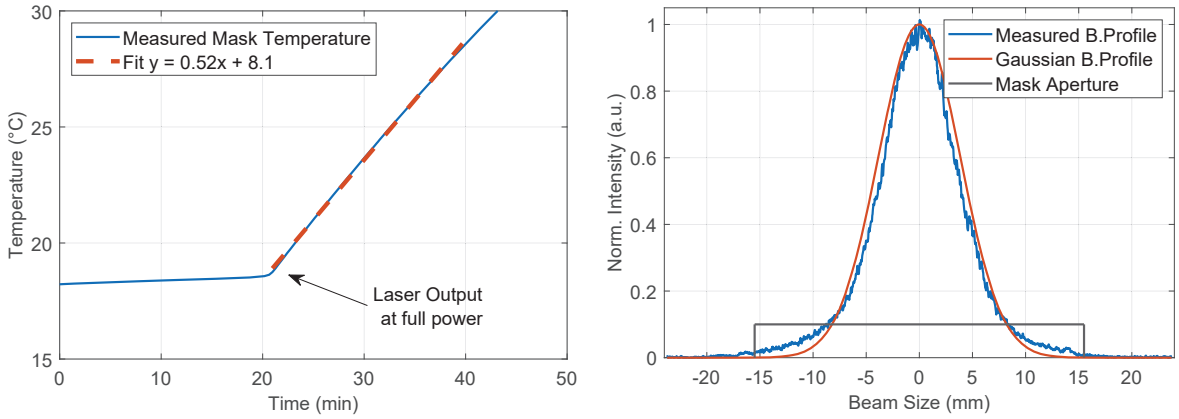

(a) (b)

Fig. 56. Two experimental results related to the SHG mount heating up due to scattered light. (a) – thermally insulated aluminium mask temperature rising due to portion of the energy being distributed outside of the clear aperture of 31 mm, fitted curve show the mask's temperature rise by 31.2 °C / h, (b) – X lineout of the beam profile with Gaussian fit and clear aperture of the mask depicted, calculated energy outside the clear aperture is 0.7% for the measured beam profile and 0.005% for the Gaussian fit.

The non-Gaussian beam profile at the LBO crystal plane can be explained by extra spatial phase added to the beam before propagation:

$$\Delta\phi(x) = 2\pi/\lambda\,\Delta n(x)\,L, \tag{28}$$

where x is the radial coordinate, λ is the laser pulse wavelength, Δn the refractive index change caused by a given process and L is the length of a material. Such a phase can be added either by transmission through medium with non-negligible nonlinear index of refraction (self-focusing), in which case $\Delta n = n_2 I(x)$, or by transmission through medium with thermal lens, in which case $\Delta n = (\mathrm{d}n/\mathrm{d}T)\Delta T(x)$. In both cases the simulated beam profile after 20 m of propagation from the RA (distance to the LBO crystal) has smaller FWHM diameter and higher portion of the energy distributed outside of the $1/e^2$ diameter, when compared to the strictly Gaussian profile with the same diameter. The problem with non-Gaussian beam profile at the LBO crystal plane is not present for the ring cavity DIRA 3. I concluded that the only material that could affect the beam profile this way is the

Fig. 57. Photo of the Faraday rotator.

Tab. 8. The properties of TGG and KTF crystals [118].

	TGG	KTF	
Formula	$Tb_3Ga_5O_{12}$	KTb_3F_{10}	[-]
Refractive index, n @ 1064 nm	1.944	~ 1.5	
Nonlinear refractive index, n_2	$\sim 20 \times 10^{-20}$	$\sim 1 \times 10^{-20}$	[m^2W^{-1}]
Thermo-optic coefficient, dn/dT	17.9×10^{-6}	$\sim 1 \times 10^{-6}$	[$m\,K^{-1}$]
Thermal conductivity, κ	7.4	1.67	[$W\,m^{-1}\,K^{-1}$]
Thermal expansion coefficient, α	7.3	13.7	[K^{-1}]

20 mm long crystal of Terbium Gallium Garnet (TGG) inside the Faraday rotator (its position within the linear cavity RA can be seen in Fig. 13 and the photo is shown in Fig. 57). This rotator is present only in the two RA with a linear cavity. Simulation of Gaussian beam profile propagation through the rotator, using some of the TGG crystal properties listed in Tab. 8 is shown in Fig. 58. In both cases (extra phase from thermal lensing or from self-focusing) the calculated beam profiles resemble the measured one from Fig. 56b. I later carried out an experiment concluding the effect responsible for the extra phase is related to thermal lensing only (description on page 67).

Apart from the TGG crystal, a Pottasium Terbium Fluoride (KTF) crystal can also be used inside the Faraday rotators and has only recently become available in large apertures. The KTF crystal has more favourable properties for Faraday rotators used in high average power and high energy lasers and the comparison of optical parameters of TGG and KTF crystals are in Tab. 8. Both nonlinear refractive index as well as the dn/dT coefficient of KTF are significantly smaller than those of TGG [119]. The manufacturing company of the original TGG rotators (Electro-optics technology, EOT), were able to provide us with, at that time commercially unavailable, custom solution of a Faraday rotator with KTF crystal inside. The custom made KTF rotator had the same clear aperture of 20 mm, which enabled quick and efficient replacement of the TGG rotator. After the replacement, the output beam profile of the RA with KTF rotator improved and became Gaussian. The output telescope of each RA was originally compensating the thermal lensing inside the rotator and the newly collimated RA output diameter after the KTF rotator installation changed from 13.5 mm at $1/e^2$ to about 13 mm. The measured beam profiles from RA with TGG and KTF rotators after 20 m of propagation are in Fig. 59.

Improvement of the RA output beamprofile in combination with the LIC mitigation described later (section 4.5.3) led to an improvement in the heating of the SHG mount. After this, the active stabilization with TECs was not needed anymore. The SHG output does not decrease by more than 1% during a day and does not require phase-matching corrections. The combination of a small decrease in beam diameter from 13.5 mm to 13 mm at $1/e^2$ and improving spatial intensity distribution due to installation of the KTF rotator improved the SHG efficiency of DIRA 1 stage from 50% to about 54% (see Fig. 60).

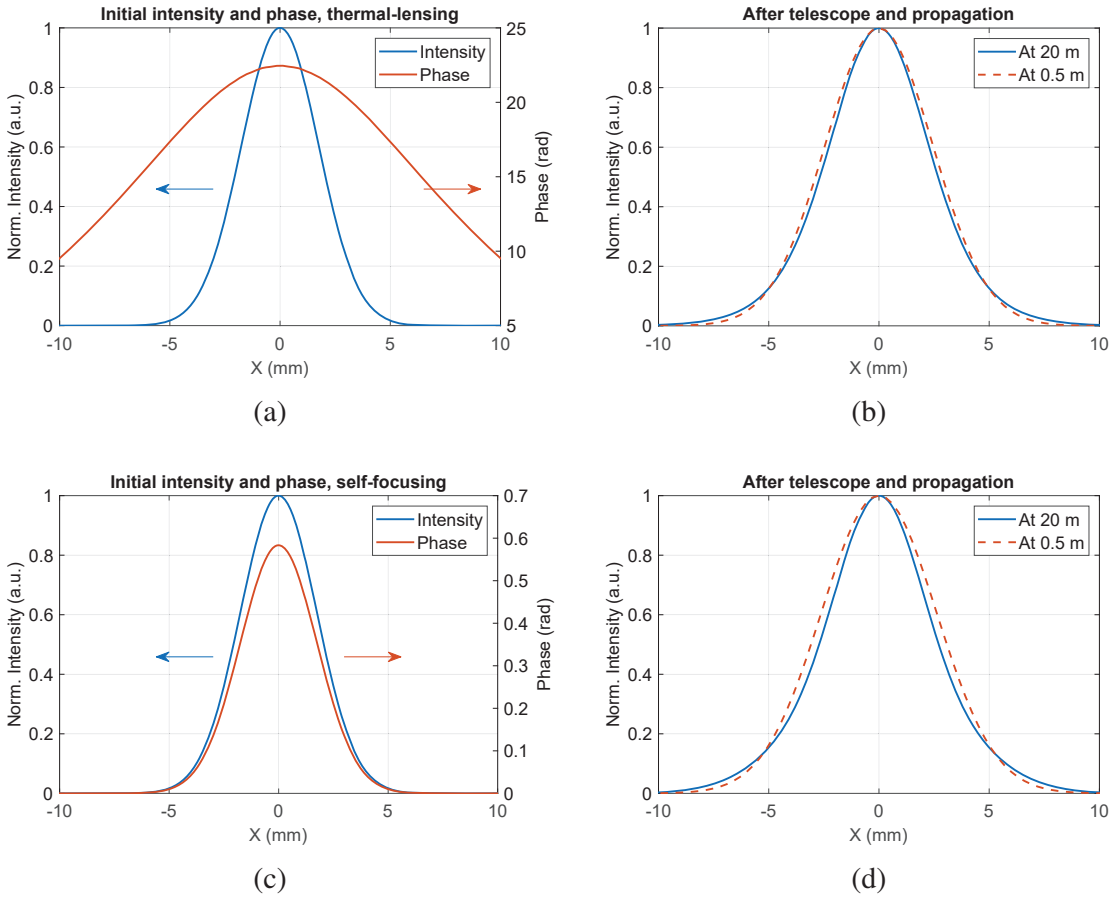

Fig. 58. Simulated Gaussian beam profile propagation with phase added due to thermal lensing and self-focusing. Both thermal lensing as well as self-focusing can add an extra phase that will cause the beam profile's FWHM to become smaller after 20 m while significant portion of the energy will be distributed outside of the $1/e^2$ diameter. Beam with diameter of 7 mm at $1/e^2$ and energy of 230 mJ is assumed at the beginning. After transmission through the Faraday rotator, the beam is magnified and collimated by the output telescope to about 10 mm at $1/e^2$ and propagated to 20 m. (a,b) – Thermal lensing. Phase profile is calculated from a simulated temperature profile using $\mathrm{d}n/\mathrm{d}T$ coefficient. Temperature simulation was done in Ansys based on coefficients of TGG from Tab. 8 and absorbed power of 0.6 W. (c,d) – Self-focusing. Phase profile is calculated from the assumed intensity profile and nonlinear refractive index n_2 of TGG.

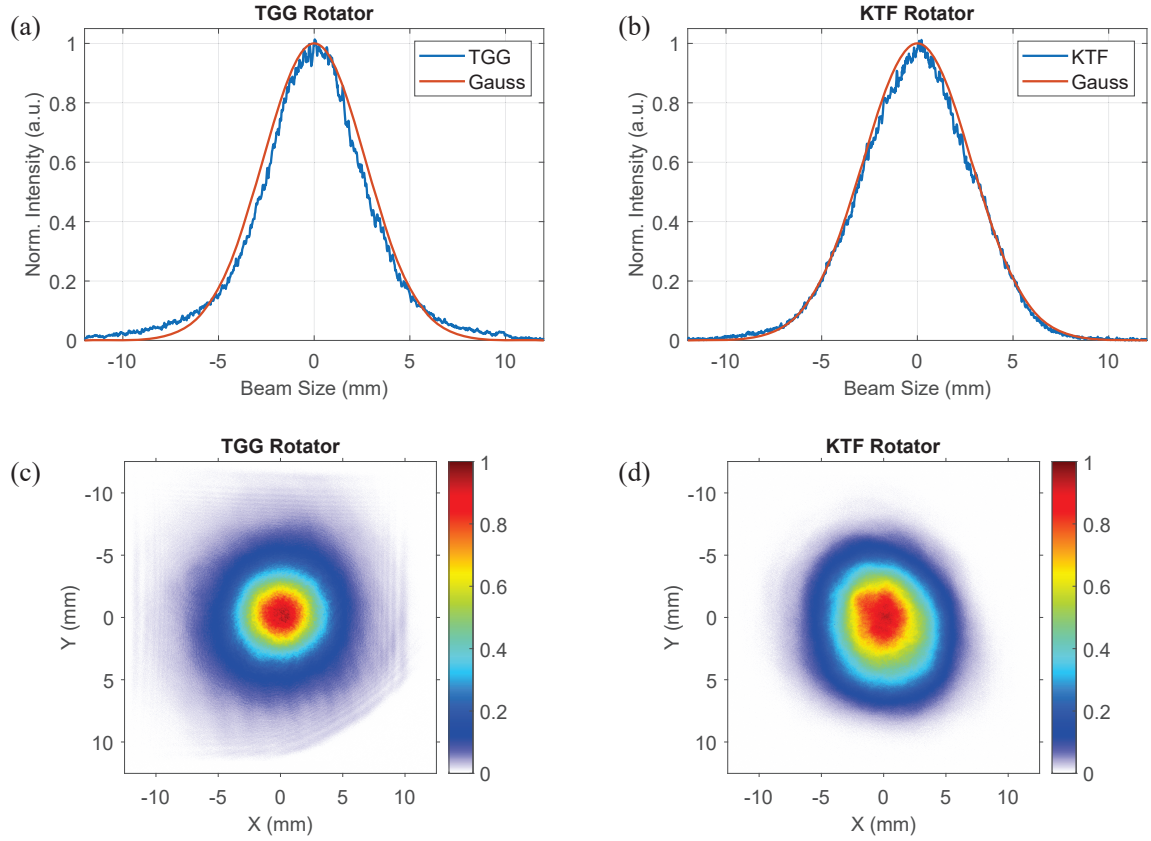

Fig. 59. DIRA 2 beam profiles after 20 m of propagation from the RA (distance to the LBO crystal plane inside the compressor). The extra Gaussian phase introduced by the TGG crystal inside Faraday rotator within the linear cavity later causes portion of the energy to be distributed outside of the main Gaussian peak decreasing the efficiency of the frequency doubling. (a,b) – X lineouts of the measured beam profiles after 20 m of propagation with two different Faraday rotators, red curves are fitted Gaussian profiles having the same diameter at $1/e^2$ as the measured lineouts, (c,d) – captured camera beam profiles.

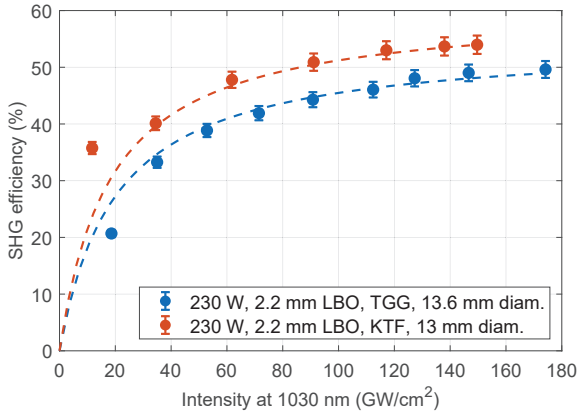

Fig. 60. Comparison of SHG results between the case with TGG (blue) and KTF (red) rotator crystal. The intensity on X axis was calculated from the measured average RA output power. It was changed by rotating the RA output waveplate. Maximum SHG efficiency with TGG crystal was 50%. Maximum SHG efficiency with KTF crystal was 54% with 108 mJ generated at 515 nm.

Thermal lensing and self-focusing experiment

In order to identify the process behind the extra Gaussian phase introduced to the pulses passing through the Faraday rotator I set up an experiment according to the layout in Fig. 61, using DIRA 2 with the new KTF rotator already inside. The presence of a rotator is needed for the correct functioning of a RA with linear cavity. The goal of this experiment was to determine whether the extra Gaussian phase is originating from self-focusing or from thermal lensing. I sent the DIRA 2 beam through an extra TGG rotator at 1 kHz and 200 Hz at different energies and measured the pulse intensity, wavefront and spectral phase. Measurements at different repetition rates but constant energy would be affected by thermal effects. Measurements at different output energy but constant repetition rate would be affected by non-linear effects. The output magnifying telescope inside the RA was removed to keep the diameter of the laser beam small. $\lambda/2$ waveplate and a TFP were used to safely absorb most of the energy transmitted through the rotator on a powermeter. Part of the leaked energy though TFP was used to measure the wavefront deformations as well as the intensity profile of the beam by a wavefront sensor (Phasics, SID4 GE). The rest of the leakage was compressed to measure the SHG – FROG trace (Picosecond FROG – PS10 from Femtoeasy). All the measurements were carried out for range of RA output energies between 1 and 200 mJ transmitted through the rotator at both 1 kHz as well as 200 Hz repetition rate[17].

The wavefront and intensity measurement results in Fig. 62 showed these two parameters of the beam stayed the same for the same average powers and different pulse energies and changed only at higher average power. Hence, thermal lensing was identified as the main reason behind the extra Gaussian phase. FROG measurements at 1 mJ and 200 mJ output at 1 kHz in Fig. 63 showed almost no changes between these two cases. The amount of extra phase introduced by the material of the original TGG crystal due to self focusing inside the rotator is negligible and does not affect the compression.

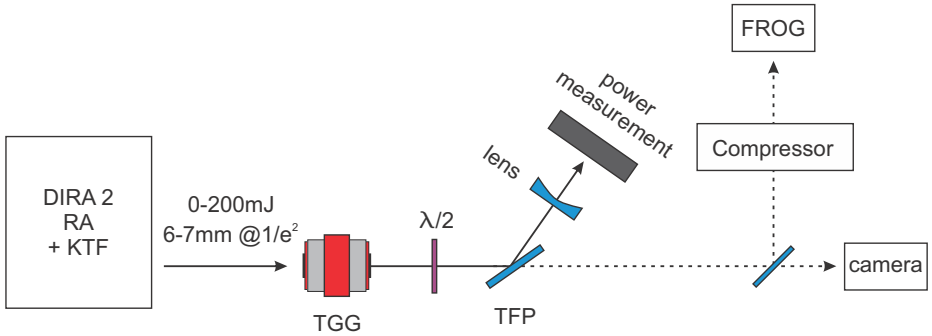

Fig. 61. Layout of the experiment verifying whether the extra Gaussian phase distorting the output beam profile originates from nonlinear effects or from thermal lensing. RA with KTF rotator inside and removed output telescope was used as a source of pulses with varying energies at both 1 kHz and 200 Hz repetition rate.

[17]Changing the RA repetition rate was done via the control software of the RA, affecting the PC triggers and diode pump timing settings.

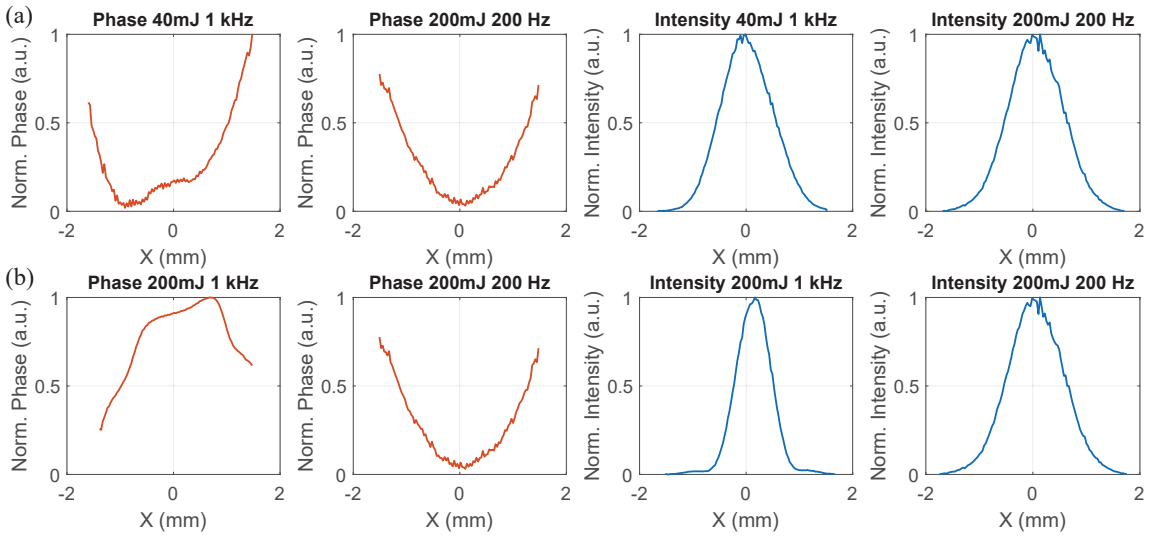

Fig. 62. Phase and Intensity profiles after transmission through 20 mm long TGG crystal. (a) – results measured at the same average power of 40 W show negligible difference between 40 mJ and 200 mJ. (b) – results measured at the same energy of 200 mJ show phase and intensity profile changes at higher repetition rate, indicating an issue with thermal lensing.

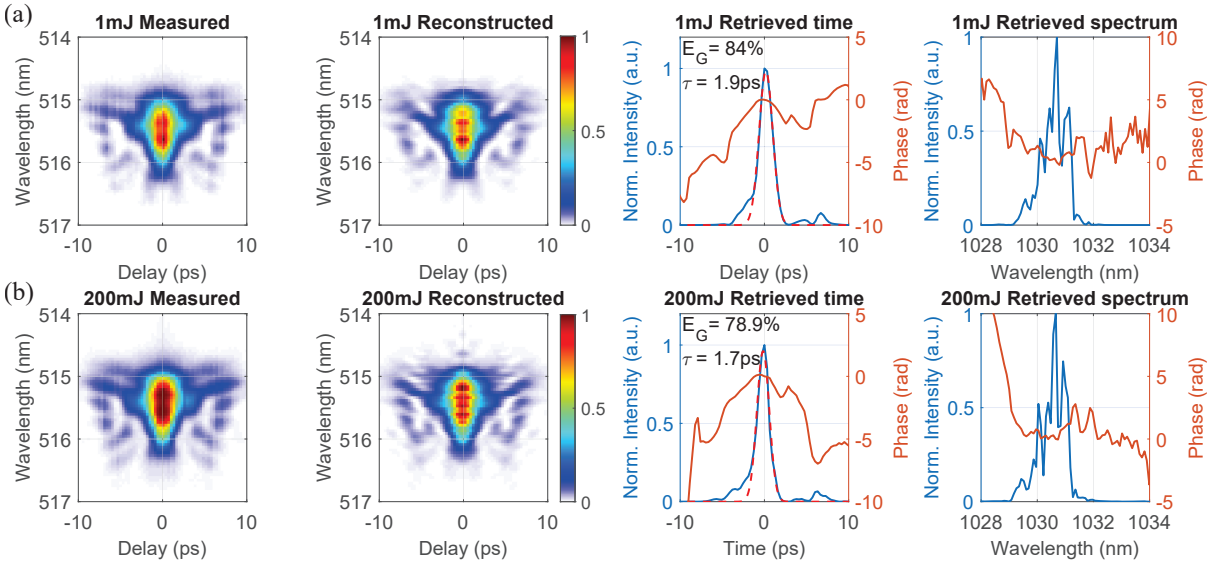

Fig. 63. Measured and reconstructed FROG traces with retrieved temporal and spectral intensity profiles at 1 mJ (a) and 200 mJ (b) at 1 kHz. Minor saturation at 200 mJ affected the reconstruction, but both retrieved profiles are very similar, showing the non-linear refractive index of TGG does not affect the dispersion of the RA output pulses and the pulse compression that follows.

4.5.3 Mitigation of Laser Induced Contamination

During the operation of 1030 nm pulse compressors and SHG stages in vacuum, the optical components in the vacuum chambers that are hit by pulses with high intensity (compressed picosecond pump pulses at both 1030 nm and 515 nm as well as compressed broadband femtosecond pulses in the chamber with amplifiers and chirped pulse compressor) develop distinct features where the beam is incident on the optic (see Fig. 64). These features can have different shapes and color, but are usually shaped like a donut (ring shape with a bright hole in the middle). The color can be either slightly black or clear with milky surroundings. The spots introduce extra absorption and distort the beam profile reflected from mirrors and transmitted through LBO crystals, or negatively affect the diffraction efficiency of compressor gratings. This limits the performance of the system and together with the need for potential damaged optic replacement affects the amount of time the system is fully operational. The LIC layers are extremely important for the SHG performance due to the heating of LBO crystals as a consequence of the extra absorption.

The details of the problem and suggested procedures to mitigate it were thoroughly described in my paper published in Applied optics [109], which is added as an attachment at the end of this thesis. It introduces the LIC problem more broadly with context to other laser systems in the world. It compares three different LIC cleaning methods (ozone cleaning, laser cleaning and plasma cleaning) and focuses on LIC affecting the compressor grating efficiency and its improvement. The paper concludes the problems with LIC can be mitigated by frequently running radio-frequency (RF) generated plasma cleaning devices on vacuum chambers and the investigation related to published results led to a review of cleanliness procedures within the ELI Beamlines projects. The list of vacuum compatible components was re-evaluated, better vacuum compatible lubricants were suggested and all the vacuum chambers are now regularly tested thoroughly with RGA before installation of any optical components inside them. All the components themselves are also tested individually with RGA and analyzed by Fourier transform infrared spectroscopy (FTIR). The newly established rules were imposed with hopes to minimize the need for using plasma cleaners on new parts of any of the laser systems at ELI Beamlines in the future. For example, one of the biggest vacuum chamber of any laser system in the world, the petawatt compressor for L4 Aton laser, was found to be not in compliance

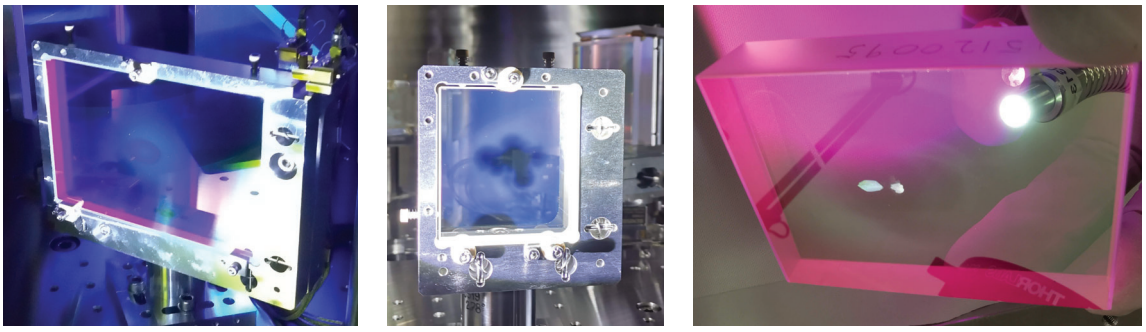

(a) (b) (c)

Fig. 64. Photo of different LIC related structures on optical components inside the pump pulse compressor and reflector tower. (a) – dark donut shape like structure with a bright spot in the middle on a dichroic mirror separating the depleted 1030 nm from the generated 515 nm beam, (b) – milky surface on a 1030 nm compressor mirror, visibly cleaned by the incident laser beam in four different places, affected by different compressor alignment, (c) – milky surface around a cleaner spot with two damaged spots in the center of a mirror reflecting 515 nm.

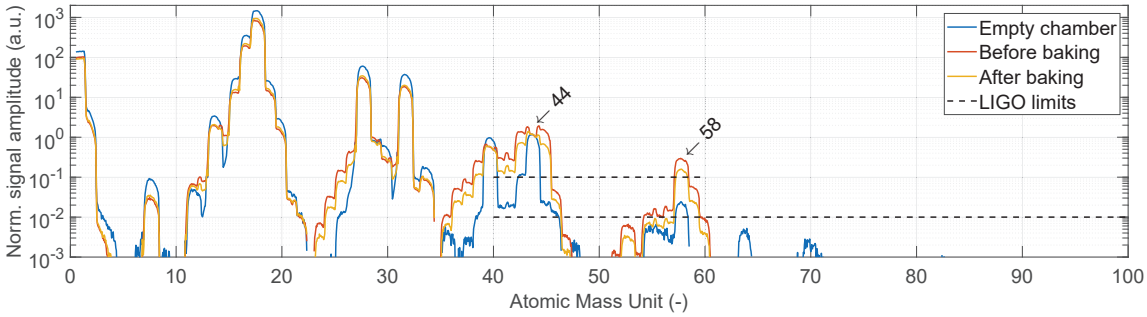

Fig. 65. RGA scan comparison of o-ring removed from the Pump beams compressor chamber. Data normalized to peak at AMU 44. Significant peak at AMU 58 before and after baking suggests a possible source of hydrocarbon contamination.

with the LIGO cleanliness criteria as the RGA scans (see Fig. 16) showed hydrocarbon contamination. After RF plasma cleaning and several days/weeks of pumping its cleanliness eventually improved and by the time of writing of this thesis, the chamber was prepared for installation of optical components.

Unfortunately, I did not have RGA scans of the compressor chamber or components installed inside at my disposal and the current RGA scans of the pump beams compressor chamber with installed mounts and optics always show plenty of hydrocarbon contamination. Running the laser for experiments frequently limited the possibilities of investigating the source of the contamination and of removing it completely. One of the possible source of the contamination might be unbaked viton O-rings that are used on all the flanges of L1 Allegra vacuum chambers. The RGA test of one of the o-rings from the compressor chamber show strong peak at AMU 58 even after baking it at 120 °C for 48 h (see Fig. 65). Hence, one of the future improvements of L1 Allegra vacuum system might involve replacing all the o-rings on all the chambers with new ones, complying with LIGO cleanliness criteria.

One of the downsides of the RF plasma source cleaning for mitigating the LIC inside the chambers is the limited cleaning range of the device itself. As mentioned in the paper, the RF plasma source placement is very crucial. We have learned the charged particles generated by the source cannot reach all the parts of the chamber at the same time and some of the optics can be cleaned only when placing the source closer to them. This complicates the cleaning procedures, as the design of the chambers include two optical tables on top of each other in the pump beams compressor for example or plenty of tubes and 90 degree corners with mirrors for the pump beams transport. This requires ideally several independent plasma sources placed on the vacuum system at the same time. As the number of the devices at ELI premises is limited and they are being shared among different research groups, it requires frequent venting of the chambers and relocating of the few plasma cleaning devices available at a given time. Despite the effort with RF plasma cleaning, several mirrors propagating the 515 nm pulses were damaged in the past and we had to replace them. Only the mirrors in the 515 nm beam transport gets damaged, suggesting the current placements of the RF plasma source prevents us from reaching those mirrors with the ionized particles and cleaning their accumulated LIC layers efficiently.

A different method of LIC removal that could be used in L1 Allegra system is the laser assisted cleaning. By using laser pulses with high enough fluence, the contaminated spot can be cleaned by a combination of laser ablation and oxygen radicals creation, which help break down the contamination layers. In order to create enough radicals, the vacuum chambers in L1 Allegra could be held at partial pressure above the typical value of 10^{-5} mbar (for example, a vacuum chamber filled with

oxygen was held at partial pressure 0.4 mbar in [109]). This can be realized by leaking air through a needle valve into the vacuum chamber on purpose. We might be able to utilize the laser assisted cleaning by running the pump laser at full power output at higher pressure in the compressor chamber and in the beam transport. This way, we might be able to remove the LIC layers even from 515 nm beam transport mirrors, which are difficult to clean with the regular RF plasma cleaner.

Despite the problems with LIC on mirrors in the beam transport of 515 nm pulses, the RF plasma cleaning is successfully mitigating any source of LIC in the compressor chamber itself. Together with the improved output beam profiles from the RA with KTF rotator described in section 4.5.2, the mitigation of LIC significantly decreased the heating of the SHG mounts to the point where the temperature stabilization was no longer necessary as long as there is no LIC present on the crystals. This improved situation is discussed further in the following section.

4.5.4 New SHG mount design with air cooling

After improving the beamprofiles of linear cavity RAs and mitigating the LIC layers on LBO crystals, the heating of the SHG mounts decreased significantly. I show in Fig. 66 how the temperature of two separate SHG mounts (for DIRA 1 and DIRA 3) changes during a few hours of full power operation. Each of the two SHG setups was different. One (for DIRA 3) had no implemented cooling solution, the other (DIRA 1) had the TEC cooling setup described earlier in section 4.5.1. The temperature sensors were mounted on the moving part of the kinematic mounts holding the insert with LBO crystal. During the experiment, the TECs were not powered and the cooling setup acted only as a passive heat-sink for the SHG mount. This passive thermal contact resulted in slower temperature rise of the SHG mount. The measured temperature change in the case of the mount with no cooling solution agrees with the heating caused by the measured absorption in LBO coatings only (producing 30 mW of heat with 200 mJ incident pulses at 1 kHz).

Two of the three pump beams compressors are designed to handle 1 J of energy at 1030 nm for potential upgrades of RA in the future (one being the multipass amplifier for DIRA 3 already under construction to provide stronger pump pulses for OPCPA stage 7). The SHG stages of the upgraded pump lasers will have to handle up to 5 times higher heatload due to absorption in the crystals and it

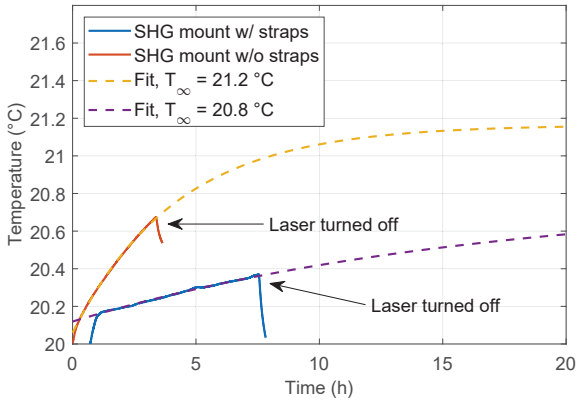

Fig. 66. Temperature of the SHG mounts with (DIRA 1) and without (DIRA 3) implemented cooling solution (TECs were not powered). The resulting temperature difference of 1.2 °C in the DIRA 3 SHG mount without any added components would not cause the energy of pulses at 515 nm to decrease by more than 1% during 24 h of operation. Data were fitted with function describing the temperature evolution in transient heat conduction problems [120], where T_∞ is the final temperature.

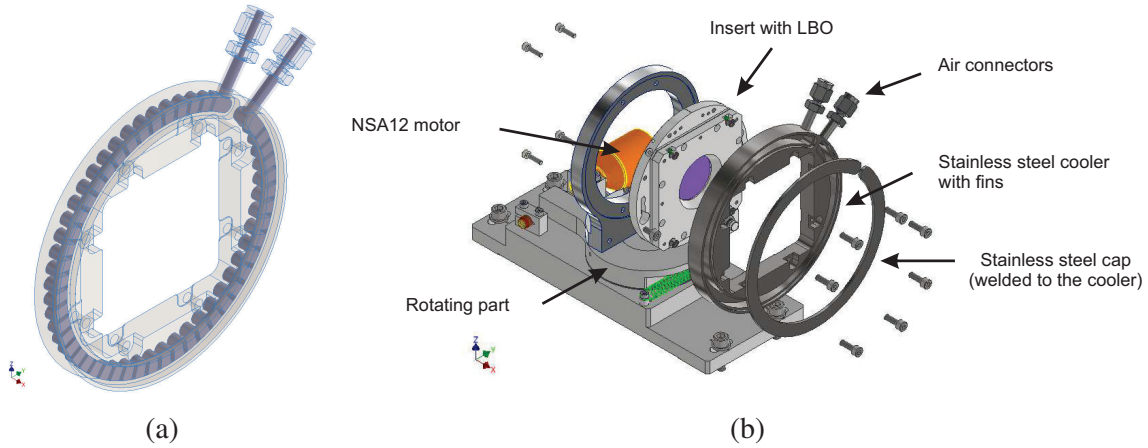

Fig. 67. New SHG mount with air cooled stainless steel attachment. (a) – cooler with highlighted air channel. With air flow of 3 m / s at 3 bar available from the laboratory air supply, the cooler is capable of removing up to 2 W of heatload. (b) – New rotational SHG mount with air cooler capable of being mounted on top of the insert with LBO crystal. *Simulations realized by Gavin Friedman, design by Petr Strkula.*

would be convenient to have a cooling solution ready. On top of that, during the L1 Allegra operation, we have discovered that the OPCPA stages 5 – 7 are heating up faster than the simple LBO absorption calculations suggest (despite mitigating LIC growth by plasma cleaning). These stages would also benefit from a suitable cooling solution. To address these needs and improve the disadvantages of the original cooling setup, a new air cooling solution has been designed in collaboration with Gavin Friedman and Petr Strkula. It is smaller (usable in OPCPA stages 5 – 7 as well), does not transfer the excess heat to the optical table but rather outside the chamber and does not block the clear view of the inspection cameras monitoring the LBO crystals. It has a form of stainless steel ring, which can be attached to the round insert with LBO crystal. The cooling is achieved by air flowing from a feedthrough on the chamber through a Swagelok tubing connected to a sealed channel with multiple fins. Fins create turbulent flow of air, utilizing higher heat transfer coefficient, and increase surface area. Based on Ansys convection simulations, the channel is capable of removing 2 W of heat with only 3 m / s air flow at 3 bar (compatible with compressed air source in the laser hall). The design with highlighted air channel is shown in Fig. 67a.

Together with new air cooler, the new SHG stage design was also created with higher reliability in mind. The design is using rotational movement rather than kinematic mount, it has lower weight compared to the previous design and together with stronger stepper motor (NSA12V6) minimizes the risk of the mount getting stuck. The option of adjusting the pitch of the LBO crystal was omitted based on experience with previous mounts in the chamber. The new mount has an option of encoding so the precise angle of the LBO rotation can be monitored remotely. It is also compatible with the inserts from the previous versions of the mounts, it enables easy attachment of the air cooler and a model of both is shown in Fig. 67b. This new mount, including the air cooler, has already been successfully tested in the chamber, where it replaced the SHG mount for DIRA 3 beam (see the pictures in Fig. 68). The output SHG energy when using the new mount and the stainless steel cooler was the same as with the old SHG mount without any implemented cooling solution.

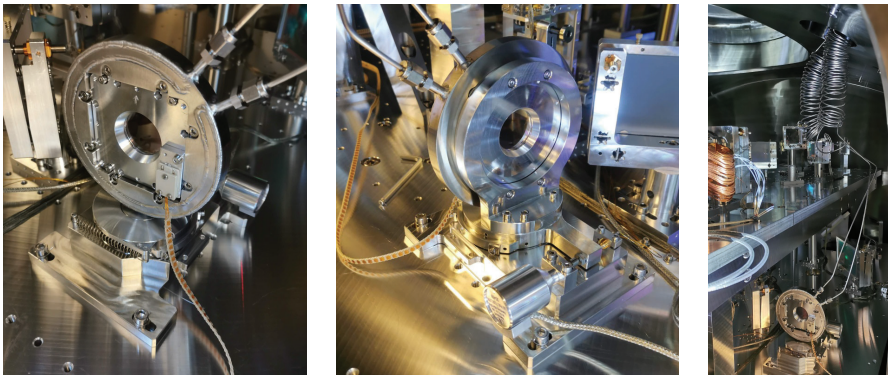

Fig. 68. Air cooled new SHG mount. Swagelok tubing allows air flow from feedthrough on the chamber to the cooler, removing the heat outside rather than transferring it to the optical table.

4.5.5 Different front-end and seed energy experiment

I already mentioned in section 4.4.3 that the performance of pump lasers is influenced by the performance of the Ti:sapphire oscillator at the beginning of seed distribution and its limited energy available for the first FA. ASE present in the seed pulses gets amplified in the RA and decreases the maximum SHG efficiency of the pump lasers. There is also a separate pump laser under development in L1 lab, not part of the L1 Allegra chain, which uses a different front-end (meaning the oscillator and seed distribution system). This pump laser provides 2 x 50 mJ pulses at 1030 nm with 1 kHz repetition rate. Its front-end comprises of Yb:fiber modelocked oscillator (Origami), CFBG stretcher, one FA and MZM for picking 1 kHz pulses from the 80 MHz train. The FA in this front-end is seeded with pulses having higher energy from the Yb-based oscillator. As a consequence, less ASE is present in seed pulses from this front-end. In addition, the seed energy available at the input of this RA is higher than in DIRA 1[18], and the overall gain of this RA is lower. As a result, the 2 x 50 mJ RA has higher contrast when compared with DIRA 1 (shown earlier in Fig. 41b). More importantly, its SHG efficiency is 73%. This is the highest SHG efficiency reached with any pump laser at ELI Beamlines. To see how much a pump laser using DIRA could benefit from using the Yb:fiber oscillator based front-end with less ASE in seed pulses, I used the output from this front-end to seed DIRA 1.

Seeing how good the SHG efficiency of the 2 x 50 mJ RA is, I also wanted to evaluate the DIRA 1 based pump laser performance operated at lower gain. With the Yb:fiber oscillator based front-end, I operated DIRA 1 at two pump power settings. One at lower gain, generating only about 120 mJ at the output, the other at the usual 230 mJ output. To have a comparison with Ti:sapphire oscillator based front-end as well, I wanted to see if increasing the seed energy has any effect on the pump laser performance. I bypassed some of the Ti:sapphire seed distribution elements (splitters and fiber delays) to boost the seed energy to 170 pJ. In all cases I measured the output energy at 1030 nm, output temporal profile before compression, contrast, pulse duration after compression, output 515 nm energy, and SHG efficiency. With this, I had 5 sets of data available – two sets with Ti:sapphire front-end with seed pulse energy of 12.5 pJ and 170 pJ, two with Yb:fiber front-end at 119 mJ and 230 mJ output energy, and one with Yb:fiber front-end from the 2 x 50 mJ RA (measured by Jakub Novák and Emily Erdman).

[18]The measured seed energy for this RA is 250 pJ, which is 20 times higher than seed energy used for DIRA 1, although not all of the energy is distributed precisely at 1030 nm and used effectively during amplification. The reason is higher reflection bandwidth of the CFBG stretcher for this RA, which is 10 nm. The reflection bandwidth of the stretcher for DIRA lasers has only 2.5 nm.

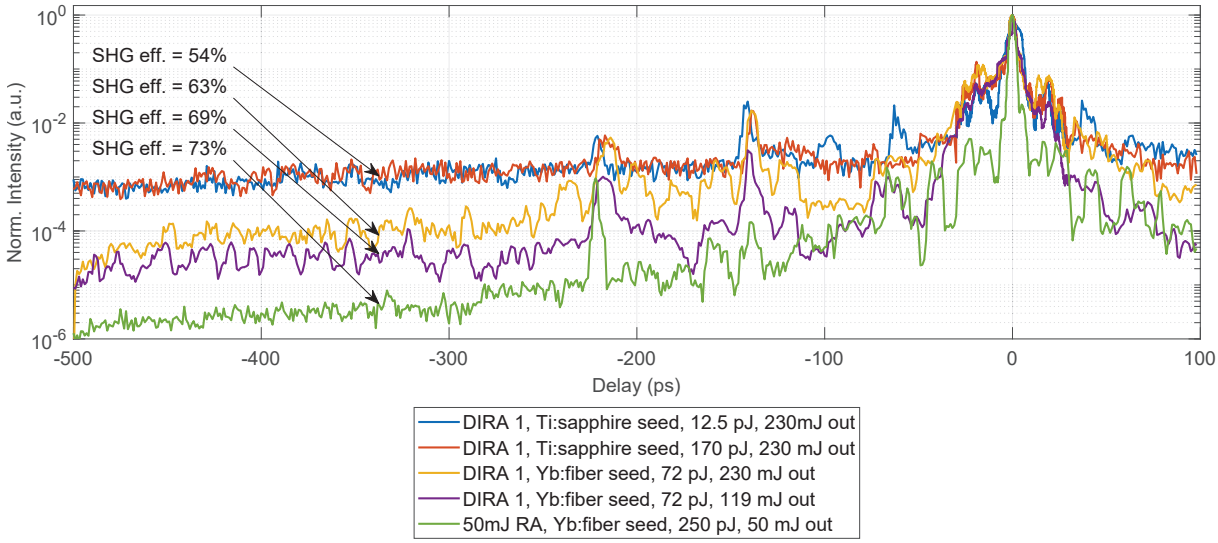

Fig. 69. Contrast of DIRA 1 seeded by Yb:fiber oscillator based front-end and Ti:sapphire oscillator based front-end with various energies at different settings. The best SHG efficiency was reached with Yb:fiber oscillator based front-end operating only at 119 mJ in the cavity. Measurement comparing the 50 mJ RA included. Different contrast between DIRA 1 operated at 230 mJ and 119 mJ is most probably originating from the RA different ASE amount at different pump levels (at different gain). Lower contrast of DIRA 1 around 0 ps is affected by the stretcher optimized for best compression in vacuum while the contrast data had to be measured in air. Compression of the 50 mJ RA pulses on the other hand is always realized in air and the stretcher is optimized for air as well. That is why the contrast around 0 ps is so much better.

In agreement with previous data (Fig. 40) showing little difference when seed energy was decreased, there was little difference between the performance with Ti:sapphire oscillator front-end and seed energies of 12.5 pJ and 170 pJ. Interestingly, the pump power needed to reach 230 mJ output was the same and the contrast (shown in Fig. 69) almost didn't change. Since the seed energy was increased by bypassing fiber components just before DIRA 1 and not by changing the Ti:sapphire oscillator or the first FA, there was still ASE pedestal visible on the temporal output pulse profile before compression (see Fig. 70a). The maximum SHG efficiency was 54% (shown in Fig. 71b) for both seed energies. According to the SNLO simulation matching the measured SHG data, only about 56% of the energy at 1030 nm is effectively used for frequency conversion.

With Yb:fiber oscillator front-end, the contrast of DIRA 1 improved by about one order of magnitude (Fig. 69). The seed distribution related ASE pedestal decreased (Fig. 70a) and SHG efficiency improved when compared to the case with Ti:sapphire front-end (Fig. 71a).

Looking at the contrast data, it is clear that with the Ti:sapphire oscillator based front-end, more seed energy does not improve the contrast and the fact that SHG efficiency stayed the same, while it improved later with Yb:fiber oscillator based front-end, suggests good contrast is essential for the SHG efficiency. In other words, with certain level of ASE already present in seed pulses, higher seed energy does not lead to higher SHG efficiency. There might be a benefit of running the RA at lower gain though. With lower gain, ASE generated as a consequence will be lower. There is a difference in contrast between DIRA 1 running at 230 mJ and 119 mJ in the cavity (Fig. 69). The 3rd order AC scanning range spans only 600 ps, making it impossible to fully measure the level of $\sim$100 ns ASE pedestal originating from the RA. Maximum SHG efficiency of DIRA 1 was 69% in case with 119 mJ in the cavity and 63% in case with 230 mJ in the cavity. The SNLO fit of the SHG

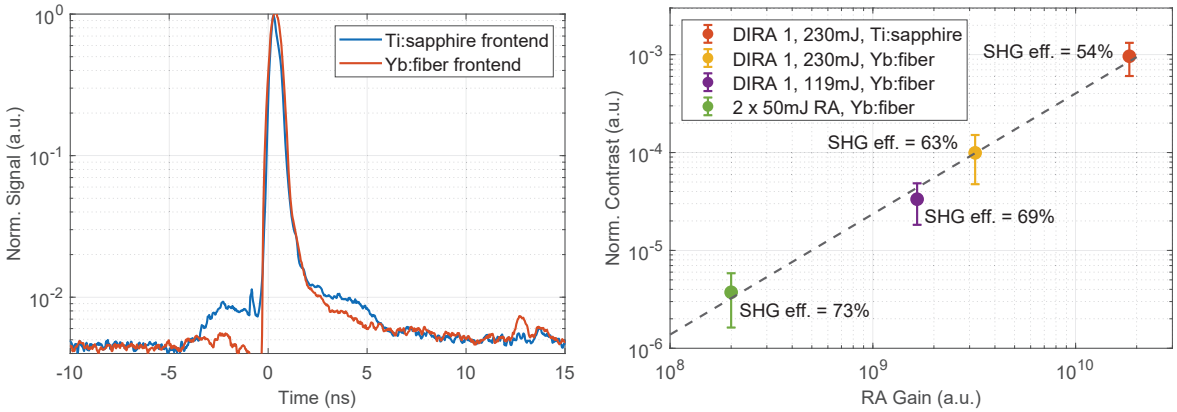

(a) (b)

Fig. 70. RA output characteristics with different front-ends. (a) – DIRA 1, output pulse measurement before compression, showing lower ASE pedestal when Yb:fiber oscillator based front-end is used to seed DIRA 1. (b) – contrast dependency on RA gain when using both front-ends. The SHG efficiency improves with better contrast.

data from DIRA 1 seeded by the Yb:fiber oscillator based front-end shows the energy effectively used for frequency conversion is 70% at 230 mJ and 80% at 119 mJ (compared to 54% at 230 mJ in case of DIRA 1 seeded by the Ti:sapphire oscillator based front-end). The main difference between the case with 230 mJ and 119 mJ is different contrast related to different gain and ASE level. Compression was optimized by the tunable stretcher in both cases to reach the same pulse duration of 1.9 ps. Beam diameter slightly increased from the measured 13.3 mm at 230 mJ to 13.6 mm at 119 mJ and this 2% difference does not explain improved SHG efficiency at 119 mJ.

SNLO simulation matching the 119 mJ output data show, that the maximum SHG efficiency with this contrast could reach 75% at RA output energy of 230 mJ. This important finding could potentially enable generation of pulses with up to 150 mJ at 515 nm at 2 ps in the future if such contrast can be maintained at full power operation of the RA.

Measured FROG traces and reconstructed spectral and temporal profile of DIRA 1 and 2 x 50 mJ RA using the Yb:fiber oscillator based front-end are shown in Fig. 72. The overview of all the results with different front-ends, including the results shown previously in other section of this thesis is shown in Fig. 73.

Results showed in this section suggest that ideally, the DIRA lasers should be seeded with clean pulses with as low ASE as possible using as low gain as possible. Lower ASE might be addressed by replacing the current front-end with a Yb:fiber based one. Lower RA gain might be reached by designing the new front-end to provide as much seed energy as possible. I addressed these requirements by suggesting a modified seed distribution system on page 83. The results shown in Fig. 71 address the issue raised in the aims of this thesis - that is, how to improve the performance of the pump lasers so they could generate the designed pulses with energy of 120 mJ at 515 nm at 3 ps. If the current Ti:sapphire oscillator based front-end is replaced by an Yb:fiber oscillator based one, DIRA based pump lasers will be able to reach an intensity close to 100 GW / cm^2 and SHG efficiency above 60%. With these parameters, pulses with more than 120 mJ at 515 nm at 3 ps could be generated. If the Ti:sapphire oscillator is kept for generating the broadband signal pulses, synchronization of the two oscillators will have to be solved. Otherwise, supercontinuum generation of broadband pulses from the 1030 nm pump pulses would have to be implemented.

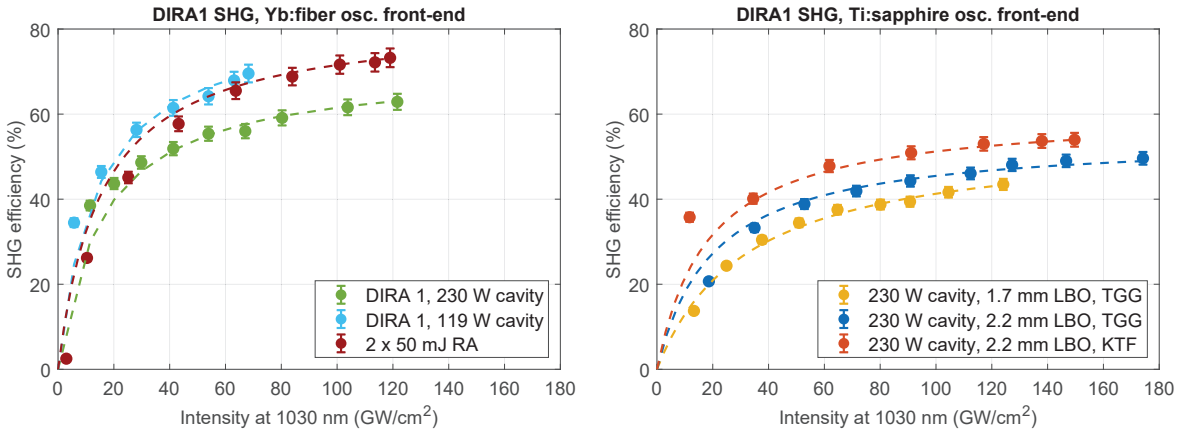

(a) (b)

Fig. 71. Comparison of all measured SHG efficiencies reached with DIRA 1. The best results were reached with low ASE pedestal and good contrast while using Yb:fiber oscillator based front-end. Full points – measured data, dashed lines – SNLO simulation. The intensity on *X* axis was calculated from the measured average RA output power. It was changed by rotating the RA output waveplate. (a) – results with Yb:fiber oscillator based front-end while running DIRA 1 at two different cavity powers (119 W in light blue, 230 W in green). According to the SNLO simulation matching the data measured with 119 W in the cavity at 1.9 ps (light blue dashed line), 15% of energy is still not efficiently used for frequency conversion. Data from the 2 x 50 mJ RA included for comparison (dark red). All three results measured with 2.2 mm LBO crystal. (b) – results with Ti:sapphire oscillator based front-end and cavity power of 230 W. I include the data with TGG as well as KTF crystal in Faraday rotator for comparison.

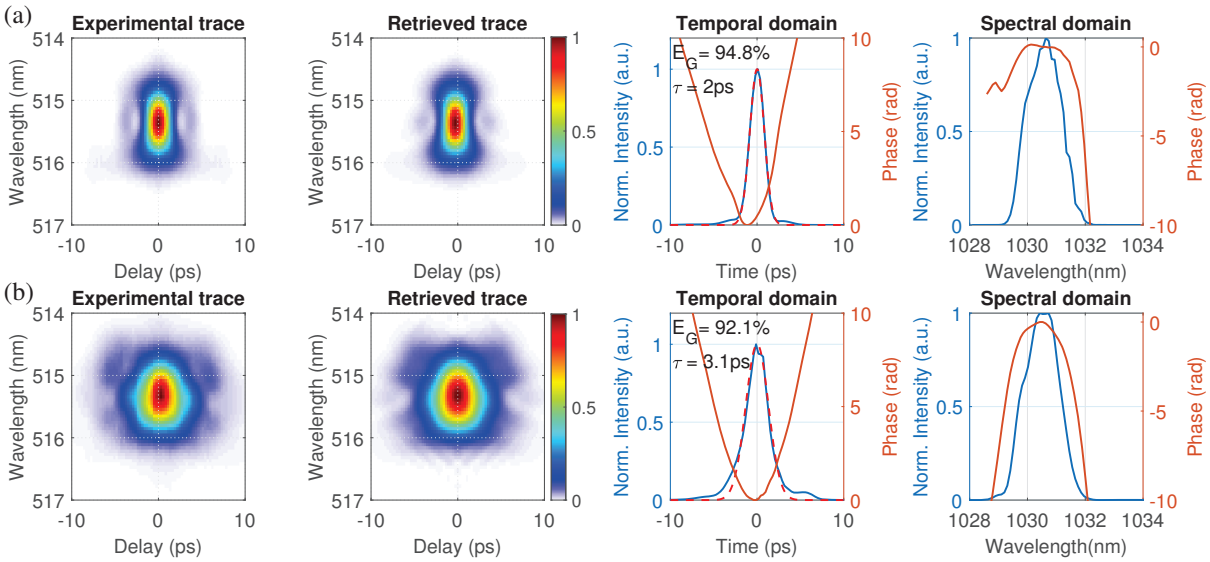

Fig. 72. SHG – FROG traces of RAs seeded by the Yb:fiber oscillator based front-end. (a) – DIRA 1 output pulse with 119 mJ in the cavity. Stretcher was optimized to reach 2 ps pulses. With this settings, the best contrast of DIRA 1 was reached with the highest SHG efficiency. (b) – 2 x 50 mJ RA with positively stretched pulse. SHG efficiency of this laser is 73%. *FROG trace of 2 x 50 mJ RA measured by Jakub Novák and Emily Erdman.*

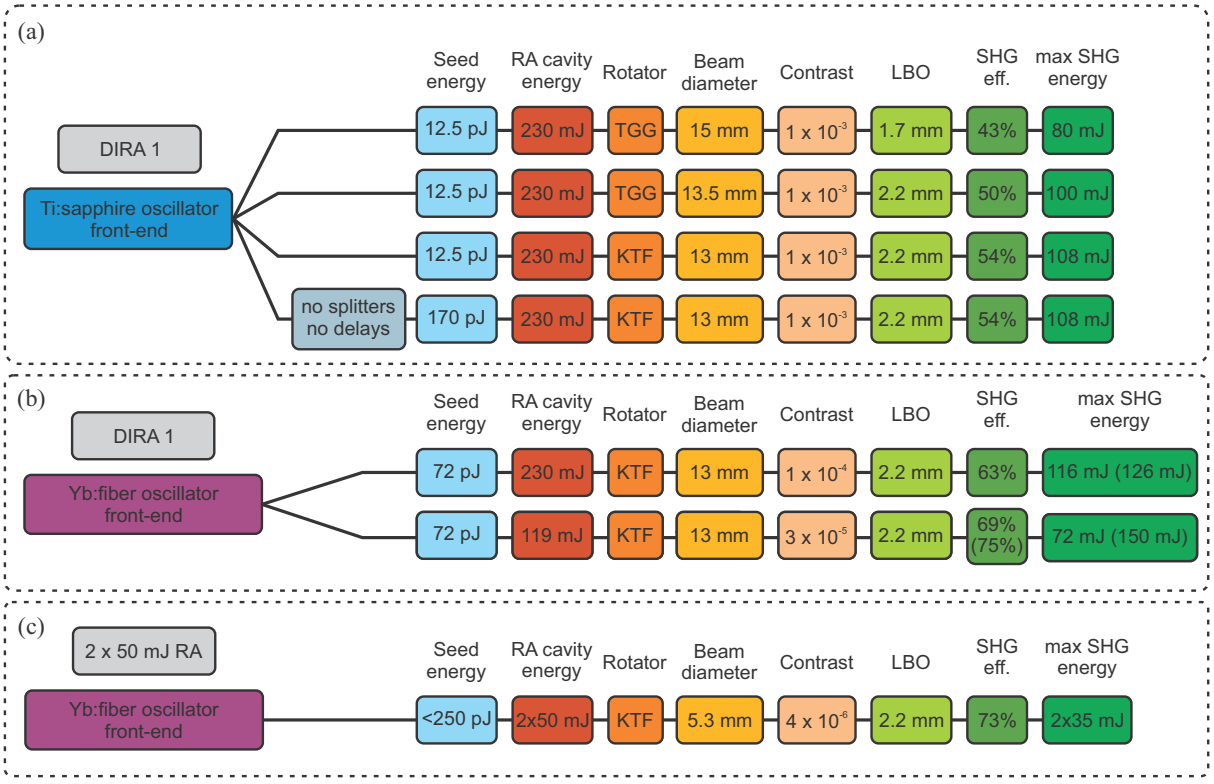

Fig. 73. SHG results overview. (a) – results from DIRA 1 using the Ti:sapphire oscillator based front-end. Using longer LBO crystal led to an improvement of SHG efficiency from 43% to 50%. Smaller beam diameter and better beam profile with KTF Faraday rotator increased it to 54%. Increasing the seed energy did not lead to any improvement. (b) – results from DIRA 1 using the Yb:fiber oscillator based front-end. With this front-end, DIRA contrast improved by an order of magnitude and SHG efficiency increased to 63%. Maximum output energy at 515 nm of 116 mJ was limited by using only 212 mJ of output energy at 1030 nm due to LIDT concerns. At full output of 230 mJ, 126 mJ at 515 nm would be achieved. Operation of DIRA 1 with lower gain resulted in further contrast and SHG efficiency improvement. Maximum theoretical efficiency in this regime at full output energy of 230 mJ would reach 75% with 150 mJ energy at 515 nm. (c) – results from 2 x 50 mJ RA using the Yb:fiber oscillator based front-end. Intensity on the LBO crystal was comparable between DIRA 1 and this RA ($\sim 120\,\mathrm{GW/m^2}$).

5. Conclusions

In order to provide the pump pulses for OPCPA stages of the L1 laser systems at ELI Beamlines, Yb-doped thin-disk based RAs were chosen as the most promising technology. They have already proved to be able to provide pulses compressible to picosecond time duration with high energy, good stability and beam quality and high repetition rate at 515 nm for stages 1 – 4 in L1 Allegra system [54]. This thesis focused on development and improvements of pump lasers for OPCPA stages 5 – 7 that are crucial for the future use of the L1 Allegra system and are still not available commercially.

5.1 Summary of achieved results

The pump lasers for OPCPA stages 5 – 7 are based on commercial RA from TRUMPF Scientific lasers, and MLD gratings compressors with LBO SHG stages placed in vacuum. Each of the RAs is capable of producing 230 mJ pulses at 1030 nm and 1 kHz with long term average power standard deviation of 0.2% and about 1% standard deviation of pulse to pulse energy stability. The M^2 is < 1.2 in both axes. The compressors are capable of compressing the pulses to about 1.5 ps duration and good beam pointing stability < 10 μrads after the compressor at 1030 nm is achieved by active beam pointing stabilization.

In my research I focused on finding reasons behind low SHG efficiency, on temperature stabilization of the SHG mounts, on beam profile improvement of RA with linear cavity design and on mitigation of LIC in vacuum. Higher SHG efficiency enabled generation of pump pulses with more energy at 515 nm, which helped reach higher output energy from OPCPA stages 5 – 7. Temperature stabilization of SHG stages enabled stable output at 515 nm without the need for frequent phase-matching corrections in LBO crystals. Beam profile improvement increased the amount of energy available for effective frequency conversion at 1030 nm and prevented heating of the SHG mounts by scattered light. Mitigation of LIC in vacuum prevented layers causing extra absorption from developing on optical components with compressed pulses. The results can be summarized as follows:

- The initial SHG efficiency of the pump lasers was only 43%. By changing the output telescope inside RAs, the beam diameter was decreased from 15 mm to 13.5 mm. Together with LBO crystal with thickness of 2.2 mm instead of 1.7 mm, the efficiency was improved to 50%.
- Non-Gaussian beam profiles at the output of two linear cavity RA were improved by replacing the Faraday rotator crystals. This increased the amount of energy available for effective frequency conversion and also caused the output beam diameter to decrease from 13.5 mm to 13 mm. Combination of both effects improved the SHG efficiency to 54%.
- The thickness of LBO crystals in SHG stages for each of the three RAs is currently 2.2 mm, 2.1 mm and 1.7 mm. Only the pump laser with 2.2 mm currently have the SHG efficiency of 54% and thicker crystals needs to be purchased for the other two. According to theoretical simulation, crystals with thickness up to 3 mm can be used without the risk of back-conversion from the 515 nm to 1030 nm.
- The contrast of the RA output pulses at 1030 nm strongly depends on the performance of the Ti:sapphire oscillator and suffers from inherently high ASE caused by poor contrast of seed pulses. Sub-optimal contrast and the consequent amount of energy not contained in the main Gaussian temporal peak is the main contribution to low SHG efficiency.
- A different amount of dispersion added to output pulses inside each RA requires different stretcher settings for each pump laser to reach perfect compression. Since 4 pump lasers in the L1 Allegra

system share the same CFBG stretcher, this prevents them from reaching the same SHG efficiency at the same time. New separate stretchers for each of the pump lasers were ordered to be later installed in the seed distribution system.

- Using a front-end based on Yb:fiber oscillator to seed one of the pump lasers showed SHG efficiency above 63% can be reached in the future if the RA are pumped by seed pulses with less ASE. Together with the suggestion of separate stretcher for each of the pump lasers, this finding resulted in a new design for seed distribution system.
- Compressed pulse propagation in vacuum develops laser induced contamination (LIC) layers on optical components. LIC layers developed on gratings and mirrors in compressor, on LBO crystals and on subsequent mirrors for beam transport of 515 nm beam. These layers were mitigated by regular radio-frequency generated plasma cleaning.
- During pump laser development, issues with rising temperature of the SHG mounts for two pump lasers with linear cavity RAs were solved by active temperature stabilization with TEC elements. This solution was later not necessary, due to LIC mitigation by plasma cleaning and due to beam profile improvement by the Faraday rotator crystals replacement.
- The experience gained by working with vacuum SHG stages led to a design of improved version of the SHG mount. To address the potential heating of the SHG stages in the future upgraded versions of pump lasers with multipass amplifier, these new stages also comprise of stainless steel part cooled by air from outside the chamber. This new cooler can also be used for stabilizing the temperature of the vacuum OPCPA stages, which are currently heating up.

Despite the issues with sub-optimal contrast and low SHG efficiency, the three pump lasers can regularly generate 75 – 100 mJ at 515 nm with pulse duration between 2 – 3 ps. DIRA 1 and DIRA 2 are already frequently used for pumping the OPCPA stages during experimental campaigns. They recently helped achieve an important milestone of amplification of the broadband pulses of L1 Allegra to 55 mJ. Based on the summarized results, I can state that all the aims of my thesis were successfully accomplished.

5.2 Contributions of the author

In any large project such as ELI Beamlines, one can never achieve all the results by himself. This was also my case, as I did my research on a system designed and partly developed by other colleagues and collaborating companies. I joined the development of the three pump lasers in 2016. Back then DIRA 1 and the vacuum chamber with first compressor and SHG stage were installed by Robert Boge in section of the HiLASE laboratory in Dolní Břežany. After carrying out the first SHG experiments at full output power together, we moved the system to the newly built L1 hall within ELI Beamlines premises. Together with other colleagues we cleaned, moved and installed most of the hardware into L1 lab and I helped installing all the pump laser key parts. This included installation of DIRA lasers, mounting optical components in air as well as in vacuum, building diagnostic setups, and providing feedback to debug and improve control system software. Together with Robert I was responsible for commissioning the RA, the compressors and SHG stages, and for RA repairs. As a part of my thesis, my responsibility was then to identify all the potential issues preventing the pump lasers from reaching the designed output energy at 515 nm. I suggested the main ideas behind the cooling TEC setup based on simulations I carried out, I suggested the solution for improving the non-Gaussian beam profile, and I was leading the efforts to mitigate the LIC. I also tested the different front-end to prove that the pump lasers can operate at the designed parameters if the seed pulses contain less ASE.

The resultant benefits of my work can be quantified by the number of hours the L1 Allegra system was provided to the experimental groups. Out of the total of 184 h of L1 Allegra operation in 2019, OPCPA stage 5 was operated for 13 h. Out of the total of 313 h in 2020, OPCPA stage 5 was operated for 186 h, and stage 6 for 20 h. In 2021, the number of total hours as well as stage 5 and 6 operation hours doubled compare to 2020. This proves the benefits of having the pump lasers that can be operated reliably on a daily basis. With further improvements, they will eventually enable the L1 system to reach the designed output energy of 100 mJ at 15 fs.

Before I started to work on pump lasers in the L1 Allegra system, I spent 2 years building a smaller pump laser for the L2 DUHA laser system, comprising of a 30 mJ-level RA with repetition rate 1 kHz, M^2 below 1.15 in both axes and pulse to pulse energy stability standard deviation of 0.5%. I solved the problem with damaged coating for pump wavelength of 969 nm inside the laser head that was causing the output power of the RA to decrease by 30%. I built the compressor with SHG stage, which provided pulses with energy of 17 mJ at 515 nm at 1.8 ps with SHG conversion efficiency of 62%. This pump laser is now used for the first 3 OPCPA stages in L2 DUHA system.

During the time of my PhD studies, I was the first author of 2 and co-author of 5 papers published in peer-reviewed journals (the two with my authorship are attached in the appendix of this thesis). I presented 3 and co-authored many other conference contributions. I also enjoyed teaching several years of laser physics and laser laboratory classes at FNSPE CTU in Prague.

6. Outlook

In order to improve the performance of the three pump lasers in L1 Allegra described in this thesis, I suggest a few upgrades and improvements. The goal is to obtain output parameters closer to the designed values of 120 mJ at 515 nm with pulse duration of 3 ps and more reliable day to day operation. They include a redesigned seed distribution system, longer LBO crystals, and a few changes to the vacuum system.

The new seed distribution system (Fig. 74) addresses the delivery of seed pulses with minimum ASE with optimized dispersion, which would improve the contrast and SHG conversion efficiency. These would be the key points of the new design:

- Yb:fiber oscillator at the beginning.
- Individual stretchers, with central wavelength at 1030.7 nm to reflect the shifted output wavelength and allowing custom dispersion compensation of each RA separately.
- Avoiding the use of acousto-optic modulator, minimizing the number of fiber amplifiers in each branch and limiting the risk of replacements.
- Free space pulse picking with Pockels cells with lower losses, replacing the MZMs.

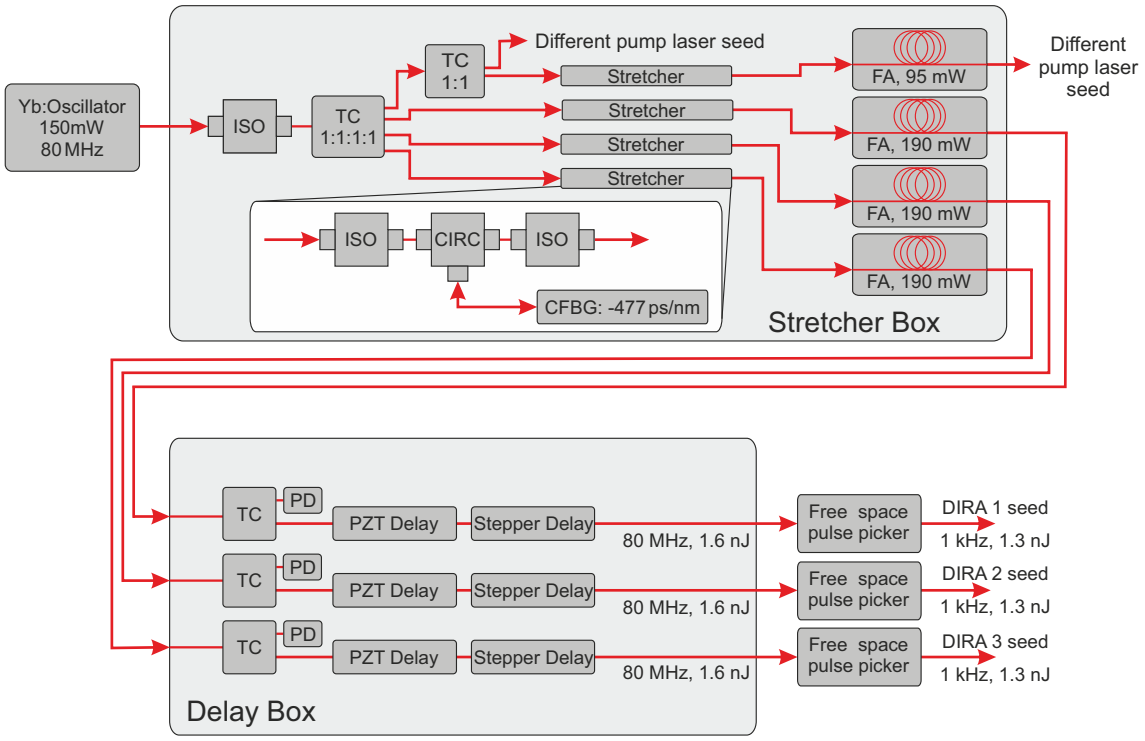

Fig. 74. New seed distribution design with Yb:fiber oscillator at the beginning, separate stretchers for each RA, fewer components and free space pulse picking. The original seed distribution layout is shown in Fig. 20.

If implemented, the new seed distribution would help utilize the good contrast and SHG efficiency above 60% shown earlier in section 4.5.5. This would lead to the generation of 515 nm pump pulses with energy above 120 mJ at 3 ps at 1 kHz. Picosecond OPCPA requires femtosecond synchronization

of the broadband signal and the pump pulses. One disadvantage of the new design is the need to address the optical synchronization due to the introduction of a new fiber oscillator.

There are two options for the generation of the broadband pulses. The first is to maintain the Ti:sapphire oscillator as the source of the broadband signal while using a new Yb:fiber oscillator to seed the pump lasers. This will be experimentally difficult, as we will need to obtain femtosecond synchronization between two independent oscillators. We have yet to show that this is achievable, with proof-of-principle experiment planned to be realized in L1 this year. The second option is to generate the broadband signal pulses with supercontinuum stage pumped by the output of the RA itself, which will be seeded by the fiber oscillator. OPCPA systems with single oscillator and supercontinuum generation already exist. In [39] for example, an OPCPA system with signal pulses generated by supercontinuum and signal-pump jitter of less than 10 fs was published. Another example would be the Sylos system used in ELI-ALPS [44].

Even without replacing the Ti:sapphire oscillator, the suggested seed distribution changes could be implemented. The amount of ASE in the seed pulses would still be limited by the combination of the Ti:sapphire oscillator and the first FA. The main advantage though would be the custom dispersion compensation due to the individual stretchers for each pump laser. Final seed energy available for DIRA lasers would probably be limited to maximum of 0.3 nJ in this case.

With Origami-based front-end and 119 mJ in the cavity of DIRA 1, the best achieved efficiency was 69%. The SHG simulation matching the measured data still show about 15% of energy missing from the central temporal peak, which is not efficiently converted to 515 nm. As a consequence, the intensity of the fundamental pulses on LBO crystal is smaller. To compensate for this, one could decrease the beam diameter or the pulse duration of the 1030 nm pulses. By doing this, we would risk exceeding the LIDT limits of optics used in the compressor and the subsequent beam transport of 515 nm pulses. Instead, we could use longer LBO crystals. SNLO simulation suggests crystals with 3 mm thickness for all three SHG stages could still lead to improved SHG efficiencies and higher generated pulse energies without back-conversion of pulses from 515 nm back to 1030 nm.

The vacuum system could benefit from replacing the o-rings on all the flanges in order to improve the cleanliness inside compressor vacuum chamber, which might decrease the required frequency of plasma cleaning. Also, laser cleaning during elevated chamber pressure could be tested to gauge the feasibility of more effective cleaning of the mirrors that can't otherwise be efficiently reached by RF generated plasma.

Currently, new open calls for experiments, offering the beam-time of L1 Allegra system, are being published. As the number of L1 Allegra system operation hours doubles every year since 2019, so grows the number of published results using the L1 Allegra for driving secondary sources of radiation. The laser system has also been used for laser wakefield electron acceleration experiments [121]. The L1 Allegra keeps proving to be an invaluable laser for fundamental research and I am convinced the efforts with development and continuous improvements of pump lasers for the last few OPCPA stages will eventually enable to exploit their full potential and allow the L1 Allegra OPCPA stages to reach its designed output energy of 100 mJ at 15 fs.

References

[1] Hughes Research Laboratories, *The first laser*, https://www.hrl.com/about/laser, Accessed: 20.9.2021.

[2] D. Strickland and G. Mourou, "Compression of amplified chirped optical pulses," *Optics Communications*, vol. 55, no. 6, pp. 447–449, 1985. DOI: 10.1016/0030-4018(85)90151-8.

[3] M. D. Perry, D. Pennington, B. C. Stuart, G. Tietbohl, J. A. Britten, C. Brown, S. Herman, B. Golick, M. Kartz, J. Miller, H. T. Powell, M. Vergino, and V. Yanovsky, "Petawatt laser pulses," *Opt. Lett.*, vol. 24, no. 3, pp. 160–162, Feb. 1999. DOI: 10.1364/OL.24.000160.

[4] C. N. Danson, C. Haefner, J. Bromage, T. Butcher, J.-C. F. Chanteloup, E. A. Chowdhury, A. Galvanauskas, L. A. Gizzi, J. Hein, D. I. Hillier, and et al., "Petawatt and exawatt class lasers worldwide," *High Power Laser Science and Engineering*, vol. 7, e54, 2019. DOI: 10.1017/hpl.2019.36.

[5] T. Fuji, A. Unterhuber, V. Yakovlev, G. Tempea, A. Stingl, F. Krausz, and W. Drexler, "Generation of smooth, ultra-broadband spectra directly from a prism-less Ti:sapphire laser," *Applied Physics B*, vol. 77, pp. 125–128, Aug. 2003. DOI: 10.1007/s00340-003-1254-z.

[6] C. Spielmann, P. Curley, T. Brabec, and F. Krausz, "Ultrabroadband femtosecond lasers," *IEEE Journal of Quantum Electronics*, vol. 30, no. 4, pp. 1100–1114, 1994. DOI: 10.1109/3.291379.

[7] S. Fourmaux, S. Payeur, S. Buffechoux, P. Lassonde, C. St-Pierre, F. Martin, and J. C. Kieffer, "Pedestal cleaning for high laser pulse contrast ratio with a 100 TW class laser system," *Opt. Express*, vol. 19, no. 9, pp. 8486–8497, Apr. 2011. DOI: 10.1364/OE.19.008486.

[8] EKSPLA, *High Energy Temporaly Shaped Nanosecond Nd:YAG Lasers*, https://ekspla.com/product/nl940-series-high-energy-narrow-band-arbitrary-temporary-shaped-nanosecond-ndyag-lasers, Accessed: 5.1.2022.

[9] Thales, *Flash Lamp Solutions*, https://www.thalesgroup.com/en/worldwide/group/market-specific-solutions-lasers-science-applications/lpss-lasers-science, Accessed: 5.1.2022.

[10] K. Nakamura, H.-S. Mao, A. J. Gonsalves, H. Vincenti, D. E. Mittelberger, J. Daniels, A. Magana, C. Toth, and W. P. Leemans, "Diagnostics, control and performance parameters for the BELLA high repetition rate petawatt class laser," *IEEE Journal of Quantum Electronics*, vol. 53, no. 4, pp. 1–21, 2017. DOI: 10.1109/JQE.2017.2708601.

[11] S. Kühn, M. Dumergue, S. Kahaly, *et al.*, "The ELI-ALPS facility: The next generation of attosecond sources," *Journal of Physics B: Atomic, Molecular and Optical Physics*, vol. 50, no. 13, p. 132 002, Jun. 2017. DOI: 10.1088/1361-6455/aa6ee8.

[12] F. Batysta, R. Antipenkov, T. Borger, A. Kissinger, J. T. Green, R. Kananavičius, G. Chériaux, D. Hidinger, J. Kolenda, E. Gaul, B. Rus, and T. Ditmire, "Spectral pulse shaping of a 5 Hz, multi-joule, broadband optical parametric chirped pulse amplification frontend for a 10 PW laser system," *Opt. Lett.*, vol. 43, no. 16, pp. 3866–3869, Aug. 2018. DOI: 10.1364/OL.43.003866.

[13] F. Lureau, G. Matras, O. Chalus, C. Derycke, T. Morbieu, C. Radier, O. Casagrande, S. Laux, S. Ricaud, G. Rey, and et al., "High-energy hybrid femtosecond laser system demonstrating 2 × 10 PW capability," *High Power Laser Science and Engineering*, vol. 8, e43, 2020. DOI: 10.1017/hpl.2020.41.

[14] C. L. Haefner, "High average power, scalable, all diode-pumped solid state petawatt laser system HAPLS: A robust driver for high intensity laser matter interactions enabling precision

science and commercial applications," *The Review of Laser Engineering*, vol. 46, no. 3, p. 138, 2018. DOI: 10.2184/lsj.46.3_138.

[15] A. Dubietis, G. Jonušauskas, and A. Piskarskas, "Powerful fs pulse generation by chirped and stretched pulse parametric amplification in BBO crystal," *Optics Communications*, vol. 88, no. 4, pp. 437–440, 1992. DOI: 10.1016/0030-4018(92)90070-8.

[16] S. E. Harris, M. K. Oshman, and R. L. Byer, "Observation of tunable optical parametric fluorescence," *Phys. Rev. Lett.*, vol. 18, pp. 732–734, 18 May 1967. DOI: 10.1103/PhysRevLett.18.732.

[17] I. Ross, P. Matousek, M. Towrie, A. Langley, and J. Collier, "The prospects for ultrashort pulse duration and ultrahigh intensity using optical parametric chirped pulse amplifiers," *Optics Communications*, vol. 144, no. 1, pp. 125–133, 1997. DOI: 10.1016/S0030-4018(97)00399-4.

[18] J. Moses, C. Manzoni, S.-W. Huang, G. Cerullo, and F. X. Kärtner, "Temporal optimization of ultrabroadband high-energy OPCPA," *Opt. Express*, vol. 17, no. 7, pp. 5540–5555, Mar. 2009. DOI: 10.1364/OE.17.005540.

[19] A. Kessel, V. E. Leshchenko, O. Jahn, M. Krüger, A. Münzer, A. Schwarz, V. Pervak, M. Trubetskov, S. A. Trushin, F. Krausz, Z. Major, and S. Karsch, "Relativistic few-cycle pulses with high contrast from picosecond-pumped OPCPA," *Optica*, vol. 5, no. 4, pp. 434–442, Apr. 2018. DOI: 10.1364/OPTICA.5.000434.

[20] W. Krupke, "Ytterbium solid-state lasers. The first decade," *Selected Topics in Quantum Electronics, IEEE Journal of*, vol. 6, pp. 1287–1296, Dec. 2000. DOI: 10.1109/2944.902180.

[21] M. Müller, C. Aleshire, A. Klenke, E. Haddad, F. Légaré, A. Tünnermann, and J. Limpert, "10.4 kW coherently combined ultrafast fiber laser," *Opt. Lett.*, vol. 45, no. 11, pp. 3083–3086, Jun. 2020. DOI: 10.1364/OL.392843.

[22] A. Klenke, E. Seise, S. Demmler, J. Rothhardt, S. Breitkopf, J. Limpert, and A. Tünnermann, "Coherently-combined two channel femtosecond fiber CPA system producing 3 mJ pulse energy," *Opt. Express*, vol. 19, no. 24, pp. 24 280–24 285, Nov. 2011. DOI: 10.1364/OE.19.024280.

[23] P. Russbueldt, D. Hoffmann, M. Höfer, J. Löhring, J. Luttmann, A. Meissner, J. Weitenberg, M. Traub, T. Sartorius, D. Esser, R. Wester, P. Loosen, and R. Poprawe, "Innoslab amplifiers," *IEEE Journal of Selected Topics in Quantum Electronics*, vol. 21, no. 1, pp. 447–463, 2015. DOI: 10.1109/JSTQE.2014.2333234.

[24] M. Schulz, R. Riedel, A. Willner, T. Mans, C. Schnitzler, P. Russbueldt, J. Dolkemeyer, E. Seise, T. Gottschall, S. Hädrich, S. Duesterer, H. Schlarb, J. Feldhaus, J. Limpert, B. Faatz, A. Tünnermann, J. Rossbach, M. Drescher, and F. Tavella, "Yb:YAG Innoslab amplifier: efficient high repetition rate subpicosecond pumping system for optical parametric chirped pulse amplification," *Opt. Lett.*, vol. 36, no. 13, pp. 2456–2458, Jul. 2011. DOI: 10.1364/OL.36.002456.

[25] R. L. Aggarwal, D. J. Ripin, J. R. Ochoa, and T. Y. Fan, "Measurement of thermo-optic properties of $Y_3Al_5O_{12}$, $Lu_3Al_5O_{12}$, $YAlO_3$, $LiYF_4$, $LiLuF_4$, BaY_2F_8, $KGd(WO_4)_2$, and $KY(WO_4)_2$ laser crystals in the 80 – 300 K temperature range," *Journal of Applied Physics*, vol. 98, no. 10, p. 103 514, 2005. DOI: 10.1063/1.2128696.

[26] C. Baumgarten, M. Pedicone, H. Bravo, H. Wang, L. Yin, C. Menoni, J. Rocca, and B. Reagan, "A 1 Joule, 0.5 kHz repetition rate picosecond laser," *Opt. Lett.*, Jun. 2016. DOI: 10.1364/OL.41.003339.

[27] C. Herkommer, P. Krötz, R. Jung, S. Klingebiel, C. Wandt, R. Bessing, P. Walch, T. Produit, K. Michel, D. Bauer, R. Kienberger, and T. Metzger, "Ultrafast thin-disk multipass amplifier

with 720 mJ operating at kilohertz repetition rate for applications in atmospheric research," *Opt. Express*, vol. 28, no. 20, pp. 30 164–30 173, Sep. 2020. DOI: 10.1364/OE.404185.

[28] J.-P. Negel, A. Loescher, A. Voss, D. Bauer, D. Sutter, A. Killi, M. A. Ahmed, and T. Graf, "Ultrafast thin-disk multipass laser amplifier delivering 1.4 kW (4.7 mJ, 1030 nm) average power converted to 820 W at 515 nm and 234 W at 343 nm," *Opt. Express*, vol. 23, no. 16, pp. 21 064–21 077, Aug. 2015. DOI: 10.1364/OE.23.021064.

[29] A. Suemasa, A. Shimo-oku, S. Ohtsuka, M. Nakamori, and M. Musha, "Stable and high power 515-nm lasers for the space gravitational wave detector: DECIGO," in *International Conference on Space Optics – ICSO 2018*, Z. Sodnik, N. Karafolas, and B. Cugny, Eds., International Society for Optics and Photonics, vol. 11180, SPIE, 2019, pp. 337–343. DOI: 10.1117/12.2535950.

[30] O. B. Jensen, A. K. Hansen, A. Müller, B. Sumpf, P. M. Petersen, and P. E. Andersen, "Efficient generation of 3.5 W laser light at 515 nm by frequency doubling a single-frequency high power DBR tapered diode laser," *Optics Communications*, vol. 392, pp. 167–170, 2017. DOI: 10.1016/j.optcom.2017.01.060.

[31] Q. Liu, M. Yang, Y. Yao, L. Zhao, B. Li, D. Qu, and Q. Zheng, "All-solid-state low noise Yb:YAG/LBO green laser at 515 nm," *Optics and Spectroscopy*, vol. 115, Jul. 2013. DOI: 10.1134/S0030400X13070151.

[32] X. Guo, W. Hou, H. Peng, H. Zhang, G. Wang, Y. Bi, A. Geng, Y. Chen, D. Cui, and Z. Xu, "4.44 W of CW 515 nm green light generated by intracavity frequency doubling Yb:YAG thin disk laser with LBO," *Optics Communications*, vol. 267, no. 2, pp. 451–454, 2006. DOI: 10.1016/j.optcom.2006.06.086.

[33] B. Gronloh, P. Russbueldt, B. Jungbluth, and H.-D. Hoffmann, "Green sub-ps laser exceeding 400 W of average power," in *Solid State Lasers XXIII: Technology and Devices*, W. A. Clarkson and R. K. Shori, Eds., International Society for Optics and Photonics, vol. 8959, SPIE, 2014, pp. 146–155. DOI: 10.1117/12.2041288.

[34] J. Vengelis, I. Stasevičius, K. Stankevičiūtė, V. Jarutis, R. Grigonis, M. Vengris, and V. Sirutkaitis, "Characteristics of optical parametric oscillators synchronously pumped by second harmonic of femtosecond Yb:KGW laser," *Optics Communications*, vol. 338, pp. 277–287, 2015. DOI: 10.1016/j.optcom.2014.10.054.

[35] D. Descamps, F. Guichard, S. Petit, S. Beauvarlet, A. Comby, L. Lavenu, and Y. Zaouter, "High-power sub-15 fs nonlinear pulse compression at 515 nm of an ultrafast Yb-doped fiber amplifier," *Opt. Lett.*, vol. 46, no. 8, pp. 1804–1807, Apr. 2021. DOI: 10.1364/OL.419683.

[36] C. Aparajit, K. Jana, A. D. Lad, Y. M. Ved, A. Couairon, and G. R. Kumar, "Efficient second-harmonic generation of a high-energy, femtosecond laser pulse in a lithium triborate crystal," *Opt. Lett.*, vol. 46, no. 15, pp. 3540–3543, Aug. 2021. DOI: 10.1364/OL.423725.

[37] M. Duda, O. Novák, M. Chyla, M. Smrž, and T. Mocek, "Balancing the conversion efficiency and beam quality of second harmonic generation of a two-picosecond Yb:YAG thin-disk laser," vol. 30, no. 2, p. 025 405, Jan. 2020. DOI: 10.1088/1555-6611/ab60b0.

[38] P. Mackonis and A. M. Rodin, "Laser with 1.2 ps, 20 mJ pulses at 100 Hz based on CPA with a low doping level Yb:YAG rods for seeding and pumping of OPCPA," *Opt. Express*, vol. 28, no. 2, pp. 1261–1268, Jan. 2020. DOI: 10.1364/OE.380907.

[39] K. Mecseki, M. K. R. Windeler, A. Miahnahri, J. S. Robinson, J. M. Fraser, A. R. Fry, and F. Tavella, "High average power 88 W OPCPA system for high-repetition-rate experiments at the LCLS X-ray free-electron laser," *Opt. Lett.*, vol. 44, no. 5, pp. 1257–1260, Mar. 2019. DOI: 10.1364/OL.44.001257.

[40] H. Fattahi, A. Alismail, H. Wang, J. Brons, O. Pronin, T. Buberl, L. Vámos, G. Arisholm, A. M. Azzeer, and F. Krausz, "High-power, 1-ps, all-Yb:YAG thin-disk regenerative amplifier," *Opt. Lett.*, vol. 41, no. 6, pp. 1126–1129, Mar. 2016. DOI: 10.1364/OL.41.001126.

[41] F. Zou, Z. Wang, Z. Wang, Y. Bai, Q. Li, and J. Zhou, "1-MW peak power, 574-kHz repetition rate picosecond pulses at 515 nm from a frequency-doubled fiber amplifier," in *High-Power Lasers and Applications VIII*, R. Li, U. N. Singh, and R. F. Walter, Eds., International Society for Optics and Photonics, vol. 10016, SPIE, 2016, pp. 81–87. DOI: 10.1117/12.2245577.

[42] F. Harth, M. C. Piontek, T. Herrmann, and J. A. L'huillier, "Ultrafast laser with an average power of 120 W at 515 nm and a highly dynamic repetition rate in the MHz range for novel applications in micromachining," in *Solid State Lasers XXV: Technology and Devices*, W. A. Clarkson and R. K. Shori, Eds., International Society for Optics and Photonics, vol. 9726, SPIE, 2016, pp. 190–199. DOI: 10.1117/12.2212919.

[43] C. Rothhardt, J. Rothhardt, A. Klenke, T. Peschel, R. Eberhardt, J. Limpert, and A. Tünnermann, "BBO-sapphire sandwich structure for frequency conversion of high power lasers," *Opt. Mater. Express*, vol. 4, no. 5, pp. 1092–1103, May 2014. DOI: 10.1364/OME.4.001092.

[44] R. Budriūnas, T. Stanislauskas, J. Adamonis, A. Aleknavičius, G. Veitas, D. Gadonas, S. Balickas, A. Michailovas, and A. Varanavičius, "53 W average power CEP-stabilized OPCPA system delivering 5.5 TW few cycle pulses at 1 kHz repetition rate," *Opt. Express*, vol. 25, no. 5, pp. 5797–5806, Apr. 2017. DOI: 10.1364/OE.25.005797.

[45] J. P. Phillips, S. Banerjee, P. Mason, J. Smith, J. Spear, M. D. Vido, K. Ertel, T. Butcher, G. Quinn, D. Clarke, C. Edwards, C. Hernandez-Gomez, and J. Collier, "Second and third harmonic conversion of a kilowatt average power, 100-J-level diode pumped Yb:YAG laser in large aperture LBO," *Opt. Lett.*, vol. 46, no. 8, pp. 1808–1811, Apr. 2021. DOI: 10.1364/OL.419861.

[46] H. Chi, Y. Wang, A. Davenport, C. S. Menoni, and J. J. Rocca, "Demonstration of a kilowatt average power, 1 J, green laser," *Opt. Lett.*, vol. 45, no. 24, pp. 6803–6806, Dec. 2020. DOI: 10.1364/OL.412975.

[47] A. Bayramian, R. Bopp, B. Deri, *et al.*, "High-energy diode-pumped solid-state laser (DPSSL) for high-repetition-rate petawatt laser systems," in *High-Brightness Sources and Light-Driven Interactions*, Optical Society of America, 2016, HT1B.5. DOI: 10.1364/HILAS.2016.HT1B.5.

[48] J. P. Phillips, S. Banerjee, J. Smith, M. Fitton, T. Davenne, K. Ertel, P. Mason, T. Butcher, M. D. Vido, J. Greenhalgh, C. Edwards, C. Hernandez-Gomez, and J. Collier, "High energy, high repetition rate, second harmonic generation in large aperture DKDP, YCOB, and LBO crystals," *Opt. Express*, vol. 24, no. 17, pp. 19 682–19 694, Aug. 2016. DOI: 10.1364/OE.24.019682.

[49] T. Sekine, H. Sakai, Y. Takeuchi, Y. Hatano, T. Kawashima, H. Kan, J. Kawanaka, N. Miyanaga, and T. Norimatsu, "High efficiency 12.5 J second-harmonic generation from $CsLiB_6O_{10}$ nonlinear crystal by diode-pumped Nd:glass laser," *Opt. Express*, vol. 21, no. 7, pp. 8393–8400, Apr. 2013. DOI: 10.1364/OE.21.008393.

[50] C. L. Haefner, A. Bayramian, S. Betts, *et al.*, "High average power, diode pumped petawatt laser systems: A new generation of lasers enabling precision science and commercial applications," *Proc. SPIE*, vol. 10241, p. 1 024 102, 2017. DOI: 10.1117/12.2281050.

[51] R. Antipenkov, F. Batysta, R. Boge, *et al.*, "The construction of Allegra kilohertz femtosecond laser system at ELI-Beamlines," *Proc. SPIE*, vol. 11034, p. 110340M, 2019. DOI: 10.1117/12.2524436.

[52] J. Nejdl, D.-D. Mai, U. Chaulagain, *et al.*, "Progress on laser-driven X-ray sources at ELI Beamlines," *Proc. SPIE*, vol. 11111, p. 111110I, 2019. DOI: 10.1117/12.2532702.

[53] O. Hort, M. Albrecht, V. E. Nefedova, O. Finke, D. D. Mai, S. Reyné, F. Giambruno, F. Frassetto, L. Poletto, J. Andreasson, J. Gautier, S. Sebban, and J. Nejdl, "High-flux source of coherent XUV pulses for user applications," *Opt. Express*, vol. 27, no. 6, pp. 8871–8883, Apr. 2019. DOI: 10.1364/OE.27.008871.

[54] J. Novák, "Diode pumped thin disk lasers for high repetition rate picosecond OPCPA pumping," Ph.D. dissertation, FNSPE CTU in Prague, 2016.

[55] P. A. Franken, A. E. Hill, C. W. Peters, and G. Weinreich, "Generation of optical harmonics," *Phys. Rev. Lett.*, vol. 7, pp. 118–119, 4 Aug. 1961. DOI: 10.1103/PhysRevLett.7.118.

[56] A. Lattes, H. Haus, F. Leonberger, and E. Ippen, "An ultrafast all-optical gate," *IEEE Journal of Quantum Electronics*, vol. 19, no. 11, pp. 1718–1723, 1983. DOI: 10.1109/JQE.1983.1071766.

[57] D. E. Spence, P. N. Kean, and W. Sibbett, "60-fsec pulse generation from a self-mode-locked Ti:sapphire laser," *Opt. Lett.*, vol. 16, no. 1, pp. 42–44, Jan. 1991. DOI: 10.1364/OL.16.000042.

[58] D. J. Jones, S. A. Diddams, M. S. Taubman, S. T. Cundiff, L.-S. Ma, and J. L. Hall, "Frequency comb generation using femtosecond pulses and cross-phase modulation in optical fiber at arbitrary center frequencies," *Opt. Lett.*, vol. 25, no. 5, pp. 308–310, Mar. 2000. DOI: 10.1364/OL.25.000308.

[59] E. Garmire, "Nonlinear optics in daily life," *Opt. Express*, vol. 21, no. 25, pp. 30 532–30 544, Dec. 2013. DOI: 10.1364/OE.21.030532.

[60] U. L. Österberg, "Nonlinear optics: Theory and applications," in *Trends in Optical Fibre Metrology and Standards*, O. D. D. Soares, Ed. Dordrecht: Springer Netherlands, 1995, pp. 711–725. DOI: 10.1007/978-94-011-0035-9_35.

[61] R. W. Boyd, *Nonlinear Optics, Third Edition*, 3rd. USA: Academic Press, Inc., 2008.

[62] S. Zahedpour, J. Wahlstrand, and H. Milchberg, "Measurement of the nonlinear refractive index of air constituents at mid-infrared wavelengths," *Optics Letters*, vol. 40, Sep. 2015. DOI: 10.1364/OL.40.005794.

[63] V. Fedorov and V. Kandidov, "A nonlinear optical model of an air medium in the problem of filamentation of femtosecond laser pulses of different wavelengths," *Optics and Spectroscopy*, vol. 105, pp. 280–287, Aug. 2008. DOI: 10.1134/S0030400X08080183.

[64] U. Roth, F. Loewenthal, R. Tommasini, J. Balmer, and H. Weber, "Compensation of nonlinear self-focusing in high-power lasers," *IEEE Journal of Quantum Electronics*, vol. 36, no. 6, pp. 687–691, 2000. DOI: 10.1109/3.845724.

[65] K. Beckwitt, F. W. Wise, L. Qian, L. A. Walker, and E. Canto-Said, "Compensation for self-focusing by use of cascade quadratic nonlinearity," *Opt. Lett.*, vol. 26, no. 21, pp. 1696–1698, Nov. 2001. DOI: 10.1364/OL.26.001696.

[66] R. DeSalvo, D. J. Hagan, M. Sheik-Bahae, G. Stegeman, E. W. V. Stryland, and H. Vanherzeele, "Self-focusing and self-defocusing by cascaded second-order effects in KTP," *Opt. Lett.*, vol. 17, no. 1, pp. 28–30, Jan. 1992. DOI: 10.1364/OL.17.000028.

[67] Rüdiger Paschotta, *RP Photonics Encyclopedia*, https://www.rp-photonics.com/, Accessed: 30.9.2021.

[68] C. V. Shank, R. L. Fork, R. Yen, R. H. Stolen, and W. J. Tomlinson, "Compression of femtosecond optical pulses," *Applied Physics Letters*, vol. 40, no. 9, pp. 761–763, 1982. DOI: 10.1063/1.93276.

[69] M. Nisoli, S. D. Silvestri, O. Svelto, R. Szipöcs, K. Ferencz, C. Spielmann, S. Sartania, and F. Krausz, "Compression of high-energy laser pulses below 5 fs," *Opt. Lett.*, vol. 22, no. 8, pp. 522–524, Apr. 1997. DOI: 10.1364/OL.22.000522.

[70] R. R. Alfano and S. L. Shapiro, "Observation of self-phase modulation and small-scale filaments in crystals and glasses," *Phys. Rev. Lett.*, vol. 24, pp. 592–594, 11 Mar. 1970. DOI: 10.1103/PhysRevLett.24.592.

[71] J. Darginavičius, D. Majus, V. Jukna, N. Garejev, G. Valiulis, A. Couairon, and A. Dubietis, "Ultrabroadband supercontinuum and third-harmonic generation in bulk solids with two optical-cycle carrier-envelope phase-stable pulses at 2 μm," *Opt. Express*, vol. 21, no. 21, pp. 25 210–25 220, Oct. 2013. DOI: 10.1364/OE.21.025210.

[72] F. Silva, D. Austin, A. Thai, M. Baudisch, M. Hemmer, D. Faccio, A. Couairon, and J. Biegert, "Multi-octave supercontinuum generation from mid-infrared filamentation in a bulk crystal," *Nature communications*, vol. 3, p. 807, May 2012. DOI: 10.1038/ncomms1816.

[73] L. Indra, F. Batysta, P. Hříbek, J. Novák, Z. Hubka, J. T. Green, R. Antipenkov, R. Boge, J. A. Naylon, P. Bakule, and B. Rus, "Picosecond pulse generated supercontinuum as a stable seed for OPCPA," *Opt. Lett.*, vol. 42, no. 4, pp. 843–846, Feb. 2017. DOI: 10.1364/OL.42.000843.

[74] H. Wang, A. Alismail, G. Barbiero, M. Wendl, and H. Fattahi, "Cross-polarized, multi-octave supercontinuum generation," *Opt. Lett.*, vol. 42, no. 13, pp. 2595–2598, Jul. 2017. DOI: 10.1364/OL.42.002595.

[75] A. V. Smith, *SNLO classic*, https://as-photonics.com/products/snlo/, Accessed: 20.9.2021.

[76] J. E. Midwinter and J. Warner, "The effects of phase matching method and of uniaxial crystal symmetry on the polar distribution of second-order non-linear optical polarization," *British Journal of Applied Physics*, vol. 16, no. 8, pp. 1135–1142, Aug. 1965. DOI: 10.1088/0508-3443/16/8/312.

[77] R. M. Waxler and G. W. Cleek, "The effect of temperature and pressure on the refractive index of some oxide glasses," *Journal of research of the National Bureau of Standards. Section A, Physics and chemistry*, vol. 77A,6, pp. 755–763, 1973. DOI: 10.6028/jres.077A.046.

[78] Y. Shen, "Self-focusing: Experimental," *Progress in Quantum Electronics*, vol. 4, pp. 1–34, 1975. DOI: 10.1016/0079-6727(75)90002-6.

[79] K. Kato, "Temperature-tuned 90 deg phase-matching properties of LiB_3O_5," *IEEE Journal of Quantum Electronics*, vol. 30, no. 12, pp. 2950–2952, 1994. DOI: 10.1109/3.362711.

[80] I. Walmsley, L. Waxer, and C. Dorrer, "The role of dispersion in ultrafast optics," *Review of Scientific Instruments*, vol. 72, no. 1, pp. 1–29, 2001. DOI: 10.1063/1.1330575.

[81] R. L. Fork, C. H. B. Cruz, P. C. Becker, and C. V. Shank, "Compression of optical pulses to six femtoseconds by using cubic phase compensation," *Opt. Lett.*, vol. 12, no. 7, pp. 483–485, Jul. 1987. DOI: 10.1364/OL.12.000483.

[82] E. Treacy, "Optical pulse compression with diffraction gratings," *IEEE Journal of Quantum Electronics*, vol. 5, no. 9, pp. 454–458, 1969. DOI: 10.1109/JQE.1969.1076303.

[83] Y. Arosa and R. de la Fuente, "Refractive index spectroscopy and material dispersion in fused silica glass," *Opt. Lett.*, vol. 45, no. 15, pp. 4268–4271, Aug. 2020. DOI: 10.1364/OL.395510.

[84] S. Luan, M. H. R. Hutchinson, R. A. Smith, and F. Zhou, "High dynamic range third-order correlation measurement of picosecond laser pulse shapes," *Measurement Science and Technology*, vol. 4, no. 12, pp. 1426–1429, Dec. 1993. DOI: 10.1088/0957-0233/4/12/018.

[85] K. W. DeLong, R. Trebino, J. Hunter, and W. E. White, "Frequency-resolved optical gating with the use of second-harmonic generation," *J. Opt. Soc. Am. B*, vol. 11, no. 11, pp. 2206–2215, Nov. 1994. DOI: 10.1364/JOSAB.11.002206.

[86] A. Giesen, H. Hügel, A. Voss, K. Wittig, U. Brauch, and H. Opower, "Scalable concept for diode-pumped high-power solid-state lasers," *Applied Physics B*, vol. 58, pp. 365–372, 1994. DOI: 10.1007/BF01081875.

[87] M. Eichhorn, "Quasi-three-level solid-state lasers in the near and mid infrared," in *CLEO/Europe and EQEC 2011 Conference Digest*, Optical Society of America, 2011, CA3–5.

[88] R. C. Powell, *Physics of Solid-State Laser Materials*. New York: Springer-Verlag, 1998.

[89] J. Koerner, V. Jambunathan, J. Hein, R. Seifert, M. Loeser, M. Siebold, U. Schramm, P. Sikocinski, A. Lucianetti, J. Nejdl, and M. Kaluza, "Spectroscopic characterization of Yb^{3+}-doped laser materials at cryogenic temperatures," *Applied Physics B: Lasers and Optics*, vol. 116, pp. 415–, Sep. 2013. DOI: 10.1007/s00340-013-5650-8.

[90] Z. Hubka, "Infrared solid-state lasers operating at low temperatures," M.S. thesis, FNSPE, CTU in Prague, May 2014.

[91] N. Vretenar, T. Carson, T. C. Newell, T. Lucas, W. P. Latham, and P. Peterson, "Yb:YAG thin-disk laser performance at room and cryogenic temperatures," in *Solid State Lasers XXI: Technology and Devices*, W. A. Clarkson and R. K. Shori, Eds., International Society for Optics and Photonics, vol. 8235, SPIE, 2012, pp. 120–127. DOI: 10.1117/12.924302.

[92] A. E. Siegman, "Pulse broadening and gain dispersion," in *Lasers,* University Science Books, CA, 1986, ch. 9.5, p. 359.

[93] D. Kokkinos, H. Schröder, K. Fleury-Frenette, M. Georges, W. Riede, G. Tzeremes, and P. Rochus, "Laser optics in space failure risk due to laser induced contamination," *CEAS Space Journal*, vol. 9, Aug. 2016. DOI: 10.1007/s12567-016-0137-1.

[94] LIGO document control center, *E080177-v2: RGA test qualification of components for the LIGO UHV*, https://dcc.ligo.org/LIGO-E080177/public, Accessed: 26.08.2021.

[95] Hidden Analytical, *Tech data, cracking patterns*, https://www.hidenanalytical.com/tech-data/cracking-patterns/, Accessed: 28.09.2021.

[96] F. Batysta, R. Antipenkov, J. T. Green, J. A. Naylon, J. Novák, T. Mazanec, P. Hříbek, C. Zervos, P. Bakule, and B. Rus, "Pulse synchronization system for picosecond pulse-pumped OPCPA with femtosecond-level relative timing jitter," *Opt. Express*, vol. 22, no. 24, pp. 30 281–30 286, Dec. 2014. DOI: 10.1364/OE.22.030281.

[97] M. Horáček, L. Indra, J. T. Green, J. A. Naylon, B. Tykalewicz, J. Novák, F. Batysta, T. Mazanec, J. Horáček, R. Antipenkov, Z. Hubka, R. Boge, P. Bakule, and B. Rus, "Multi-channel, fiber-based seed pulse distribution system for femtosecond-level synchronized chirped pulse amplifiers," *Review of Scientific Instruments*, vol. 88, no. 1, p. 013 109, 2017. DOI: 10.1063/1.4974272.

[98] TRUMPF Scientific lasers, *DIRA series*, https://www.trumpf-scientific-lasers.com/products/dira-series/, Accessed: 20.9.2021.

[99] T. Metzger, "High-repetition-rate picosecond pump laser based on an Yb:YAG disk amplifier for optical parametric amplification," Ph.D. dissertation, Technical University Berlin, 2009.

[100] J. Mužík, "Development of high-repetition-rate picosecond thin-disk lasers," Ph.D. dissertation, FNSPE CTU in Prague, 2021.

[101] O. Schreiber, *Eli ytterbium-doped fiber amplifier model,* version 1.0, Oct. 15, 2021.

[102] A. Špaček, J. T. Green, F. Batysta, J. Novák, R. Antipenkov, P. Bakule, and B. Rus, "General method of passive optical pulse peak intensity stabilization through controlled self-phase modulation and over-compression," *J. Opt. Soc. Am. B*, vol. 35, no. 10, pp. 2494–2500, Oct. 2018. DOI: 10.1364/JOSAB.35.002494.

[103] Y. Painchaud, C. Paquet, and M. Guy, "Optical tunable dispersion compensators based on thermally tuned fiber Bragg gratings," *Opt. Photon. News*, vol. 18, no. 9, pp. 48–53, Sep. 2007. DOI: 10.1364/OPN.18.9.000048.

[104] Cristal laser, *LBO crystals*, https://www.cristal-laser.com/products/non-linear-optics/lbo-crystal.html, Accessed: 20.9.2021.

[105] M. P. Kalashnikov, E. Risse, H. Schönnagel, and W. Sandner, "Double chirped-pulse-amplification laser: A way to clean pulses temporally," *Opt. Lett.*, vol. 30, no. 8, pp. 923–925, Apr. 2005. DOI: 10.1364/OL.30.000923.

[106] M. Iliev, A. K. Meier, M. Greco, and C. G. Durfee, "Nonlinear dynamics of double-pass cross-polarized wave generation in the saturation regime," *Appl. Opt.*, vol. 54, no. 2, pp. 219–227, Jan. 2015. DOI: 10.1364/AO.54.000219.

[107] N. Minkovski, G. I. Petrov, S. M. Saltiel, O. Albert, and J. Etchepare, "Nonlinear polarization rotation and orthogonal polarization generation experienced in a single-beam configuration," *J. Opt. Soc. Am. B*, vol. 21, no. 9, pp. 1659–1664, Sep. 2004. DOI: 10.1364/JOSAB.21.001659.

[108] M. Hornung, H. Liebetrau, A. Seidel, S. Keppler, A. Kessler, J. Körner, M. Hellwing, F. Schorcht, D. Klöpfel, A. K. Arunachalam, and et al., "The all-diode-pumped laser system polaris – an experimentalist's tool generating ultra-high contrast pulses with high energy," *High Power Laser Science and Engineering*, vol. 2, e20, 2014. DOI: 10.1017/hpl.2014.26.

[109] Z. Hubka, J. Novák, I. Majerová, J. T. Green, P. K. Velpula, R. Boge, R. Antipenkov, V. Šobr, D. Kramer, K. Majer, J. A. Naylon, P. Bakule, and B. Rus, "Mitigation of laser-induced contamination in vacuum in high-repetition-rate high-peak-power laser systems," *Appl. Opt.*, vol. 60, no. 3, pp. 533–538, Jan. 2021. DOI: 10.1364/AO.414878.

[110] Z. Hubka, R. Antipenkov, R. Boge, E. Erdman, M. Greco, J. T. Green, M. Horáček, K. Majer, T. Mazanec, P. Mazůrek, J. A. Naylon, J. Novák, V. Šobr, P. Strkula, M. Torun, B. Tykalewicz, P. Bakule, and B. Rus, "120 mJ, 1 kHz, picosecond laser at 515 nm," *Opt. Lett.*, vol. 46, no. 22, pp. 5655–5658, Nov. 2021. DOI: 10.1364/OL.440448.

[111] Ansys®, *Workbench*, version 19.1.

[112] Newlight Photonics Inc., *LBO properties*, http://www.newlightphotonics.com/v1/lbo-properties.html, Accessed: 20.9.2021.

[113] Engineering ToolBox, https://www.engineeringtoolbox.com/, Accessed: 20.9.2021.

[114] ASM Aerospace Specifications Metals, Inc., *Aluminum 5083-O*, http://asm.matweb.com/search/SpecificMaterial.asp?bassnum=MA5083O, Accessed: 20.9.2021.

[115] S. G. Grechin, A. V. Zuev, A. E. Kokh, N. V. Moiseev, P. A. Popov, A. A. Sidorov, and A. S. Fokin, "Thermophysical parameters of the LBO crystal," *Quantum Electronics*, vol. 40, no. 6, pp. 509–512, Aug. 2010. DOI: 10.1070/qe2010v040n06abeh014312.

[116] Technology Applications, Inc., *Spaceflight Model Thermal Straps*, https://www.techapps.com/copper-thermal-strap-gallery-spaceflight-models, Accessed: 20.9.2021.

[117] C. L. Choy, K. W. Kwok, W. P. Leung, and F. P. Lau, "Thermal conductivity of poly(ether ether ketone) and its short-fiber composites," *Journal of Polymer Science Part B: Polymer Physics*, vol. 32, no. 8, pp. 1389–1397, 1994. DOI: 10.1002/polb.1994.090320810.

[118] Northrop Grumman, *Faraday crystals*, https://www.northropgrumman.com/space/synoptics-products-faraday-crystals/, Accessed: 20.9.2021.

[119] EOT Electro-optics Technology, Inc., *PAVOS Ultra High Power Optical Isolators - 1010 nm to 1080 nm*, https://www.eotech.com/cart/category30/faraday-rotators-and-isolators, Accessed: 20.9.2021.

[120] T. L. Bergman, A. S. Lavine, F. P. Incropera, and D. P. DeWitt, *Fundamentals of Heat and Mass Transfer*. New Jersey, USA: John Wiley & Sons, Inc., 2018.

[121] S. Lorenz, G. Grittani, E. Chacon-Golcher, C. M. Lazzarini, J. Limpouch, F. Nawaz, M. Nevrkla, L. Vilanova, and T. Levato, "Characterization of supersonic and subsonic gas targets for laser wakefield electron acceleration experiments," *Matter and Radiation at Extremes*, vol. 4, no. 1, p. 015 401, 2019. DOI: 10.1063/1.5081509.

Publications and conference proceedings

Papers

[1] **Hubka, Z.**, R. Antipenkov, R. Boge, E. Erdman, M. Greco, J. T. Green, M. Horáček, K. Majer, T. Mazanec, P. Mazůrek, J. A. Naylon, J. Novák, V. Šobr, P. Strkula, M. Torun, B. Tykalewicz, P. Bakule, and B. Rus, "120 mJ, 1 kHz, picosecond laser at 515 nm," *Opt. Lett.*, vol. 46, no. 22, pp. 5655–5658, Nov. 2021. DOI: 10.1364/OL.440448.

[2] **Hubka, Z.**, J. Novák, I. Majerová, J. T. Green, P. K. Velpula, R. Boge, R. Antipenkov, V. Šobr, D. Kramer, K. Majer, J. A. Naylon, P. Bakule, and B. Rus, "Mitigation of laser-induced contamination in vacuum in high-repetition-rate high-peak-power laser systems," *Appl. Opt.*, vol. 60, no. 3, pp. 533–538, Jan. 2021. DOI: 10.1364/AO.414878.

[3] M. Horáček, L. Indra, J. T. Green, J. A. Naylon, B. Tykalewicz, J. Novák, F. Batysta, T. Mazanec, J. Horáček, R. Antipenkov, **Hubka, Z.**, R. Boge, P. Bakule, and B. Rus, "Multi-channel, fiber-based seed pulse distribution system for femtosecond-level synchronized chirped pulse amplifiers," *Review of Scientific Instruments*, vol. 88, no. 1, p. 013 109, 2017. DOI: 10.1063/1.4974272.

[4] R. Boge, J. Horáček, P. Mazůrek, J. A. Naylon, J. T. Green, **Hubka, Z.**, V. Šobr, J. Novák, F. Batysta, R. Antipenkov, P. Bakule, and B. Rus, "Robust method for long-term energy and pointing stabilization of high energy, high average power solid state lasers," *Review of Scientific Instruments*, vol. 89, no. 2, p. 023 113, 2018. DOI: 10.1063/1.5018713.

[5] J. Novák, J. T. Green, T. Metzger, T. Mazanec, B. Himmel, M. Horáček, **Hubka, Z.**, R. Boge, R. Antipenkov, F. Batysta, J. A. Naylon, P. Bakule, and B. Rus, "Thin disk amplifier-based 40 mJ, 1 kHz, picosecond laser at 515 nm," *Opt. Express*, vol. 24, no. 6, pp. 5728–5733, Mar. 2016. DOI: 10.1364/OE.24.005728.

[6] F. Batysta, R. Antipenkov, J. Novák, J. T. Green, J. A. Naylon, J. Horáček, M. Horáček, **Hubka, Z.**, R. Boge, T. Mazanec, B. Himmel, P. Bakule, and B. Rus, "Broadband OPCPA system with 11 mJ output at 1 kHz, compressible to 12 fs," *Opt. Express*, vol. 24, no. 16, pp. 17 843–17 848, Aug. 2016. DOI: 10.1364/OE.24.017843.

[7] L. Indra, F. Batysta, P. Hříbek, J. Novák, **Hubka, Z.**, J. T. Green, R. Antipenkov, R. Boge, J. A. Naylon, P. Bakule, and B. Rus, "Picosecond pulse generated supercontinuum as a stable seed for OPCPA," *Opt. Lett.*, vol. 42, no. 4, pp. 843–846, Feb. 2017. DOI: 10.1364/OL.42.000843.

Selected Conferences

[8] **Hubka, Z.**, R. Antipenkov, R. Boge, A. Špaček, J. Novák, M. Horáček, P. Mazurek, K. Majer, B. Tykalewicz, M. Torun, J. T. Green, J. A. Naylon, P. Bakule, and B. Rus, "Optimization of pump lasers for high-energy OPCPA system," in *High Power Lasers and Applications*, J. Hein, T. J. Butcher, P. Bakule, C. L. Haefner, G. Korn, and L. O. Silva, Eds., International Society for Optics and Photonics, vol. 11777, SPIE, 2021, pp. 17–23.

[9] **Hubka, Z.**, R. Boge, F. Batysta, R. Antipenkov, J. Novak, M. Greco, E. Erdman, A. Spacek, L. Indra, K. Majer, J. T. Green, J. A. Naylon, P. Bakule, and B. Rus, "High energy, high average power, nonlinear frequency conversion and parametric amplification of picosecond pulses in vacuum," in *Nonlinear Optics (NLO)*, Optical Society of America, 2019, NTh2B.7. DOI: 10.1364/NLO.2019.NTh2B.7.

[10] **Hubka, Z.**, R. Boge, J. Novák, J. T. Green, M. Greco, R. Antipenkov, F. Batysta, V. Šobr, J. A. Naylon, P. Bakule, and B. Rus, "Picosecond thin-disk pump laser system for high energy OPCPA," in *Ultrafast Optics 2017*, International Society for Optics and Photonics, vol. 10606, SPIE, 2018, p. 93.

[13] R. Antipenkov, F. Batysta, R. Boge, E. Erdman, M. Greco, J. T. Green, **Hubka, Z.**, L. Indra, K. Majer, T. Mazanec, P. Mazůrek, J. Naylon, J. Novák, V. Šobr, A. Špaček, M. Torun, B. Tykalewicz, P. Bakule, and B. Rus, "The current commissioning results of the Allegra kilohertz high-energy laser system at ELI-Beamlines," in *Laser Congress 2019 (ASSL, LAC, LS&C)*, Optical Society of America, 2019, ATh1A.6. DOI: 10.1364/ASSL.2019.ATh1A.6.

[14] R. Boge, J. Horáček, P. Mazůrek, J. A. Naylon, J. Novák, F. Batysta, **Hubka, Z.**, V. Šobr, R. Antipenkov, J. T. Green, P. Bakule, and B. Rus, "Active cavity stabilization for high energy thin disk regenerative amplifier," in *High-Power, High-Energy, and High-Intensity Laser Technology III*, International Society for Optics and Photonics, vol. 10238, SPIE, 2017, pp. 46–51. DOI: 10.1117/12.2270607.

[15] P. Bakule, R. Antipenkov, J. T. Green, J. Novák, F. Batysta, B. Rus, R. Boge, **Hubka, Z.**, J. A. Naylon, M. Horáček, J. Horáček, P. Strkula, D. Snopek, L. Indra, and B. Tykalewicz, "Development of high energy, sub-15 fs OPCPA system operating at 1 kHz repetition rate for ELI-Beamlines facility," in *Research Using Extreme Light: Entering New Frontiers with Petawatt-Class Lasers III*, International Society for Optics and Photonics, vol. 10241, SPIE, 2017, pp. 21–29. DOI: 10.1117/12.2270598.

[16] R. Antipenkov, F. Batysta, R. Boge, *et al.*, "The construction of Allegra kilohertz femtosecond laser system at ELI-Beamlines," in *Short-pulse High-energy Lasers and Ultrafast Optical Technologies*, International Society for Optics and Photonics, vol. 11034, SPIE, 2019, pp. 58–63. DOI: 10.1117/12.2524436.

[17] J. Novák, P. Bakule, J. T. Green, **Hubka, Z.**, and B. Rus, "100 mJ thin disk regenerative amplifier at 1 kHz as a pump for picosecond OPCPA," in *CLEO: 2015*, Optical Society of America, 2015, STu4O.4. DOI: 10.1364/CLEO_SI.2015.STu4O.4.

Research Article Vol. 60, No. 3 / 20 January 2021 / Applied Optics 533

applied optics

Mitigation of laser-induced contamination in vacuum in high-repetition-rate high-peak-power laser systems

Zbyněk Hubka,[1,2,*] Jakub Novák,[1] Irena Majerová,[1] Jonathan T. Green,[1] Praveen K. Velpula,[1] Robert Boge,[1] Roman Antipenkov,[1] Václav Šobr,[1] Daniel Kramer,[1] Karel Majer,[1] Jack A. Naylon,[1] Pavel Bakule,[1] and Bedřich Rus[1]

[1]ELI Beamlines, Institute of Physics, Czech Academy of Sciences, Na Slovance 2, 18221 Prague, Czech Republic
[2]Czech Technical University in Prague, Faculty of Nuclear Sciences and Physical Engineering, Břehová 7, 115 19 Prague, Czech Republic
*Corresponding author: zbynek.hubka@eli-beams.eu

Received 12 November 2020; revised 14 December 2020; accepted 15 December 2020; posted 16 December 2020 (Doc. ID 414878); published 11 January 2021

Vacuum chambers are frequently used in high-energy, high-peak-power laser systems to prevent deleterious nonlinear effects, which can result from propagation in air. In the vacuum sections of the Allegra laser system at ELI-Beamlines, we observed degradation of several optical elements due to laser-induced contamination (LIC). This contamination is present on surfaces with laser intensity above 30 GW/cm^2 with wavelengths of 515, 800, and 1030 nm. It can lead to undesired absorption on diffraction gratings, mirrors, and crystals and ultimately to degradation of the laser beam profile. Because the Allegra laser is intended to be a high-uptime source for users, such progressive degradation is unacceptable for operation. Here, we evaluate three methods of removing LIC from optics in vacuum. One of them, the radio-frequency-generated plasma cleaning, appears to be a suitable solution from the perspective of operating a reliable, on-demand source for users.

https://doi.org/10.1364/AO.414878

1. INTRODUCTION

It is quite common for large portions of high-energy high-power lasers to be in vacuum in order to avoid problems with nonlinear effects like self-focusing or self-phase modulation [1,2]. The components in such vacuum systems must be chosen carefully to avoid contamination of optical surfaces under vacuum. Degassing of materials or contamination in an optical system can pose a risk for optics by creation of an adsorbed layer on it. While optical surface quality can degrade in air due to the accumulation of layers of contamination [3], their growth is much more pronounced in vacuum environments. The need to remove these layers from optics has been known since the beginning of the satellite programs [4]. Wide use of synchrotrons generating extreme UV in the 1980s and 1990s showed that the growth of these layers is strongly linked with a presence of UV or x-ray radiation [5–9]; this phenomenon is often called "radiation-induced contamination" or "laser-induced contamination" (LIC).

The source of this contamination is mostly low-vapor-pressure hydrocarbon molecules present in vacuum chambers, which are difficult to remove with vacuum pumps. These molecules dissociate by photon-induced ionization (called cracking) and deposit a carbonaceous layer on the optical surfaces. The growth mechanism of this contamination has been previously modeled [10,11].

Hydrocarbon contamination degrades the performance of optical components, which is a problem in scanning electron microscopy [12], lithography [13], or spacecraft systems using lasers with UV wavelengths [14–16]. It has also been shown that the LIC can degrade the performance of laser systems with wavelengths outside the UV region [3,17] through multiphoton absorption process and can lead to laser-induced damage [10,17,18]. Two examples of optical components from a laser system with visible LIC spots are shown in Fig. 1 and support the idea of LIC being caused by multiphoton absorption at 1030 nm.

Methods to remove the LIC from optical surfaces aim to create ionized molecules and radicals, which bond to the molecules deposited on the contaminated surface (often carbon) and generate volatile molecules (water vapor, CO_x, NO_x, etc.), which can be removed from the chamber by vacuum pumps. One of the common methods uses gaseous oxygen in combination with UV radiation (either from an external source or the laser/synchrotron itself) [12,16,19] to generate ozone or oxygen radicals, which help break down the contamination layers. Other methods include generating radicals through radio-frequency discharge [8,20] or ablating the contamination layers

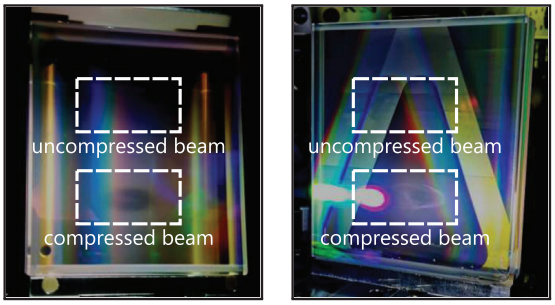

(a) (b)

Fig. 1. Laser-induced contamination spots on two dielectric gratings from two similar pulse compressors. LIC is visible only in the area where the compressed pulse hits the grating. The laser pulse parameters are 1030 nm, 3 ps, 15 mm $1/e^2$ diameter, and 200 mJ energy. (a) Grating with a darkening in the bottom part. (b) Different grating with similar contamination, with extra white edges visible due to a different camera angle. The bright white saturated area in (b) next to the LIC comes from the flashlight used to illuminate the grating.

with laser radiation [21]. Although more common in systems with UV and x-ray wavelengths, short-pulse near-infrared lasers can also suffer from LIC. Here, we describe how LIC affects the performance of the Allegra laser and how it can be mitigated *in situ* allowing high uptime for the laser source.

Allegra is a high-repetition-rate, high-energy, high-average-power, ultrashort pulse laser intended to be used for laser-driven x-ray and XUV light source experiments [22]. The system is based on picosecond optical parametric chirped pulse amplification (OPCPA) and is designed to generate 100 mJ, sub 15 fs pulses at 1 kHz.

To avoid nonlinear effects in air, we placed a large portion of the system inside vacuum, including three diffraction grating-based Treacy compressors, three second-harmonic (SHG) stages, three OPCPA sections, and a series of chirped mirrors for final pulse compression. The laser system is designed for user operation with maximum uptime, and significant attention is given to its stability, high reliability, and automation [23–25]. Because of the high demands for operation, it is not reasonable to regularly remove optics from carefully aligned optical systems in vacuum for cleaning. To maintain the maximum possible uptime, cleaning must be performed *in situ* with minimal disturbance to the laser.

Although there are other laser systems within ELI-Beamlines with similar laser pulse intensities but lower repetition rates (10 Hz and lower), under similar vacuum conditions, it is only the 1 kHz Allegra laser that has observed beam degradation due to LIC, indicating that the repetition rate is an important factor in developing the contamination layers.

A. LIC in Allegra Laser System

After a given period of laser operation, typically five days of operation at 20 mJ output (10^7 shots), we begin to notice changes in the laser performance and can observe LIC on optics in vacuum (typical pressure reached in our chambers is $\sim 10^{-6}$ mbar) in both broadband amplification stages as well as in the pump pulse compressors. It is represented by a darkening, with bright edges

Table 1. Fluence and Intensity of Laser Pulse with Different Wavelengths on Optical Surfaces inside Vacuum Chamber and Presence of LIC Spots[a]

Wavelength	Pulse Duration	Fluence	Intensity	LIC Visible
1030 nm	0.5 ns	260 mJ/cm^2	0.5 GW/cm^2	no
1030 nm	3 ps	260 mJ/cm^2	87 GW/cm^2	yes
515 nm	3 ps	113 mJ/cm^2	38 GW/cm^2	yes
750–920 nm	3 ps	6.5 mJ/cm^2	2.2 GW/cm^2	no
750–920 nm	15 fs	6.5 mJ/cm^2	430 GW/cm^2	yes

[a]Repetition rate of laser pulses is 1 KHz.

from certain viewing angles, as shown in Fig. 1. The spots are the same size as the laser beam (~15 mm@$1/e^2$) and have the shape of a donut, with the middle part being lighter in color, similar to what was previously observed [16,18,26]. To capture them on a camera can be quite challenging, as the spots are usually visible only from a narrow range of angles.

From our experience, the presence of LIC spots is closely correlated to the laser pulse intensity rather than pulse fluence, as we only observe LIC on optics where the laser pulses are compressed and see nothing where those same pulses are stretched. This indicates the higher the laser pulse intensity is, the faster LIC accumulates up to the point where it is visible with the naked eye (see Table 1 for details). The visual presence of darkened LIC spots on mirrors, OPCPA and SHG crystals, and diffraction gratings degrades their performance by introducing absorption. Contaminated gratings also suffer from increased diffraction into the 0th order.

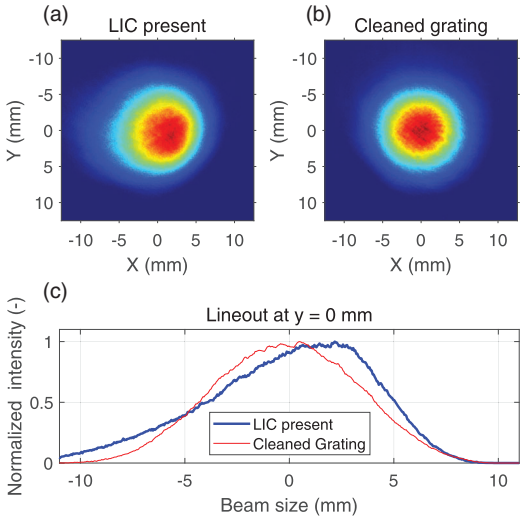

Fig. 2. Comparison of the 1030 nm Treacy compressor output beam profile before and after 12 h of cleaning the vacuum chamber with the RF plasma source. (a) Distorted beam profile with contaminated optics present in the compressor. (b) Undistorted beam profile after cleaning the chamber with an RF plasma source overnight. (c) Beam profile lineout at the center. The source of distortion might be related to the asymmetric absorption on the grating with LIC present (data in Fig. 8) or to a different setpoint of active beam-pointing stabilization system, causing a slightly different overlap of the laser beam and LIC, present on the optics in the chamber.

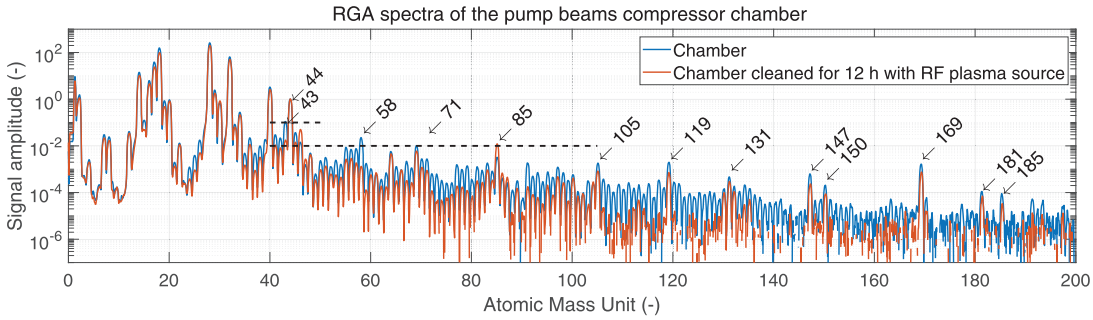

Fig. 3. RGA spectra of the pump pulse compressor chamber, both measured at $\sim 10^{-6}$ mbar. Both data sets are normalized to the atomic mass units (amu) 44 peak. The blue data set was measured one day after the chamber was evacuated; the orange data set after 12 h or running the RF plasma source. After the cleaning, in most cases, the amplitude of the peaks above 100 amu decreased by almost an order of magnitude. Despite this visible improvement, the presence of peaks at amu 71, 85, 105, 119, 131, 147, 150, 169, 181, and 185 still suggests some level of contamination in the chamber.

If not eliminated, these LIC spots can lead to undesirable losses of energy inside the system and eventually to catastrophic failure through laser-induced damage. In our case, the spot on the left grating in Fig. 1 caused the efficiency of the grating diffraction to drop by 13% and to the creation of distorted beam profiles, visible in Fig. 2.

B. Possible Sources of Contamination

We have made efforts to keep our vacuum chambers as clean as possible and use vacuum-compatible materials such as stainless steel, aluminum, and Kapton and Teflon materials with vacuum-compatible lubricants. All components placed into the chambers are ultrasonically cleaned. The chambers are evacuated using turbomolecular pumps with dry screw vacuum pumps for prevacuum. Flanges and doors are sealed using unbaked Viton O-rings.

When looking at typical residual gas analyzer (RGA) spectra of our pump laser compressor chamber in Fig. 3, we can compare two traces. In the first one, the chamber was vented, opened, and evacuated again. The second trace is after cleaning the chamber for 12 h with an RF plasma source, which greatly improves the situation. The ratio between the amplitude of the peaks with amu 44 (CO_2) and amu 43 (hydrocarbon C_3H_7) is below 1/10, and the amplitude of peaks above amu 44 is $\leq$1/100 of the amu 44 peak, which is in accordance with the laser interferometer gravitational-wave observatory (LIGO) standard [27].

Both RGA spectra show concentrations of hydrocarbon constituents, indicated by groups of peaks separated by 14 amu related to CH_2 as well as multiple peaks with amu >100. The peak with amu 58 is usually caused by the Viton O-rings used on all the doors and flanges. The peaks with amu 119, 131, 147, 150, 169, or 185 are most probably linked with the use of perfluoropolyether-based grease, and their amplitude is not getting much smaller after the RF plasma cleaning process. That can be explained by the absence of hydrocarbons in this type of grease. Other peaks and the hydrocarbon groups in Fig. 3 might be linked to the hydrocarbon-based ultrahigh vacuum grease used in the past and to the fact that our chambers were cleaned with vacuum wipes soaked in acetone and isopropyl-alcohol immediately after the manufacturing process. Contamination from the wipes is supported by Fourier-transform infrared spectroscopy tests from the walls showing clear presence of polyester molecules.

2. METHODS OF REMOVING LIC FROM OPTICS

We have tested the following three methods to eliminate LIC from our optics: UV-ozone cleaning, laser pulse cleaning, and RF plasma cleaning. We used three nonidentical contaminated mirrors from a different laser, the Ti:sapphire section of a Prague Asterix laser system [28], with different degrees of contamination. The following results were obtained in a small, dedicated vacuum chamber with the contaminated mirrors facing the cleaning device/beam at an angle of 45 deg. All of the methods successfully removed the LIC from the optical surface, and their specifics are described below.

A. UV-ozone Cleaning

For this cleaning method, we used atmospheric pressure inside the small chamber and mounted a simple commercially available 3 W mercury lamp to one of the flanges of the chamber. The UV light from the lamp creates oxygen radicals (while generating ozone as an intermediate step) from the air in the chamber and is also absorbed by the contaminants, helping the cleaning process. A more detailed description of the method can be found in [16]. It took 20 h to completely clean a contaminated mirror, while its reflectivity improved by 12% back to its original value. Results are shown in Fig. 4(c).

B. RF Plasma Source Cleaning

With the RF source, we evacuated the chamber and ran a cleaning cycle with an Evactron E50 RF plasma source mounted on a flange. It took 4 h to completely clean a contaminated mirror, while the reflectivity improved by 35% back to its original value. The improvement in reflectivity is shown in Fig. 4(b), and a visual comparison under a microscope is shown in Fig. 5.

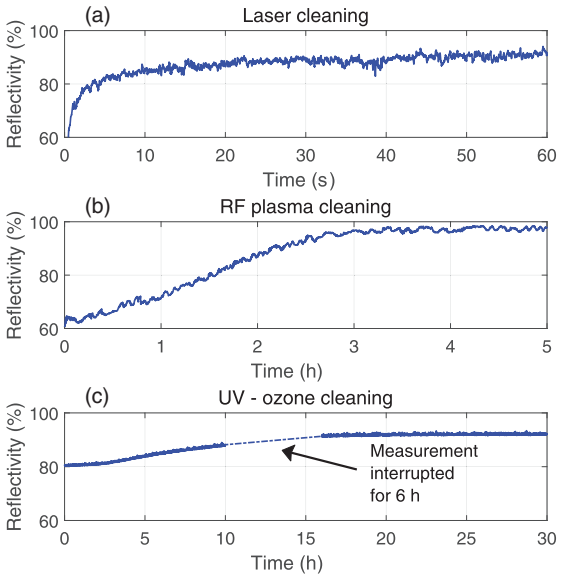

Fig. 4. Results of three LIC cleaning methods from three different mirrors in a dedicated small chamber, arranged from the fastest method on top. Although the laser cleaning seems faster (time scale in seconds), it would later require scanning the whole surface area affected by LIC. Microscope details of the surface cleaned by RF plasma source are shown in Fig. 5.

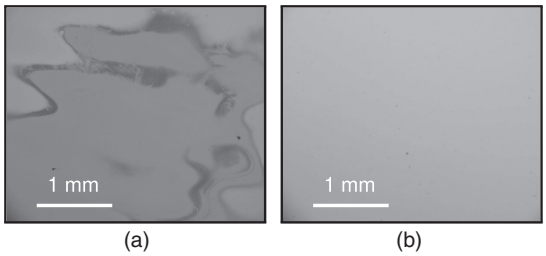

Fig. 5. Comparison of a mirror surface from a different system (beam transport of Ti:sapphire section of Prague Astrix laser system) under microscope. (a) Details of a contaminated area. (b) Same area after 5 h of RF plasma cleaning.

C. Laser Cleaning

For the laser cleaning method, we evacuated the chamber and partially filled it with oxygen (partial pressure 0.4 mbar). We irradiated the contaminated area with ultrashort pulses from a coherent Astrella laser with a fluence of 35 mJ/cm^2, repetition rate of 1 kHz, pulse duration of 50 fs, and central wavelength of 800 nm. The laser spot had a 500 μm 1/e^2 diameter. It took only 1 min to completely clean a contaminated spot on the mirror, while the reflectivity of the spot improved by 45% back to its original value, as shown in Fig. 4(a). Contrary to the other two cleaning methods mentioned in this section, removing the whole contamination would later require scanning across the contaminated surface. With LIC spots as big as 800 mm^2 on the gratings, it would take more than 16 h to clean with the cleaning laser spot of the same size.

Using this method for cleaning the contaminated optics in the Allegra system vacuum chambers, by reaching similar conditions (partial atmosphere or oxygen pressure and intensities of ∼1 TW/cm^2) and utilizing the same laser beam, which causes the LIC in the first place, is not feasible for our system at the moment. The slower cleaning rate, due to lower intensities (see Table 1), possible self-focusing, due to the partial pressure in the chambers and plasma generation due to the presence of foci in the imaging system, did not justify the risks involved. Instead, due to its simplicity and ease of use, we chose the RF plasma source as the most suitable method for cleaning optics in the Allegra vacuum chambers.

3. *IN SITU* TEST OF LIC REMOVAL

For the *in situ* test, we chose to characterize one of the dielectric gratings from a compressor inside the pump pulse compressor chamber [marked as (1) in the layout in Fig. 6]. The original average diffraction efficiency of the grating was 97%. This grating is hit by the laser pulse twice: first on its way in, while still stretched, and then once again on the way out where the pulse is compressed. No LIC is observed where the stretched pulse hits the grating, while LIC is clearly visible where the pulse is compressed. This is shown in Fig. 1.

The RF plasma source was mounted to the top of the chamber with the flange being roughly 60 cm away from surface of the grating with the LIC spot.

To test the effectiveness, we ran the RF source *in situ*. To evaluate the level of LIC on the grating after each cleaning iteration, we measured the diffraction efficiency of the −1st and 0th order across the spot with the LIC. For that, we used a small 1030 nm CW beam and moved the grating on a translation stage, as depicted in Fig. 7. After the measurement, we returned

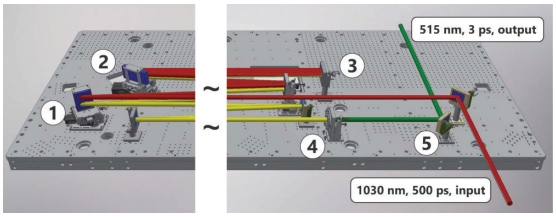

Fig. 6. Compressor layout inside the chamber: 1) first diffraction grating; 2) second diffraction grating; 3) end mirror, which folds the beam back through the compressor under a slightly different angle, resulting in two distinct laser spots on both gratings where the laser beam hits both gratings; 4) SHG crystal; 5) dichroic mirror separating 515 nm from residual 1030 nm.

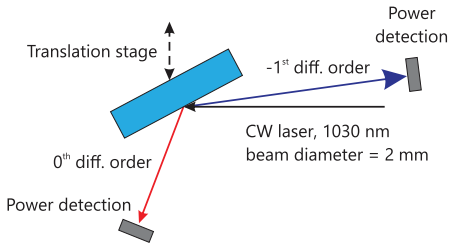

Fig. 7. Diffraction efficiency measurement layout.

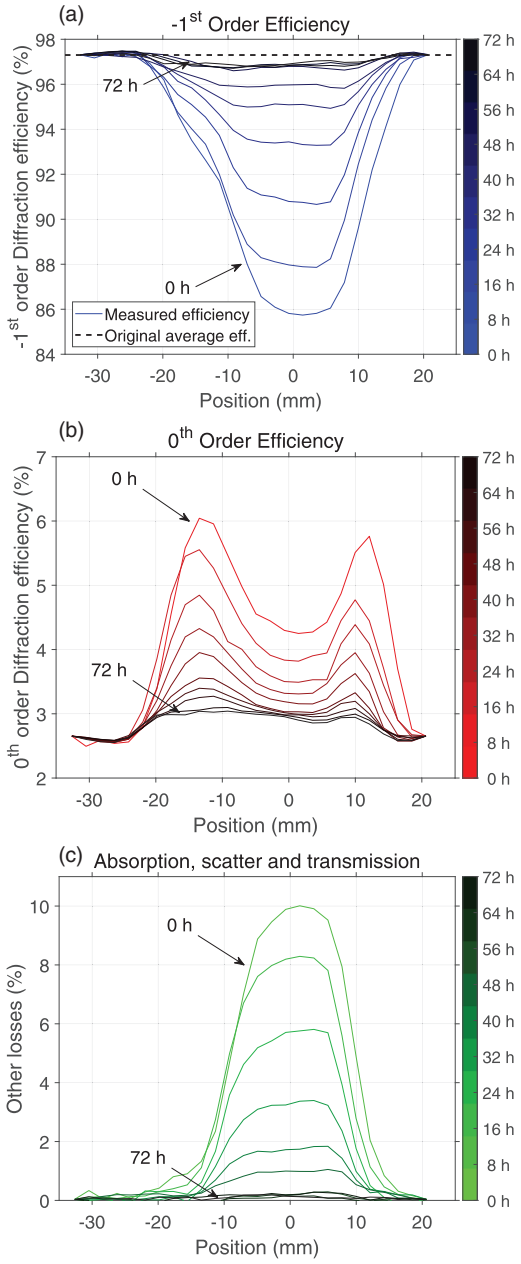

Fig. 8. Experimental data with the dielectric grating from the compressor chamber, using nine cycles (8 h each) of RF plasma source cleaning. (a) Evolution of the −1st order diffraction efficiency. (b) Evolution of the 0th order diffraction efficiency. (c) Other losses besides reflection calculated from (a) and (b).

the grating to its mount in the chamber, evacuated the chamber to $\sim 10^{-6}$ mbar, and ran the 8 h RF plasma cleaning cycle while running the turbomolecular pump at maximum speed. After this cleaning cycle, the grating was removed and measured again. This process was repeated nine times, until the diffraction efficiency in the center of the LIC spot no longer improved, as shown in Fig. 8.

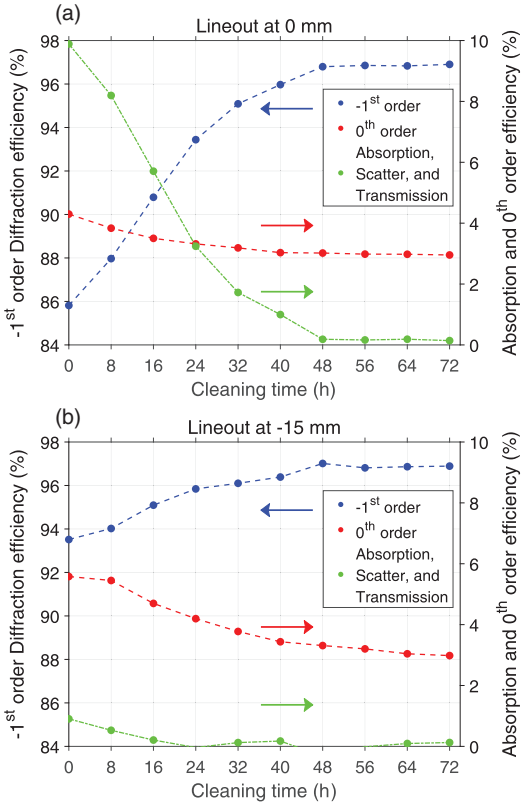

Fig. 9. Lineouts at two different positions from Fig. 8. (a) At 0 mm, indicating the center of the LIC spot where the change of the −1st order diffraction efficiency and other losses are more pronounced. (b) At −15 mm, indicating the center of the left peak in 0th order diffraction.

The data show that the "donut" shape of the LIC influences mainly the 0th order efficiency, which is larger on the edges of the LIC spot. The reason for this shape is not clear at the moment and will be the subject of future investigation. Apart from this, the overall diffraction efficiency of the −1st order is lower mainly in the center due to the absorption caused by the carbon layer. Most of the improvement occurred in the first 48 h of the cleaning cycle, as shown in Fig. 9(a), which illustrates the progress of the efficiency of −1st and 0th order and the calculated absorption during the cleaning process. RF plasma cleaning improved the diffraction efficiency of the −1st order by 13%, after which the LIC spot visually disappeared.

A. RF Source Placement Consideration

After 72 h of cleaning cycles, the LIC from the gratings was removed; however, the LIC on the dichroic mirror, which was positioned on the other side of the same chamber, did not disappear. This suggests the RF plasma cleaning is a viable solution only for the optical surfaces close to the RF source itself, probably due to the lower concentration of radicals farther from the plasma source. Other components in the chamber, which can block optical surfaces from the plasma source, may also decrease the efficiency of the cleaning. In addition, the placement of the

turbomolecular pump (in our case at the center bottom of the chamber) is important. It influences the cleaning efficiency of surfaces on the other side of the chamber as the generated ions are drifting from the RF plasma source toward the pump.

All this should be taken into consideration when choosing the method of cleaning or, in our case, the placement of the RF plasma source. For instance, in order to clean the dichroic mirror, the RF source needed to be placed on the other side of the chamber, closer to the mirror itself.

4. CONCLUSION

We identified LIC to be a problem for optical surfaces in vacuum in the Allegra laser system. Visible contamination was present only on the surfaces with compressed (<3 ps) laser pulses with intensities higher than 30 GW/cm^2. The wavelength of the laser does not play a significant role, as the contamination was observed for wavelengths at 515, 830, and 1030 nm. Based on the lack of LIC in other high-intensity lasers at ELI, average power and high repetition rate appear to be a factor in the deposition along with high intensity. The influence of LIC presence and its removal on the laser-induced damage threshold was not measured and would require a separate study.

We concluded that the RF source is a suitable solution to avoid problems with LIC in the future if the cleaning runs are scheduled regularly.

Funding. European Regional Development Fund (ADONIS, CZ.02.1.01/0.0/0.0/16–019/0000789); Ministry of Education, Youth, and Sports of the Czech Republic (NPS II Project No. LQ1606).

Disclosures. The authors declare no conflicts of interest.

REFERENCES

1. S. Toth, T. Stanislauskas, I. Balciunas, R. Budriunas, J. Adamonis, R. Danilevicius, K. Viskontas, D. Lengvinas, G. Veitas, D. Gadonas, A. Varanavičius, J. Csontos, T. Somoskoi, L. Toth, A. Borzsonyi, and K. Osvay, "SYLOS lasers–the frontier of few-cycle, multi-TW, kHz lasers for ultrafast applications at extreme light infrastructure attosecond light pulse source," J. Phys. Photon. **2**, 045003 (2020).
2. R. Antipenkov, F. Batysta, R. Boge, E. Erdman, M. Greco, J. T. Green, Z. Hubka, L. Indra, K. Majer, T. Mazanec, P. Mazůrek, J. Naylon, J. Novák, V. Šobr, A. Špaček, M. Torun, B. Tykalewicz, P. Bakule, and B. Rus, "The current commissioning results of the Allegra kilohertz high-energy laser system at ELI-beamlines," in *Laser Congress 2019 (ASSL, LAC, LS&C)* (Optical Society of America, 2019), paper ATh1A.6.
3. P. Zhang, Y. Jiang, J. Wang, W. Fan, X. Li, and J. Zhu, "Improvements in long-term output energy performance of Nd:glass regenerative amplifiers," High Power Laser Sci. Eng. **5**, e23 (2017).
4. R. B. Gillette, J. R. Hollahan, and G. L. Carlson, "Restoration of optical properties of surfaces by radiofrequency-excited oxygen," J. Vac. Sci. Technol. **7**, 534–537 (1970).
5. K. Boller, R.-P. Haelbich, H. Hogrefe, W. Jark, and C. Kunz, "Investigation of carbon contamination of mirror surfaces exposed to synchrotron radiation," Nucl. Instrum. Methods Phys. Res. **208**, 273–279 (1983).
6. E. D. Johnson and R. F. Garrett, "In situ reactive cleaning of x-ray optics by glow discharge," Nucl. Instrum. Methods Phys. Res. A **266**, 381–385 (1988).
7. R. A. Rosenberg and D. C. Mancini, "Deposition of carbon on gold using synchrotron radiation," Nucl. Instrum. Methods Phys. Res. A **291**, 101–106 (1990).
8. B. R. Müller, J. Feldhaus, F. Schäfers, and F. Eggenstein, "Cleaning of carbon contaminated vacuum ultraviolet-optics: influence on surface roughness and reflectivity," Rev. Sci. Instrum. **63**, 1428–1431 (1992).
9. P. Yadav, M. Modi, M. Swami, and P. Singh, "Ex-situ characterization of synchrotron radiation induced carbon contamination on LiF window," J. Electron Spectrosc. Relat. Phenom. **211**, 64–69 (2016).
10. D. Kokkinos, H. Schröder, K. Fleury-Frenette, M. Georges, W. Riede, G. Tzeremes, and P. Rochus, "Laser optics in space failure risk due to laser induced contamination," CEAS Space J. **9**, 153–162 (2016).
11. J. T. Hollenshead, L. E. Klebanoff, and G. Delgado, "Predicting radiation-induced carbon contamination of EUV optics," J. Vac. Sci. Technol. B **37**, 021602 (2019).
12. H. D. Wanzenboeck, P. Roediger, G. Hochleitner, E. Bertagnolli, and W. Buehler, "Novel method for cleaning a vacuum chamber from hydrocarbon contamination," J. Vac. Sci. Technol. A **28**, 1413–1420 (2010).
13. R. R. Kunz, V. Liberman, and D. K. Downs, "Experimentation and modeling of organic photocontamination on lithographic optics," J. Vac. Sci. Technol. B **18**, 1306–1313 (2000).
14. W. Riede, P. Allenspacher, H. Schröder, D. Wernham, and Y. Lien, "Laser-induced hydrocarbon contamination in vacuum," Proc. SPIE **5991**, 59910H (2006).
15. R. Schäfer, G. Schmidtke, T. Strahl, M. Pfeifer, and R. Brunner, "EUV data processing methods of the solar auto-calibrating EUV spectrometers (SolACES) aboard the International Space Station," Adv. Space Res. **59**, 2207–2228 (2017).
16. N. Bartels, P. Allenspacher, W. Riede, H. Schröder, and D. Wernham, "Removal of laser-induced contamination on ALADIN laser optics by UV/ozone cleaning," Proc. SPIE **11173**, 98–107 (2019).
17. F. E. Hovis, B. A. Shepherd, C. T. Radcliffe, A. L. Bailey, and W. T. Boswell, "Optical damage at the part per million level: the role of trace contamination in laser-induced optical damage," Proc. SPIE **2114**, 145–153 (1994).
18. S. Becker, A. Pereira, P. Bouchut, F. Geffraye, and C. Anglade, "Laser-induced contamination of silica coatings in vacuum," Proc. SPIE **6403**, 189–200 (2007).
19. T. Koide, T. Shidara, K. Tanaka, A. Yagishita, and S. Sato, "In situ DC oxygen-discharge cleaning system for optical elements," Rev. Sci. Instrum. **60**, 2034–2037 (1989).
20. R. Vane, "Immobilization and removal of hydrocarbon contamination using the Evactron® de-contaminator," Microsc. Microanal. **12**, 1662–1663 (2006).
21. S. Georgiou, "Laser Cleaning Methodologies of Polymer Substrates," in *Polymers and Light. Advances in Polymer Science*, (Springer, 2004), pp. 1–50.
22. O. Hort, M. Albrecht, V. Nefedova, O. Finke, D.-D. Mai, S. Reyné, F. Giambruno, F. Frassetto, L. Poletto, J. Andreasson, G. Julien, S. Sebban, and J. Nejdl, "High-flux source of coherent XUV pulses for user applications," Opt. Express **27**, 8871–8883 (2019).
23. F. Batysta, R. Antipenkov, J. T. Green, J. A. Naylon, J. Novák, T. Mazanec, P. Hříbek, C. Zervos, P. Bakule, and B. Rus, "Pulse synchronization system for picosecond pulse-pumped OPCPA with femtosecond-level relative timing jitter," Opt. Express **22**, 30281–30286 (2014).
24. M. Horáček, L. Indra, J. T. Green, J. A. Naylon, B. Tykalewicz, J. Novák, F. Batysta, T. Mazanec, J. Horáček, R. Antipenkov, Z. Hubka, R. Boge, P. Bakule, and B. Rus, "Multi-channel, fiber-based seed pulse distribution system for femtosecond-level synchronized chirped pulse amplifiers," Rev. Sci. Instrum. **88**, 013109 (2017).
25. R. Boge, J. Horáček, P. Mazůrek, J. A. Naylon, J. T. Green, Z. Hubka, V. Šobr, J. Novák, F. Batysta, R. Antipenkov, P. Bakule, and B. Rus, "Robust method for long-term energy and pointing stabilization of high energy, high average power solid state lasers," Rev. Sci. Instrum. **89**, 023113 (2018).
26. F. R. Wagner, G. G. El Reaidy, D. Faye, and J. Y. Natoli, "Laser induced deposits in contaminated vacuum environment: optical properties and lateral growth," Opt. Laser Technol. **122**, 105889 (2020).
27. "LIGO document E080177-v2: RGA test qualification of components for the LIGO UHV," 2020, https://dcc.ligo.org/LIGO-E080177/public.
28. J. Hřebíček, B. Rus, J. C. Lagron, J. Polan, T. Havlíček, T. Mocek, J. Nejdl, and M. Pešlo, "25 TW Ti:sapphire laser chain at PALS," Proc. SPIE **8080**, 142–148 (2011).

Letter Vol. 46, No. 22 / 15 November 2021 / Optics Letters 5655

120 mJ, 1 kHz, picosecond laser at 515 nm

Zbyněk Hubka,[1,2,*] Roman Antipenkov,[1] Robert Boge,[1] Emily Erdman,[1,3] Michael Greco,[1] Jonathan T. Green,[1] Martin Horáček,[1] Karel Majer,[1] Tomáš Mazanec,[1] Petr Mazůrek,[1] Jack A. Naylon,[1] Jakub Novák,[1] Václav Šobr,[1] Petr Strkula,[1] Murat Torun,[1] Boguslaw Tykalewicz,[1] Pavel Bakule,[1] and Bedřich Rus[1]

[1]ELI Beamlines, Institute of Physics, Czech Academy of Sciences Na Slovance 2, 18221 Prague, Czech Republic
[2]Czech Technical University in Prague, Faculty of Nuclear Sciences and Physical Engineering Břehová 7, 115 19 Prague, Czech Republic
[3]Charles University, Faculty of Mathematics and Physics, Ke Karlovu 2027/3, 12116 Prague, Czech Republic
*Corresponding author: zbynek.hubka@eli-beams.eu

Received 18 August 2021; revised 15 October 2021; accepted 20 October 2021; posted 21 October 2021 (Doc. ID 440448); published 9 November 2021

We report on a 1 kHz, 515 nm laser system, based on a commercially available 230 W average power Yb:YAG thin-disk regenerative amplifier, developed for pumping one of the last optical parametric chirped pulse amplification (OPCPA) stages of the Allegra laser system at ELI Beamlines. To avoid problems with self-focusing of picosecond pulses, the 1030 nm output pulses are compressed and frequency doubled with an LBO crystal in vacuum. Additionally, development of a thermal management system was needed to ensure stable phase matching conditions at high average power. The resulting 515 nm pulses have an energy of more than 120 mJ with SHG efficiency of 60% and an average RMS stability of 1.1% for more than 8 h.

https://doi.org/10.1364/OL.440448

ELI Beamlines is a facility that provides high peak power and high average power lasers and secondary sources of radiation for user-driven basic and applied research, including particle-acceleration, plasma physics experiments, and ultra-high intensity laser–matter interactions. The laser systems at ELI Beamlines are based on a variety of amplification technologies such as Ti:sapphire [1], Nd:glass [2], and optical parametric chirped pulse amplification (OPCPA) [3]. The Allegra laser is a high repetition rate (1 kHz) OPCPA system aimed at driving various x ray sources such as a plasma x ray source [4] and a high-harmonic source [5] for probing ultra-fast dynamics of processes in various types of samples. The benefits of OPCPA over Ti:sapphire amplification are simpler geometries not requiring multi-pass arrangements, smaller thermal lensing due to the lack of intrinsic heat deposition in the amplification crystals, and better contrast due to the absence of spontaneous emission [6]. Picosecond OPCPA especially has exceptional contrast due to the complete lack of superfluorescence photons outside the picosecond window of the pump pulse [7,8]. Another advantage of using picosecond pulses for both broadband amplification as well as frequency doubling of infrared pump lasers is the higher intensity on nonlinear crystals allowing crystals with thicknesses of only a few mm to be used.

The Allegra OPCPA chain consists of seven stages pumped by five pump lasers. In order to ensure consistent output of the laser system, reliable and stable pump lasers centered near 515 nm are required. Frequency doubled Yb:YAG thin-disk amplification was chosen as the pump laser technology for Allegra system; in recent years, such thin-disk-based regenerative amplifiers have proved to be excellent sources of high repetition rate, picosecond pulse trains with output energies over 100 mJ at 1030 nm [9,10]. In the Allegra system, the thin-disk amplifiers are run in a chirped pulse configuration, and compression to picosecond pulse duration is done via Treacy compressors with multilayer dielectric gratings. A large portion of the L1 Allegra system is in vacuum, including the compressors and SHG stages for the last three pump lasers (one of them is the pump laser described in this paper), the last three OPCPA stages, and the final chirped mirror compressor. Such a configuration avoids transmission of high intensity pulses through vacuum windows and the associated nonlinearities. It also eliminates self-phase modulation and Kerr-lensing effects in air which would otherwise corrupt and focus the fundamental 1030 nm laser pulses over the distances we are using.

LBO is selected as the frequency doubling crystal due to its favorable properties such as large aperture and large angular acceptance. With the designed intensity of the incident 1030 nm picosecond pulses on the SHG crystal of 100 GW/cm^2, crystals with a length of just 1–3 mm are needed to reach near maximum conversion efficiency. With such thin nonlinear crystals, surface absorption is dominant over bulk absorption [11,12], due to defects and roughness influenced by polishing, and the absorption in anti-reflection coatings. Because the SHG crystals for the high average power pump lasers are in vacuum, even a modest deposition of heat in the crystal and/or crystal mount results in an increase in crystal temperature and degraded phase matching, which requires angular corrections [13]. In order to ensure long-term stable operation

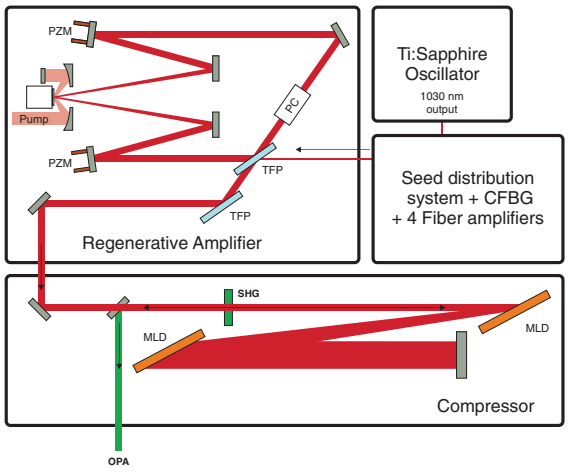

Fig. 1. Layout of the pump laser. The 1030 nm seed pulses generated by a long-wavelength module of the Ti:sapphire oscillator are stretched by a chirped fiber Bragg grating (CFBG) and amplified in the seed distribution system. The regenerative amplifier has a ring cavity design with piezo-driven mirrors (PZM), thin-film polarizers (TFP), and Pockels cell (PC). The multilayered dielectric grating (MLD) compressor, together with the LBO crystal inside the kinematic mount for frequency doubling (SHG), are placed in a vacuum chamber.

of the laser, it is important to address the thermal management and temperature stabilization properly.

The overview of the layout of the whole pump laser system described in this paper is in Fig. 1. To provide the 1030 nm seed pulses for the regenerative amplifier, we are using an in-house developed fiber seed distribution system [14], which is seeded by a long-wavelength portion of the spectrum from a mode-locked Ti:sapphire oscillator (Rainbow, Femtolasers). The 80 MHz pulses from the oscillator are stretched in a CFBG stretcher (−477 ps/nm, Teraxion), and their repetition rate is reduced by Mach–Zehnder interferometer pulse pickers. The 30 pJ seed pulses are then amplified in a commercially available regenerative amplifier (DIRA 200–1, Trumpf Scientific Lasers, 50 round trips with a 74 ns round trip duration, gain of $7.5 \cdot 10^9$), resulting in a train of 224 mJ pulses at 1030 nm at 1 kHz. The pulse duration is 500 ps before being compression with a spectral bandwidth of 1 nm FWHM and an output beam diameter at $1/e^2$ of 15 mm.

To compress the amplified pulses, we are using a folded Treacy type compressor (two multilayer dielectric diffraction gratings, separated by an optical path of 4 m, with 1740 lines/mm, incident angle of 62° and overall efficiency of 90%, providing 202 mJ at 1030 nm after compression). The compressed 1030 nm pulses are then converted to 515 nm using a $33 \times 33 \times 2.1\text{mm}^3$ LBO crystal. The beamsize of the LBO crystal is 15 mm at $1/e^2$.

Compression and frequency doubling of picosecond pulses in vacuum poses a challenge for two reasons. First, we had to mitigate the issue of laser-induced contamination caused by outgassing of components placed in vacuum. We are now using regular plasma cleaning to prevent significant buildup of contamination, which allows us to operate the pump lasers on a daily basis without disrupting the time schedule of the experiments. The details were published in [15].

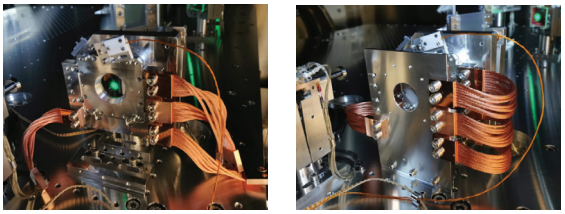

(a) (b)

Fig. 2. Solution to allow the LBO crystal in the SHG mount to reach thermal equilibrium, allowing several hours of adjustment free operation. (a) Kinematic mount with the crystal and copper straps (front mask removed for visibility). TEC elements stabilizing the mount are placed under the copper straps on the right side. (b) The same setup with the aluminium mask in front, acting as a heat-sink for the TECs due to the thermal bridge between the optical table and the SHG mount. The mask also blocks scattered light otherwise heating the mount.

The second issue that was solved was the heating of the SHG mount in vacuum. Originally, the crystal was mounted in a kinematic mount with minimal heat conduction to the optical table. For this SHG stage, the heating is mostly due to the absorption in the ion beam deposited anti-reflection coatings (measured to be 50 ppm at 1030 nm and 100 ppm at 515 nm). In the other two pump SHG stages (not covered in this paper), the dominant source of heating was the residual scattered light around the fundamental beam, which required periodic adjustment of the crystal phase matching angle when there was no temperature stabilization active. To mitigate these thermal effects, we connected the crystal holder to a heat-sink in form of a simple aluminium mask through several copper thermal straps (Technology Applications, Inc.) as shown in Fig. 2. The heat-sink mask is secured to the optical table inside the vacuum chamber, and it is sufficient to allow the SHG mount to reach thermal equilibrium during operation. To decrease the time it takes to reach thermal equilibrium, we use thermo-electric cooling elements that stabilize the temperature of the mount throughout the day to 21.5°C. The copper straps and the aluminium mask connected to the optical table act as a heatsink for the TECs. The drawback of this configuration is the transfer of excess heat to the optical table, which might affect the alignment of other optical elements in the compressor and the chamber. The future upgrade of this cooling scheme consists of a passive stainless steel cooling block mounted on the SHG crystal holder. The hollow structure of the block will be cooled by compressed air, connected by Swagelok tubing and a feedthrough flange to an air source outside of the chamber.

The laser system described here provides pulses at 515 nm with an average energy of 121 ± 1 mJ at 1 kHz over the course of 8 h (Fig. 3) without the need of phase matching corrections. To the best of our knowledge, this is currently the highest energy published from a single beam picosecond pump laser at 515 nm and 1 kHz. The transform limit of the compressed pulse spectrum is 1.4 ps, and the shortest pulse duration achieved here is 1.5 ps (PulseCheck autocorrelator, APE). The M^2 of the 515 nm beam is 1.25 and 1.21 at 10 W of output power for X and Y axes, respectively, and is worse at full power (1.94 in X and 1.63 in Y, Fig. 4). This degradation probably originates from the optical elements inside the vacuum chamber (vacuum window,

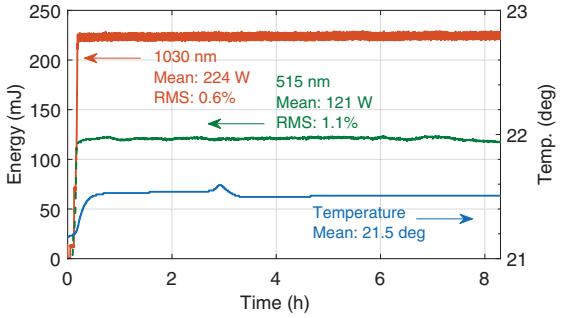

Fig. 3. Output energy of fundamental (red), second harmonic (green) pulses, and temperature (blue) of the LBO crystal holder in vacuum (stabilized by TEC elements) of the described pump laser during 8 h of operation. Compressor efficiency is 90%, and SHG efficiency is 60%. The 5% SHG energy decrease in the last 90 min is caused by the 25% decrease in the 1030 nm seed pulse energy, provided by the Ti:sapphire oscillator. Lower seed energy affects the contrast of pulses at 1030 nm and with it, the SHG efficiency.

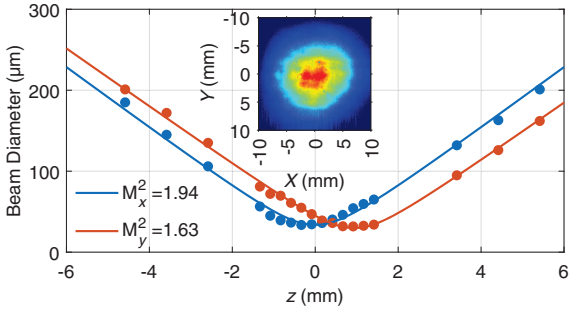

Fig. 4. M^2 measurement of 515 nm beam and near-field beam profile inset at 121 mJ (maximum output power). The M^2 of X and Y axes at low power (10 W) is 1.25 and 1.21, respectively.

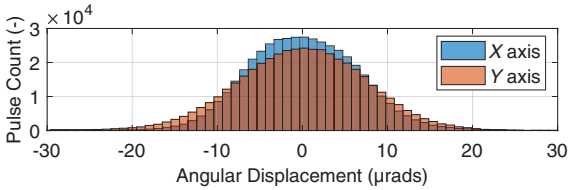

Fig. 5. Angular beam pointing stability, measured from the center beam axis during the 8 h of operation. The standard deviation in X and Y axes is 6 and 7 μrads, respectively.

gratings, mirrors, or thermal lens in LBO crystal). The M^2 measurement of the regenerative amplifier output at full power is <1.2 in both axes. The M^2 of the compressed beam at 1030 nm has not yet been measured and will be, together with the degradation of M^2 at 515 nm, subject to a future investigation. Active beam pointing stabilization ensures the standard deviation of the beam angular displacement is below 10 μrads in each axis (Fig. 5).

The achieved SHG conversion efficiency is 60% (power measured with a thermal sensor L2000W-BB-120, Ophir) and is below the value predicted by simulation with SNLO

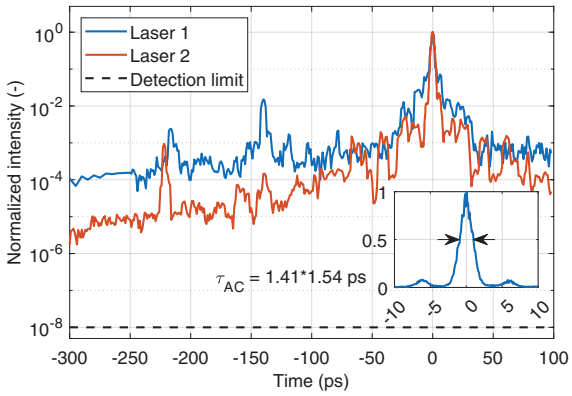

Fig. 6. Contrast measurement (third-order autocorrelator Tundra, UltraFast Innovations). Laser 1 is the one described in this paper. Laser 2 is a different pump laser seeded with a different oscillator and different stretcher. The calculated energy outside of the main Gaussian pulse within the contrast measurement window is 35% for Laser 1 and 8% for Laser 2. The SHG efficiencies of Laser 1 and Laser 2 are 60% and 75%, respectively. Inset, autocorellation trace of Laser 1 with retrieved pulse duration (PulseCheck, APE).

software [16]. A similar value was reached with comparable technology by another group [17].

A separate in-house-built laser system, 1 kHz 100 mJ regenerative amplifier with a different seed distribution system (Yb:fiber mode locked oscillator, different stretcher, and only a single fiber amplifier) has better SHG efficiency of 75%. A third-order autocorellation measurement of the fundamental pulse contrast comparing the two lasers in Fig. 6 shows how much energy is actually not contained in the main pulse. Hence, the total amount of energy available for efficient SHG conversion of the laser described in this paper is smaller, and the calculated efficiency is lower. We discuss the reasons for lower SHG efficiency later.

Although the system described here can generate more than 120 mJ at 515 nm with 1.5 ps pulses, for day-to-day operation, to increase the lifetime of optics, and for more stable OPCPA amplification [18], we do not fully compress the pulses to 1.5 ps. Instead, we use negatively stretched pulses with 3 ps duration, reaching about 100 mJ at 515 nm. Together with other pump lasers, it recently allowed the Allegra system to reach output energies above 50 mJ at 15 fs.

The reduced efficiency of the second harmonic process for this laser can be explained by the significant portion of energy being spread outside the main picosecond pulse, which is not, due to the low intensity, converted to 515 nm. The measured SHG efficiency dependence on the compressed pulse energy at 1030 nm is in Fig. 7. The simulation in SNLO software matches the measured data if we assume 31.5% of the fundamental energy is outside the main pulse. Most likely, there are two main reasons for this energy distribution. First, the dispersion is uncompensated, creating wings in the autocorrelation trace and pedestal around the main pulse in the contrast measurement (Fig. 6). The amount of extra dispersion might be influenced by the stretcher due to manufacturing tolerances and by B-integral in the regenerative amplifier cavity. We are planning to address this issue by replacing the stretcher with an improved version

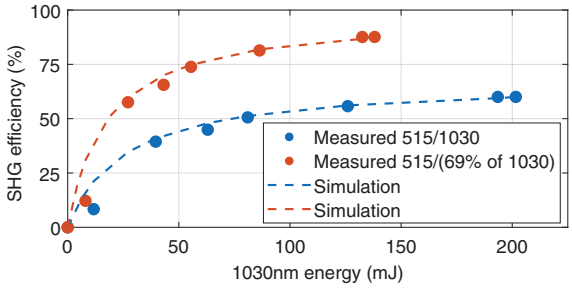

Fig. 7. Measured SHG efficiency and a corresponding theoretical simulation in SNLO. Blue data points show efficiency calculated from power measurement, and the blue curve is simulated assuming 31.5% of the energy at 1030 nm is not converted. Red data points show efficiency calculated after correction for the unconverted energy, and the red curve is the same simulation, plotted against the corrected amount of energy. Best case efficiency after correction is 88%. Similarly high SHG efficiency was reported from an SHG stage converting nanosecond pulses with energy of 650 mJ in LBO at 1 kHz in [19].

with higher resolution temperature tuning so that the residual dispersion could be optimized [20].

The second reason for lower SHG efficiency might be related to the overall energy available to the seed distribution system. The limited energy the Ti:sapphire oscillator provides at 1030 nm is causing poor signal-to-noise ratio in the first fiber amplifier. The amplified spontaneous emission contribution from this amplifier and possibly other amplifiers within the seed distribution system leads to a degraded contrast of the compressed pulses and, hence, to a lower SHG efficiency.

We have shown the results of 1 kHz, 515 nm picosecond pump laser, within the Allegra laser system at ELI Beamlines, reaching more than 120 mJ. Although with non-ideal compression and contrast, we still achieved SHG efficiency of 60%. By mitigating laser-induced contamination and by proper thermal management of the vacuum SHG mount with TEC elements and copper heat-straps, we showed that stable frequency doubling and full-day operation of a high power pump laser in vacuum can be realized without the need for phase matching corrections. With an average power RMS stability of 1.1% for more than 8 h, the system presented here proves to be a robust, stable pump laser providing pulses with sufficient energy for the final OPCPA stages of the Allegra system. Future upgrade aiming for reaching better SHG efficiency will involve an improved temperature tunable stretcher.

Funding. European Regional Development Fund (ADONIS, CZ.02.1.01/0.0/0.0/16–019/0000789); Ministry of Education, Youth and Sports of the Czech Republic (Project No. LM2018141).

Disclosures. The authors declare no conflicts of interest.

Data Availability. Data underlying the results presented in this paper are not publicly available at this time but may be obtained from the authors upon reasonable request.

REFERENCES

1. C. L. Haefner, A. Bayramian, S. Betts, *et al.*, Proc. SPIE **10241**, 1024102 (2017).
2. F. Batysta, R. Antipenkov, T. Borger, A. Kissinger, J. T. Green, R. Kananavičius, G. Chériaux, D. Hidinger, J. Kolenda, E. Gaul, B. Rus, and T. Ditmire, Opt. Lett. **43**, 3866 (2018).
3. R. Antipenkov, F. Batysta, R. Boge, *et al.*, Proc. SPIE **11034**, 110340M (2019).
4. J. Nejdl, D.-D. Mai, U. Chaulagain, *et al.*, Proc. SPIE **11111**, 111110I (2019).
5. O. Hort, M. Albrecht, V. E. Nefedova, O. Finke, D. D. Mai, S. Reyné, F. Giambruno, F. Frassetto, L. Poletto, J. Andreasson, J. Gautier, S. Sebban, and J. Nejdl, Opt. Express **27**, 8871 (2019).
6. I. Ross, P. Matousek, M. Towrie, A. Langley, and J. Collier, Opt. Commun. **144**, 125 (1997).
7. A. Kessel, V. E. Leshchenko, O. Jahn, M. Krüger, A. Münzer, A. Schwarz, V. Pervak, M. Trubetskov, S. A. Trushin, F. Krausz, Z. Major, and S. Karsch, Optica **5**, 434 (2018).
8. R. Budriūnas, T. Stanislauskas, J. Adamonis, A. Aleknavičius, G. Veitas, D. Gadonas, S. Balickas, A. Michailovas, and A. Varanavičius, Opt. Express **25**, 5797 (2017).
9. J. Novák, J. T. Green, T. Metzger, T. Mazanec, B. Himmel, M. Horáček, Z. Hubka, R. Boge, R. Antipenkov, F. Batysta, J. A. Naylon, P. Bakule, and B. Rus, Opt. Express **24**, 5728 (2016).
10. S. Klingebiel, M. Schultze, C. Y. Teisset, R. Bessing, M. Häfner, S. Prinz, M. Gorjan, D. Sutter, K. Michel, H. G. Barros, Z. Major, F. Krausz, and T. Metzger, in *CLEO—European Conference on Lasers and Electro-Optics* (2015), paper STu4O.2.
11. B. Gronloh, P. Russbueldt, B. Jungbluth, and H.-D. Hoffmann, Proc. SPIE **8959**, 89590T (2014).
12. F. Zhuang, B. Jungbluth, B. Gronloh, H.-D. Hoffmann, and G. Zhang, Appl. Opt. **52**, 5171 (2013).
13. J. P. Phillips, S. Banerjee, K. Ertel, P. Mason, J. Smith, T. Butcher, M. D. Vido, C. Edwards, C. Hernandez-Gomez, and J. Collier, Opt. Lett. **45**, 2946 (2020).
14. M. Horáček, L. Indra, J. T. Green, J. A. Naylon, B. Tykalewicz, J. Novák, F. Batysta, T. Mazanec, J. Horáček, R. Antipenkov, Z. Hubka, R. Boge, P. Bakule, and B. Rus, Rev. Sci. Instrum. **88**, 013109 (2017).
15. Z. Hubka, J. Novák, I. Majerová, J. T. Green, P. K. Velpula, R. Boge, R. Antipenkov, V. Šobr, D. Kramer, K. Majer, J. A. Naylon, P. Bakule, and B. Rus, Appl. Opt. **60**, 533 (2021).
16. A. V. Smith, "SNLO classic," https://as-photonics.com/products/snlo/.
17. S. Prinz, M. Schnitzenbaumer, D. Potamianos, M. Schultze, S. Stark, M. Häfner, C. Y. Teisset, C. Wandt, K. Michel, R. Kienberger, B. Bernhardt, and T. Metzger, Opt. Express **26**, 1108 (2018).
18. A. Špaček, J. T. Green, F. Batysta, J. Novák, R. Antipenkov, P. Bakule, and B. Rus, J. Opt. Soc. Am. B **35**, 2494 (2018).
19. H. Chi, Y. Wang, A. Davenport, C. S. Menoni, and J. J. Rocca, Opt. Lett. **45**, 6803 (2020).
20. J. Želudevičius, R. Danilevičius, and K. Regelskis, J. Opt. Soc. Am. B **32**, 812 (2015).